

DESIGN, ANALYSIS, AND FLIGHT TEST OF A COMPACT, HEAVY-LIFT VTOL DELIVERY DRONE

NOAH MCGUINNESS, NOAH SCHOCHET AND NATHAN SPILKER, '21

SUBMITTED TO THE
DEPARTMENT OF MECHANICAL AND AEROSPACE ENGINEERING
PRINCETON UNIVERSITY
IN PARTIAL FULFILLMENT OF THE REQUIREMENTS OF
UNDERGRADUATE INDEPENDENT WORK.

FINAL REPORT

MAY 28, 2021

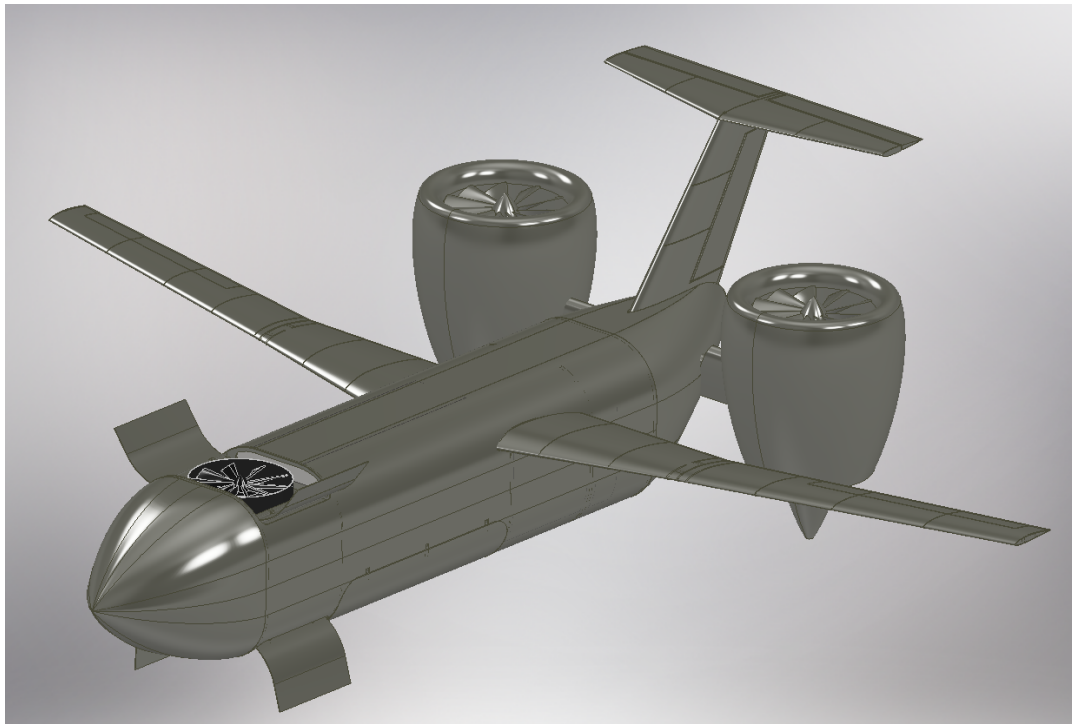
PROFESSOR DANIEL
NOSENCHUCK
PROFESSOR LUIGI MAR-
TINELLI
MAE 444
125 PAGES
ADVISER COPY

© Copyright by Noah McGuinness, Noah Schochet and Nathan Spilker, 2021.
All Rights Reserved

This thesis represents my own work in accordance with University regulations.

Abstract

This thesis explores the theoretical design and analysis of a serial hybrid-electric, fully-autonomous, package delivery system for midrange (250-500 mi) missions and payloads up to 25 pounds. To improve applicability without existing infrastructure, the vehicle is designed to be as compact as possible, with full vertical-takeoff and landing (VTOL) capabilities in a hybrid fixed-wing/tri-copter configuration. The project covers the full breadth of the design process, including initial aircraft sizing methods; propulsion, powertrain and electrical design; structural design for practical manufacture and integration; analysis of the airframe; aerodynamic analysis for stability and control; and the development of closed loop MIMO controllers for VTOL and transition flight to demonstrate controllability. Further, to explore the viability of the tri-copter configuration and prove out the VTOL control scheme, a physical scale model is constructed and flight tested.



Acknowledgements

We would first and foremost like to thank our advisor, Professor Daniel Nosenchuck, for his continued advice and support throughout the year: not only for advising us on the scope of our project, but for inspiring us to continue this project after graduation in the pursuit of innovation.

Additionally, the development of the scale prototype of the design presented in this thesis would not have been possible without the generous assistance from the Morgan W. McKinzie '93 Senior Thesis Prize Fund, for which we are grateful.

Last, but not least, we would like to thank the MAE Department for working around the clock to make our Senior year and thesis projects as educational and fulfilling as possible given the difficult circumstances of COVID-19.

Contents

Abstract	iii
Acknowledgements	iv
List of Tables	viii
List of Figures	ix
List of Symbols	xiv
1 Introduction	1
1.1 Project Motivation	1
1.2 Thesis Outline	2
2 Overview	4
2.1 Benefits of UAV Delivery and Logistics	4
2.2 Technology Review	7
2.2.1 Multi-rotor	7
2.2.2 Fixed Wing	7
2.2.3 Hybrid	8
2.3 Proposed Mission	9
2.4 Final Vehicle Overview and Specifications	10
3 Sizing Design Process	13
3.1 Configuration Investigation	13
3.2 Preliminary Sizing	15
3.3 Configuration Design	20
3.3.1 Fuselage Sizing	20
3.3.2 VTOL Stability Considerations	20
3.3.3 Modelling Propulsion	22
3.3.4 Wing, Tail, and EDF Placement	22
3.3.5 Aerodynamic Performance	25
3.3.6 Power Requirements	29

3.3.7	Updated Fuel Fractions and Range	30
3.3.8	Control Surface Sizing	30
4	Detailed Design	32
4.1	Powertrain	32
4.1.1	Propulsion	32
4.1.2	Hybrid Electric	32
4.1.3	Batteries	34
4.2	Structures and Airframe	36
4.2.1	Internal Frame	36
4.2.2	Fuselage Skin	43
4.2.3	Wings and Tail	47
4.2.4	Fuel & Batteries	49
4.3	Guidance, Navigation, and Control	52
4.3.1	VTOL	52
4.3.2	Aerodynamic Coefficients and Simulation	58
5	Analysis and Simulation	62
5.1	Structures and Airframe	62
5.1.1	Fuselage Skeleton	62
5.1.2	Wings	64
5.1.3	Weights & Balance	67
5.2	Guidance, Navigation, and Control	67
5.2.1	VTOL Ascent	67
5.2.2	VTOL Descent	73
5.3	Updated Mass Budget	76
5.4	Updated Range	76
6	Small-Scale Prototype	77
6.1	Overview	77
6.1.1	Constraints	78
6.2	Scaling Considerations	78
6.3	Hephaestus: Small Scale Prototype Version 1: [Powertrain testing rig]	79
6.3.1	ESC Calibration and Motor Testing:	81
6.4	Chiron: Small Scale Prototype Version 2 [Core Systems and Hover Test]	82
6.4.1	Goal	82
6.4.2	Design considerations	83

6.4.3	Testing and Results	86
6.5	Hermes: Small Scale Prototype Version 3	88
6.5.1	Goal	88
6.5.2	Results	88
6.5.3	Addressing Issues of Prior Iteration	89
6.5.4	Tilt Rotor Mounting Mechanism	89
6.5.5	Generative Design	92
6.5.6	Topology Optimization	95
6.5.7	Future Considerations	96
7	Conclusions and Future Directions	97
A	Sizing Calculations	100
A.1	Carpet Plot Generation	100
A.2	Actuator Disk Parameters	101
A.3	Tail Sizing	101
A.4	Neutral Point Calculations	102
A.5	Flight Mode Power and Range Calculations	103
A.6	Control Surface Sizing	105
B	Final Configuration Analysis	107
B.1	Final Range	107
C	GNC	108
C.1	VTOL Ascent	108

List of Tables

3.1	Mission Requirements	13
3.2	Preliminary Mass Budget	18
3.3	Preliminary Fuel Fractions	19
3.4	Fuel and Power Budget	30
3.5	Control surface parameters	31
4.1	Linear Plant Parameters	56
4.2	Maximum Acceptable Values of State and Control Variables, Ascent .	57
5.1	Parameters for Nonlinear System	71
5.2	Maximum Acceptable Values of State and Control Variables, Descent	73
5.3	Final Mass Budget	76

List of Figures

2.1	Mission Profile	10
2.2	Side View of Aircraft	11
2.3	Front View of Final Vehicle.	11
2.4	Top View of Final Vehicle.	12
3.1	Payload Range for Representative Aircraft with Pure Battery Power .	14
3.2	Carpet Plot	16
3.3	Schubeler DS-215-DIA HST EDF	17
3.4	Pegasus Aeronautics GE70 Gas Generator	18
3.5	OpenVSP Rending of Fuselage	20
3.6	EDF Layout	21
3.7	Kinked Wing Configuration	23
3.8	Full Configuration Front View, AR = 13.4	24
3.9	Full Configuration Top View, AR = 13.4	24
3.10	Trailing Wakes on Full Configuration, AR = 13.4	25
3.11	L/D vs. α for Full Configuration, AR = 13.4	26
3.12	L/D vs. α for Full Configuration, AR = 17.3	27
3.13	Full Configuration Top View, AR = 17.3	27
3.14	Trailing Wakes on Full Configuration, AR = 17.3	28
3.15	L/D vs. α for Full Configuration, 6° Wing Incidence	28
3.16	Front View of Final Configuration	29
4.1	A comparison of serial and hybrid electric systems	34
4.2	Early Internal Frame Iteration	37
4.3	Fuselage Frame and Skin	37
4.4	Fuselage Frame and Skin - Cutaway View	38
4.5	Final Fuselage Internal Frame (no mesh)	38
4.6	Front EDF Mount	39
4.7	Main Wing Mount	40

4.8	Installed Wing Mount	41
4.9	Wing Fasteners with Internal Mandrill	41
4.10	Fully Integrated Pegasus GE70	42
4.11	Pegasus G70 Mount (view 2)	43
4.12	Final Fuselage Internal Frame (meshed)	43
4.13	Labeled Skin (Assembled Panels)	44
4.14	Cutaway view of payload skin with frame (doors open)	45
4.15	Bottom view of payload and EDF doors	46
4.16	Representative view of skin assembly and half doors open	47
4.17	T-Tail Installation and Structure	48
4.18	Two-Part Wing	49
4.19	Integrated Fuel Tank.	50
4.20	Battery Storage	51
4.21	Fuel Tank	51
4.22	Simulink 6DOF Simulation for Cruise	60
4.23	Sample VSP Run for Populating Aero Database	60
4.24	3 DOF Aerodynamic Database	61
5.1	Final Frame Static Stress Analysis	63
5.2	Final Frame Buckling Analysis	63
5.3	Figure : Linear Buckling Analysis (Mode 1; eig = 29.5)	64
5.4	Wing-Mount Static Analysis (140 lbs)	64
5.5	Wing-Mount Buckling: Mode 1 Eigenvalue	65
5.6	Full Wing Assembled	65
5.7	Frame-Only Wing Buckling	66
5.8	Wing Buckling with Skin	66
5.9	Final CG	67
5.10	Linear System Simulink Representation	68
5.11	Linear Response VTOL Ascent 1	69
5.12	Linear Response VTOL Ascent 2	70
5.13	Position and Velocity Response to -0.5 ft/s Ramp Input	72
5.14	Descent Guidance Algorithm	74
5.15	Position and Velocity Response to Descent Guidance	75
6.1	Version 3 prototype	77
6.2	Version 1 prototype	80
6.3	Version 2 prototype	82

6.4	Front Tilt Mechanism	85
6.5	Stable hover test	87
6.6	Version 3 prototype	88
6.7	Gear box for tilting rear EDFs	92
6.8	3D printed, generatively designed motor mount	93
6.9	Generatively designed motor mount	94
6.10	Generatively designed motor mount	94
6.11	A mesh showing the wing box after topology optimization	95
6.12	Sections of the fuselage, 3D printed with tree supports	96
A.1	Sizing Script for Carpet Plot	100
A.2	Mathematica Script to Determine Actuator Disk Parameters	101
A.3	Mathematica Script for Sizing Tail	101
A.4	$\frac{\partial C_{M_{ref}}}{\partial C_L}$ for Full Configuration, AR = 13.4	102
A.5	$\frac{\partial C_{M_{ref}}}{\partial C_L}$ for Full Configuration, AR = 17.3	102
A.6	Climb 1 Flight Mode Analysis	103
A.7	Cruise 1 Flight Mode Analysis	103
A.8	Climb 2 Flight Mode Analysis	104
A.9	Cruise 2 Flight Mode Analysis	104
A.10	Script For Control Surface Sizing	105
A.11	Script Output For Control Surface Sizing	106
B.1	Mathematica Script For Final Range Calculation	107
C.1	Full Nonlinear Simulink Model	108
C.2	Linear Controller in Nonlinear Model	109
C.3	Euler Angle and Body Rate Response to -0.5 ft/s ramp input	110
C.4	Euler Angle and Body Rate Response to Descent Guidance	111

List of Symbols

C_d	drag coefficient	15
C_{d_0}	zero-lift drag coefficient	15
C_{d_i}	induced drag coefficient	15
C_l	lift coefficient	15
AR	aspect ratio	15
e	Oswald efficiency factor	15
W	weight	15
S	wing area	15
\bar{Q}	dynamic pressure	15
W_{TO}	takeoff weight	15
$\frac{dh}{dt}$	climb rate	16
TWR	thrust to weight ratio	16
SFC	specific fuel consumption	18
$\frac{L}{D}$	lift-to-drag ratio	18
R	range	18
g	acceleration of gravity	18
η_o	overall efficiency of EDF	19
P	power	19
T	thrust	19
β	fuel fraction	19
C_t	coefficient of thrust	22
C_p	coefficient of power	22
SM	static margin	22
\bar{c}	length mean aerodynamic chord	22
x_{cg}	x-coordinate of center of gravity	22
x_n	x-coordinate of neutral point	22
l_{x_i}	x-distance from ith EDF to center of gravity	23
l_{y_i}	y-distance from ith EDF to center of gravity	23

x_{ref}	moment reference center	25
α	angle of attack	25
α_{trim}	trim angle of attack	28
γ	flight path angle	29
SEP	specific excess power	29
I_{jk}	jk component of inertia tensor	52
$s()$	sine	52
$c()$	cosine	52
$t()$	tangent	52
p	body roll rate	52
q	body pitch rate	52
r	body yaw rate	52
\dot{p}	body roll acceleration	52
\dot{q}	body pitch acceleration	52
\dot{r}	body yaw acceleration	52
x_I	x-coordinate in inertial frame	52
y_I	y-coordinate in inertial frame	52
z_I	z-coordinate in inertial frame	52
u	body x-velocity	52
v	body y-velocity	52
w	body z-velocity	52
ϕ	roll angle	52
θ	pitch angle	52
ψ	yaw angle	52
L	rolling moment	52
M	pitching moment	52
N	yawing moment	52
X_B	body x-force	52
Y_B	body y-force	52
Z_B	body z-force	52
ϵ	thrust vane deflection angle	53
A_{proj}	projected area onto XY plane	53
ω_i	angular rate of ith propeller	53
b	propeller reaction torque coefficient	53
T_i	thrust of ith EDF	53
H_B^I	transformation from body to inertial coordinates	54

X_I	x-force in inertial coordinate system	54
Y_I	y-force in inertial coordinate system	54
Z_I	z-force in inertial coordinate system	54
m	mass of aircraft	55
r	reference signal vector	56
K	feedback gain matrix	56

Chapter 1

Introduction

1.1 Project Motivation

The growth of e-commerce and the logistics industry in the 21st century has produced a significant demand for rapid doorstep delivery. With “last-mile delivery” being the most expensive per-unit leg of any logistics operation, we believe that within the next decade there will be an incentive for companies with large distribution networks to adopt autonomous delivery solutions for the reduction of cost and fulfillment times, pressuring the FAA to normalize UAV operations. As restrictions are reduced on the usage of unmanned vehicles for the autonomous delivery of packages via air, there is anticipated to soon be a large demand for vehicles capable of performing this feature efficiently and without human supervision. Amazon and other tech startups operating in this space have primarily focused their efforts on the development of electric multi-rotor or hybrid aerial drones that are capable of delivering packages from the 1oz-4lb weight range; however, due to the limitations of current battery technology, the range and payload capabilities of these solutions are highly limited.

It is well known that transporting heavy payloads over long distances is a problem most efficiently solved by fixed-wing aircraft that rely on aerodynamic forces to generate lift, requiring only a steady forward thrust to maintain the required airspeed. This force is often only a small fraction of the net weight of the vehicle. In contrast, multi-rotor solutions must generate enough thrust such that the vertical component of the force vector in horizontal flight is of equal magnitude to the vehicle’s weight, and that the horizontal component is sufficient to achieve translational motion at a reasonable speed. The configuration presents significant complications for energy

consumption, as all onboard motors must work full-time to maintain flight; however, the primary benefit of employing multirotor systems lies in the ability to takeoff and land vertically, without the need for any existing infrastructure such as long runways. For this reason, VTOL has been the primary focus of autonomous aerial delivery systems currently in development.

In order to tackle the range of payloads above 4 lbs, the required size and footprint of current VTOL systems capable of extended-range missions drastically increases, making it impractical for many consumer and commercial applications where landing in a small space or densely-populated area is required. For this reason, this thesis seeks to develop an autonomous vehicle capable of carrying packages up to 25 lbs up to a total range of up to 600 miles while maintaining physical dimensions capable of fitting well within a standard compact parking space (8' x 16'). In order to accomplish this, a unique vehicle configuration was adopted, employing high-thrust electric ducted fans (EDFs) in a tri-copter configuration for VTOL, and a fixed-wing design capable of cruising at speeds up to Mach 0.3 (approximately 225 mph). The drone utilizes electric motors, with batteries for full-electric takeoff and landing operations and an internal combustion engine (ICE) coupled to a 4500 kW generator for powering the two rear motors for cruising flight.

1.2 Thesis Outline

The objective of this thesis is twofold: to explain the engineering design methodology used to develop a novel aerospace vehicle and to demonstrate the viability of this system at a small scale by constructing and flight-testing a physical prototype. From the early stages of identifying a practical problem and brainstorming potential solutions, to developing a detailed design of the final vehicle configuration, this thesis will provide the reader with an overview of the unmanned aerial vehicle's (UAVs) intended mission, overall performance and specifications, and explanation of each subsystem and its function. Because the vehicle developed in this paper is unconventional and does not have a strong precedent, significant portions of this work will be dedicated to demonstrating the practicality, stability, and controllability of our design and its viability for real-world applications. To further justify the calculations and methods used to develop detailed designs of each subsystem and analyze the overall vehicle, more lengthy technical data and figures will be elaborated on in the appendices for a clearer description of the exact processes used.

This thesis will begin by conducting a brief literature review of the existing mar-

ket for drone deliveries, demonstrating that there is a substantial gap both in the market for our product’s application and in the existing technology proving the viability of our UAV’s unique configuration. Next, the considerations used to narrow down vehicle configurations to the final tri-rotor VTOL / fixed-wing twin-rotor layout will be discussed, with an overview of the sizing process used to narrow down possible missions and develop rough vehicle dimensions to meet range and payload requirements.

In the following chapter, a detailed overview of each subsystem will be presented. First, all aspects of the physical design will be explained in three major sections: propulsion and powertrain, structures and airframe, and mechanisms and actuators. Methods of assembly and manufacture of each component will also be discussed at a high level. Next, guidance, navigation and control (GNC) will be discussed to demonstrate that the control systems developed and onboard control inputs (differential thrust and thrust-vaning for VTOL; thrust, elevators, ailerons, and rudder for cruise) are capable of autonomously guiding the vehicle through its mission in the context of a high-fidelity dynamic mathematical model implemented in MATLAB & Simulink.

The next chapter will be dedicated to the detailed analysis of the final vehicle, proving the ability of the craft to perform the mission requirements. The analysis will demonstrate the structural integrity, airworthiness, capacity, range, and controllability of the UAV in detail. The methods used were primarily computational and finite-element based; however, empirical results from sub-scale testing also guided the analysis and development process for the full-sized design.

In addition to demonstrating the successful physical flight-test of a scaled proof-of-concept, the theoretical portion of this paper lays the groundwork for the development of the full-scale system by explaining the exact manufacturing methodologies and existing components that could be used to construct a functioning version for reasonable up-front costs. The final sections will describe the manufacturing procedures and cost-analysis for developing initial prototypes of the design, before concluding with considerations for redesign for more practical mass-manufacturing.

Chapter 2

Overview

2.1 Benefits of UAV Delivery and Logistics

Modern transportation and logistics infrastructure is an incredibly complex system. Getting people and things from point A to point B is no small task, and relies on utilizing many different modes of transportation, types of infrastructure, and methods of distribution while seeking to optimize a cost function that includes numerous variables such as per unit cost, per mile cost, speed, safety, and more. Recent technological advancements in UAVs have made them a promising tool that can drastically improve the efficiency of logistic and distribution systems.

'Logistical UAV' is a somewhat intentionally ambiguous term used in this section to refer to the broad class of unmanned aerial vehicles, either autonomous or remotely piloted, used to move people or things from point A to point B. Distribution networks are incredibly complex systems, but logistical UAVs can and will become a widespread, essential tool. This broad category encompasses a wide variety of vehicles that are designed for specific use cases and contexts. For simplicity, this section will discuss logistical UAVs in an general, often idealized sense, but it should be noted that these trends do not necessarily hold true for every specific configuration, implementation, or use case. Among the plethora of benefits logistical UAVS may have over alternative modes of transportation are higher speed, lower cost, decreased carbon footprint, decreased reliance on physical infrastructure, and distribution chain simplification.

Speed

logistical UAVs have the potential to be among the fastest modes of transportation available. They can be deployed rapidly and fly directly to the recipient with no stops in between. They also benefit from traveling at higher speeds than ground vehicles, avoiding delays and bottlenecks such as traffic, and can take a more direct "as the crow flies" route between points.

Cost Savings

- Despite the increased prevalence of "free shipping," transportation costs are increasing. 2021 saw shipping costs soar to record highs as the COVID-19 pandemic exacerbated. The research on potential cost savings due to logistical UAVs is conflicting, and illustrates that cost reduction is largely context dependent. One potential area for cost reduction is eliminating or minimizing the reliance on labor. From a technological perspective UAVs will shortly be able to operate completely autonomously. Regulation and public opinion could lead to a norm where UAVs are controlled by a remote operator, who oversees several drones or perhaps directly pilots one at a time. Another transportation expense that UAVs have the potential to reduce is fuel costs. Fully or hybrid electric UAVs would eliminate fuel costs, and use cheaper forms of energy.

Decreased Carbon Footprint

- It is no secret that the transportation sector is a massive source of pollution and greenhouse gasses. The transportation sector is the largest carbon emitter, responsible for roughly 30% of all global carbon emissions, with 90% of these carbon emissions coming from diesel and gasoline [1]. The reduction in emissions for fully electric UAVs depends on the source of electricity used to power the batteries. Hypothetically, electric UAVs can reduce emissions by nearly 100% if charged using electricity exclusively from renewable sources. UAVs can not entirely eliminate emissions due to shipping as other segments of the logistics chain will likely continue to use fossil fuels for the near future.

Reduced Reliance on Physical Infrastructure

- While trucks require roads, trains require rails, and ships require ports, logistical UAVs require far less infrastructure. UAVs in their simplest form only require a flat

area to take off and land, a source of electricity to charge (or other fuel source), and GPS signal. Widespread adoption of drone delivery, however, would still result in some additional infrastructure. Most current logistic UAVs have a limited range, and would require distribution centers to be built in or near densely populated urban areas. UAVs would also require launch and landing site infrastructure. Depending on the vehicle and environment, this infrastructure requirement varies dramatically, and could be as little as a small paper with a specific simple printed on it, or as much as vast networks of 'vertiports' that allows numerous drones to takeoff and land simultaneously. Electric UAV's would also need charging infrastructure, which could range from charging pads connected to simple wall outlets; to large 'bee hives' featuring automated machines that charge and swap batteries; to a series of smaller charging waypoints mounted on rooftops or even telephone poles. Lastly, logistic UAVs would require unmanned traffic management (UTM) systems that would perform multiple functions such as helping drones avoid collisions, avoid hazardous areas to fly (such as over concerts, government buildings, powerplants), deal with hazardous weather, and even know the safest place to crash if a critical failure occurs. These UTM systems could feature radar, radio towers, beacons, and other communication systems. The UTM infrastructure requirements are much less for UAVs flying at higher altitudes or over rural regions. While the infrastructure requirements listed may appear daunting, real world implementations of them are likely to be considerably easier than alternative types of infrastructure due to the inherent flexibility of the required infrastructure, and room for novel implementations. For starters, much of the infrastructure requirements can be simplified, combined, or retrofitted to existing infrastructure. Distribution centers will likely be housed in the countless warehouses e-commerce giants are already building regardless of UAV adoption. Charging stations can be combined with package lockers, housed on unused rooftops, combined with EV charging stations, or even mounted on lightposts. The key takeaway is that compared to physical infrastructure for other transportation methods, UAV infrastructure is cheaper, smaller footprint, and easier to create.

Distribution Chain Simplification

- In order for a seemingly simple task to be done, for example business A sends a box to Business B, an incredibly complex series of tasks needs to be rapidly executed without errors. The package is picked dropped off at a shipping storefront or post office, a truck picks it up and takes it to a regional hub, its sorted, loaded onto

a truck or plane, transported hundreds of miles to a different regional hub, sorted again, driven by truck to a smaller distribution facility, sorted again, loaded onto yet another truck, driven around while the driver makes almost 200 stops, and then finally it arrives at its destination. This process is slow, expensive, and highly susceptible to disruption. In contrast, with logistic UAVs, the process can be as simple as load box UAV, vehicle flies to destination and delivers box. This simplification makes it easier for a company to build a new distribution network, potentially eliminates the need for external logistics companies altogether, and makes it possible to ship fragile or perishable items.

2.2 Technology Review

Most UAV configurations fall into three main categories: multi-rotor, fixed wing, hybrid.

2.2.1 Multi-rotor

One of the most common form factor that UAVs adopt is the multi-rotor design, where a number of motors are attached to a frame, and the motors spin propellers which generate lift. When people hear the word "drone" this is what they tend to think of. This design is cheap to produce, is relatively simple with only the motors needing to move, lightweight, and maneuverable. They can also take off and land vertically with little to no infrastructure needed. Designs with 4, 6, or 8 motors are most common, but designs exist for any number of motors from 1 to upwards of 18. Multirotors are most powered by electric batteries, with Lithium Polymer and Lithium Ion being the dominant battery chemistries. Multi-rotors are not particularly energy efficient as their motors must constantly output thrust equal to the vehicle's weight just to stay airborne. These inefficiencies, combined with limitations in current battery technology mean multi-rotors have a short range (0-15 miles) and can not carry much payload (0-5lbs with exceptions carrying up to 16lbs). Examples include most DJI drones, and hobbyist quadcopters.

2.2.2 Fixed Wing

In contrast to multi-rotors, fixed wing aircraft use wings to generate lift which keeps the vehicle airborne. One or more motor is used to propel the craft forward. A useful

metric for comparing aerial vehicles is it's thrust-to-weight-ratio (TWR), which is a measure of how much thrust is output by its motors divided by the total vehicle weight. While multirotors need a TWR of 1 or higher, fixed wing aircraft have a TWR of around 0.1, meaning they only expend 1/10th as much energy. For this reason fixed wings are able to carry larger payloads over much longer distances compared to multirotors. The disadvantages of fixed wing aircraft are that they require infrastructure to take off and land, such as a runway, and that they tend to be much larger than their multirotor counterparts due to their wingspan. Some fixed wing aircraft operating as logistics UAVs mitigate the need for runways with a variety of methods such as launching with slingshots, and catching aircraft with nets, but that is still trading one type of infrastructure for another. Fixed wing aircraft vary dramatically in terms of size, cargo capacity, and range.

2.2.3 Hybrid

The last category of UAV's are VTOL aircraft, which combine the vertical takeoff and landing capabilities of multi-rotors with the long range and large payload capabilities of fixed wings. This type of design will become increasingly important and increasingly prevalent in the coming years as logistic UAVs begin to expand their reach in terms of payload and range. These hybrid vehicles can be classified into 3 groups based on how they achieve VTOL. VTOL aircraft are not a new concept, but have historically proven to be extremely difficult to implement in combustion engine vehicles. This is because the power requirements of the propulsion system for take off and for cruise are very far apart (1:10 ratio), and combustion engines can not be highly efficient over such a huge gap. Electric motors, however, operate efficiently across a large band of power outputs, making long coveted VTOL designs increasingly feasible and practical. The three general types of VTOL craft are:

1. Lift = Cruise ($L=C$). In this configuration a single system is used for propulsion in cruise and in hover. The most notable example of this is the Boeing V-22 Osprey. In the UAV world, the common implementation of $L=C$ is a "tailsitter" which takes off with its nose pointed up and its tail on the ground, and then rotates its entire body 90 degrees to fix wing after takeoff. This design reduces mechanical complexity, but is hard to stabilize and results in an engine that is poorly matched for cruise.
2. Lift + Cruise ($L+C$) . In this configuration two completely separate systems are used for hover and cruise. A common implementation of this is the "quadplane"

design which is simply attaching a multi rotor to a fixed wing plane. This design is currently one of the most widely used in logistic UAVS because it is simple to implement and reliable. The transition from hover to cruise, a major source of difficulty in creating a robust VTOL design, is mostly avoided by having two separate systems. This design is not particularly efficient however as the system for hover must be carried during lift, and adds a large amount of unnecessary weight and drag. As the electric VTOL market matures, it is likely these designs will decrease in popularity.

3. Lift + Lift/Cruise (L+L/C). This design features a cruise propulsion system that generates significant lift for hover, but a smaller lift system is used to supplement it in hover. This design combines many of the desirable qualities of the previous two while avoiding some of the drawbacks. Essentially, using a smaller lift system to augment hover means the range of thrusts the cruise motors must operate over is decreased, and using the cruise motors for lift means the minimum amount of extra mass is carried around during cruise. One large scale example of this is the F-35B Lightning 2 which uses a lift fan to provide S/VTOL capabilities. This design is very efficient, but is mechanically complex and requires more actuators.

2.3 Proposed Mission

The proposed mission is outlined in Figure 2.1. The package will be loaded, takeoff vertically, travel to the destination up to 250 miles away, and land vertically. Once the package is removed it will follow the same procedure to travel home.

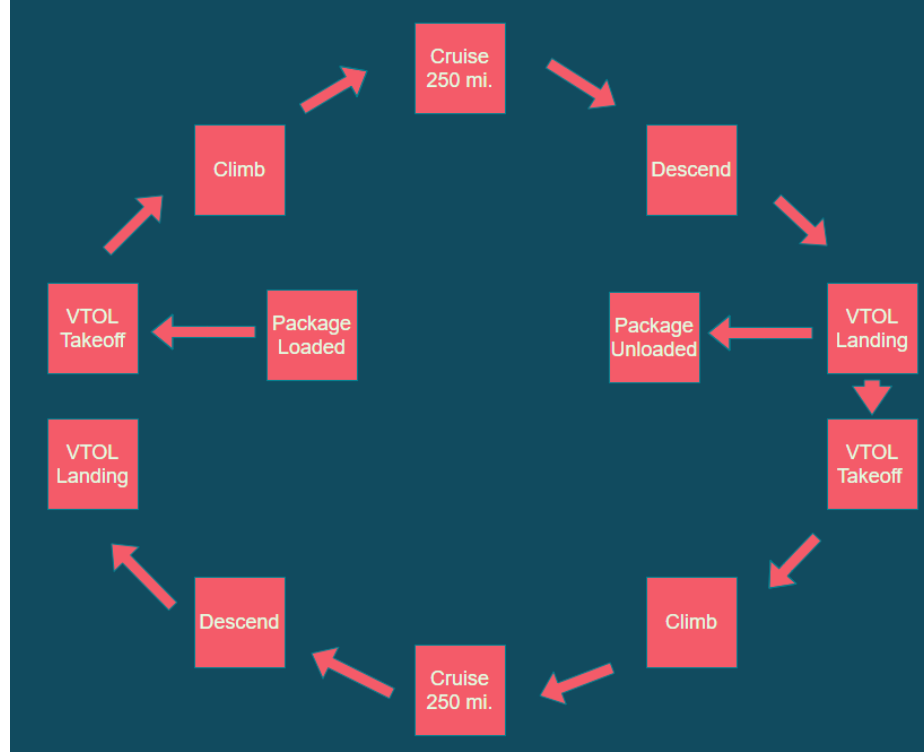


Figure 2.1: Mission profile.

2.4 Final Vehicle Overview and Specifications

The final vehicle has a takeoff weight of 120 lbs. It can carry a 25 pound payload and has a maximum two-way range of 650 miles. It has VTOL capability, as well as a folding wing mechanism for landing. It is a tricopter configuration: two tilting rear electric ducted fans provide cruising thrust while tilted forward, and VTOL thrust is provided by the two rear electric ducted fans tilted upward and a third electric ducted fan stowed within the fuselage permanently fixed upward. Yaw control during VTOL is accomplished via a thrust vane. The power plant is a small UAV gas generator which allows the range to be greatly extended beyond pure battery power. The configuration is compact; the wing span is 6.83 ft. A 3 view of the final configuration is shown in Figures 2.2, 2.3 and 2.4.

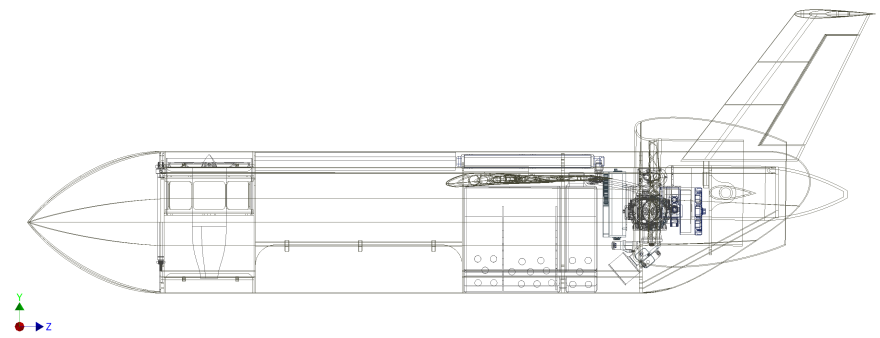


Figure 2.2: Side view of final vehicle.

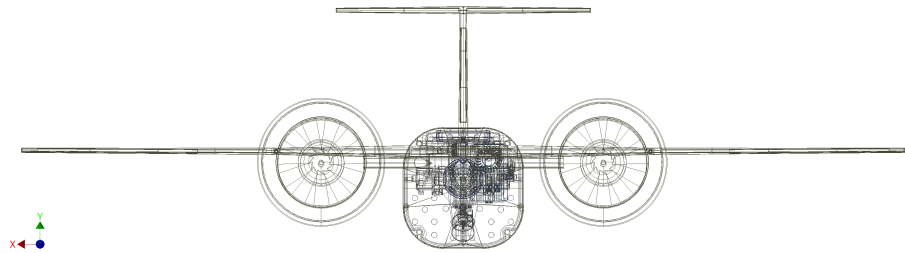


Figure 2.3: Front view of Final Vehicle.

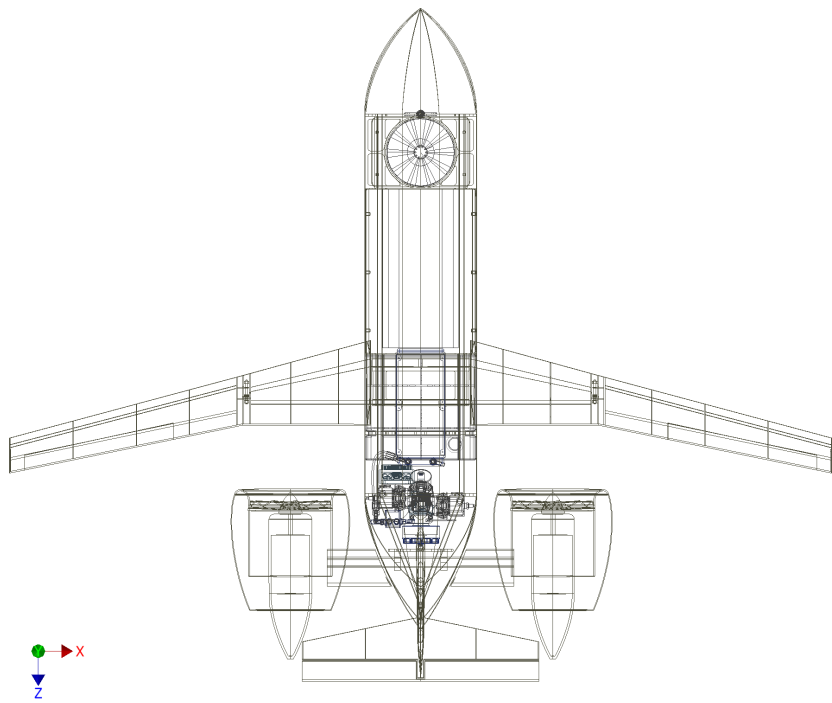


Figure 2.4: Top view of Final Vehicle.

Chapter 3

Sizing Design Process

Table 3.1: Mission Requirements

Payload Weight	25 lbs.
Payload Dimensions	15”x10”x10”
Max span	7 ft.
Range	500 mi.
Cruising Altitude	1000 ft.
Cruising Speed	Mach 0.21
Climb Gradient	3.8%
Takeoff Method	VTOL

3.1 Configuration Investigation

A driving requirement in the mission of the aircraft under development is the compactness of the solution, while also retaining VTOL capabilities. With a payload requirement of 25 lbs. and assuming an optimistic payload fraction of 0.3, to have a thrust-to-weight ratio of 1.2 during VTOL, the thrust requirement is 100 lbs. Using 4 open propellers in a quadcopter configuration, the propellers may be sized to over 30” diameter. This is not the compact solution that this thesis hopes to achieve; such large propellers sweep over a very large area and have added safety concerns. A solution that is much more desirable utilizes EDFs, or Electric Ducted Fans. An electric ducted fan consists of an electrically driven propeller mounted inside a cylindrical duct. Ducted fans are much more efficient at producing thrust than open propellers at the same diameter, but are less efficient than propellers at low thrust, or dur-

ing cruise. EDFs provide a very compact propulsion solution, one that is extremely desirable for the proposed aircraft in this thesis.

In order to achieve the desired range of 500 miles, hydrocarbon fuel must be used. Due to the low energy density of batteries in 2021, a pure battery flight cannot meet our mission requirements. To illustrate this, a representative payload vs. range plot for an aircraft of similar weight class is shown in Figure 3.1, showcasing how little range the pure battery aircraft can achieve with an optimistic delivered battery energy density of 200 Wh/kg.

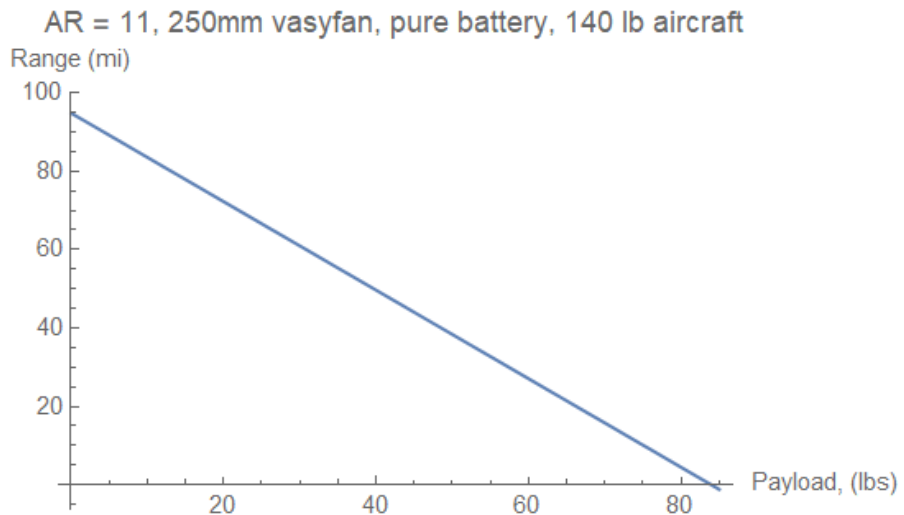


Figure 3.1: Payload vs. range diagram for representative aircraft with pure battery power.

Another consideration that was evaluated in the preliminary stages of this thesis is a quadcopter vs. tricopter configuration. A quadcopter configuration is immediately desirable due to the reaction torque balance on the aircraft. Since a quadcopter has an even number of propellers, it can have an equal number of propellers spinning clockwise and counterclockwise, thus balancing the reaction torques generated by the propellers. However, a tricopter has the advantage of the ability to stow its third rotor within the fuselage of the vehicle during cruising fixed wing flight, whereas the quadcopter leaves two motors and propellers in the flow, hurting the aerodynamic performance. It was decided to pursue the tricopter configuration in this thesis, with yaw control implemented with thrust vaning.

3.2 Preliminary Sizing

An important plot for propeller aircraft sizing is the Power-to-Weight vs. Wing Loading plot, also known as a carpet plot. The constraints on this plot for the proposed vehicle are the cruising constraint and climb rate constraint. There are no takeoff or landing runway length constraints because our proposed system will be VTOL. In order to develop the cruising constraint, a preliminary aspect ratio was chosen to be 13. Further developing the cruising constraint requires a definition of aerodynamic drag:

$$C_d = C_{d_0} + C_{d_i}$$

Where C_{d_0} is the parasitic drag coefficient and C_{d_i} is the induced drag coefficient. Define C_{d_i} :

$$C_{d_i} = \frac{C_l^2}{\pi A Re}$$

C_{d_0} is preliminary approximated as 0.02. e is the Oswald efficiency factor. The preliminary estimate made for this parameter is 0.6. The required lift coefficient for cruise is defined as:

$$C_{l_{req}} = \frac{W}{S \bar{Q}}$$

Where \bar{Q} is the dynamic pressure at cruise conditions and W is the instantaneous weight of the aircraft, which can be expressed as βW_{TO} , where W_{TO} is the takeoff weight and β is the product of weight fractions from all previous mission segments. Finally, based on the equilibrium condition where thrust is equivalent to drag, the cruise constraint can be derived:

$$\frac{T_{SL}}{W_{TO}} = \frac{\beta \bar{Q}}{\bar{\alpha}} \left(C_{d_0} + \frac{C_{l_{req}}^2}{\pi A Re} \right) \frac{S}{W_{TO}} \quad (3.2.1)$$

Or, in terms of power:

$$\frac{P}{W_{TO}} = V \frac{\beta \bar{Q}}{\bar{\alpha}} \left(C_{d_0} + \frac{C_{l_{req}}^2}{\pi A Re} \right) \frac{S}{W_{TO}} \quad (3.2.2)$$

Here, $\beta = \beta_{takeoff} \beta_{climb}$. $\beta_{takeoff} = 1$ because, as will be explained shortly, the takeoff will be powered by battery. β_{climb} is approximated as 0.99. $\bar{\alpha}$ is the ratio of cruise density to sea level density to adjust the thrust from sea level to cruise. The climb constraint can be derived by augmenting Equation 3.2.2 with the climbing

power requirement.

$$\frac{P}{W_{TO}} = V \frac{\beta}{\bar{\alpha}} \left\{ K_1 \frac{\beta}{Q} \frac{W_{TO}}{S} + \frac{C_{d0}}{\frac{\beta}{Q} \frac{W_{TO}}{S}} + \frac{1}{V} \frac{dh}{dt} \right\} \quad (3.2.3)$$

Here, $\beta = \beta_{takeoff} = 1$. K_1 is the induced drag coefficient over C_l^2 . $\frac{dh}{dt}$ is the climb rate. For a climb gradient of 3.8%, $\frac{dh}{dt} = 2.7 \text{ m/s}$. Plotting these constraints, the carpet plot is obtained. It is pictured in Figure 3.2.

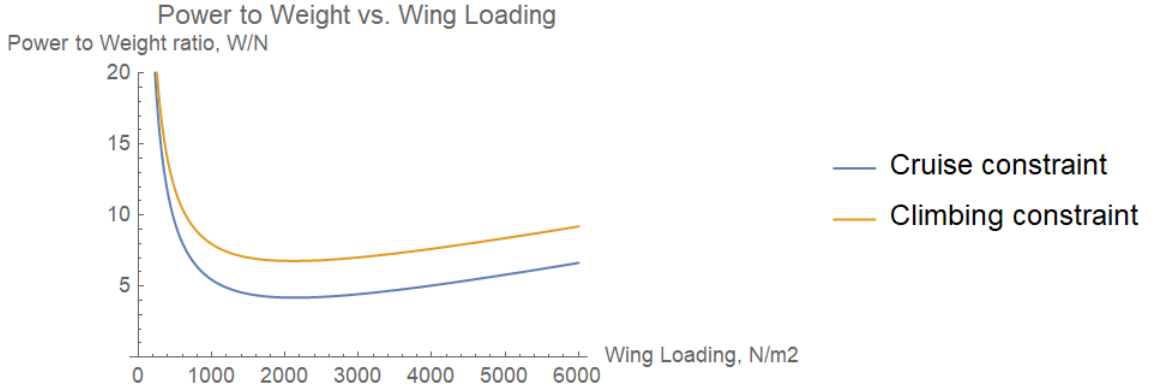


Figure 3.2: Carpet plot for the configuration under investigation.

The match point is found at the minimum of the climbing constraint curve: a wing loading of 2140 N/m^2 (44.7 lbs./ft^2) and a power to weight ratio of 4.2 W/N during cruise and 6.9 W/N during climb.

The total takeoff mass of the aircraft can be represented as follows:

$$W_{TO} = W_{payload} + W_{fuel} + W_{structure} + W_{generator} + W_{propulsion} + W_{battery}$$

In order to estimate some of these parameters, an initial estimate of W_{TO} was made:

$$W_{TO} \approx 120 \text{ lbs.}$$

This gives the aircraft a payload fraction of 0.21. This estimate allows the other parameters to be approximated. In order to achieve VTOL, the TWR of the entire aircraft must be larger than 1 during takeoff. A TWR of 1.2 was chosen as a preliminary estimate.



Figure 3.3: Schubeler DS-215-DIA HST EDF.[10]

In order to achieve a TWR of 1.2 for the entire aircraft, the aircraft will need 145 lbs. of VTOL propulsion. As stated before, EDFs were chosen as the best suited source of propulsion for this aircraft due to their high thrust in a smaller package compared to motor-driven open propellers. An initial EDF was chosen to meet the rear propulsion requirement: the Schubeler 195mm EDF. It provides 56 lbs. static thrust, weighs 9.7 lbs. with the recommended ESC, and pulls 15.6 kW at full throttle[10]. The front propulsion requirement was initially sized to be the Vasy Fan 160mm EDF. It provides 33.7 lbs. of static thrust, weighs 6 lbs. with the recommended ESC, and pulls 14kW at full throttle[8]. This gives the aircraft 145 lbs. static thrust.

The power draw of all motors at full throttle is 45.2kW. After researching small gas generators, it was determined that the power output of a small generator is too low to power VTOL. The VTOL mission segments would have to be battery powered. To give the aircraft 120 s of VTOL, the energy requirement is 1.42 kWh. Using lithium-ion batteries as an initial choice for the battery pack, and assuming a delivered energy density of 180 Wh/kg, the weight of batteries becomes 17.3 lbs.



Figure 3.4: Pegasus Aeronautics GE70 gas generator.[2]

A high performance UAV gas generator from Pegasus Aeronautics called the GE70 was chosen as an initial option for electricity generation. It provides a maximum of 4 kW and weighs 9.7 lbs [2]. Assuming a structure mass of 25lbs., we arrive to the mass budget shown in Table 3.2.

Table 3.2: Preliminary Mass Budget

Component	Mass (lbs.)
Payload	25
Structure	25
Generator	9.7
Propulsion	25.4
Battery	17.3
Fuel	17.6
Total	120

In the initial estimate of a takeoff weight of 120lbs., there are 17.6 lbs. remaining for fuel. In order to find the correct fuel fraction, the Breguet range equation will be used.

$$R = \frac{1}{g} \frac{V}{SFC} \frac{L}{D} \ln\left(\frac{1}{\beta_{cruise}}\right) \quad (3.2.4)$$

Where R is the range of the aircraft, SFC is the thrust specific fuel consumption, and $\frac{L}{D}$ is the lift-to-drag ratio of the aircraft. The theoretical maximum lift-to-drag ratio can be calculated using the formula:

$$\left(\frac{L}{D}\right)_{max} = \frac{1}{2} \sqrt{\frac{\pi e A R}{C_{d_0}}} \quad (3.2.5)$$

The delivered lift-to-drag ratio is assumed to be 75% the theoretical maximum. Thus, $\frac{L}{D} = 13.5$. Using the initial takeoff weight estimate of 120 lbs., the thrust requirement during cruise becomes 8.9 lbs. To determine power requirement in cruise, the following equation is used:

$$P_{req,generator} = P_{req}\eta_o \quad (3.2.6)$$

The propulsive power is defined in equation 3.2.7.

$$P_{req} = TV \quad (3.2.7)$$

As stated by the EDF manufacturer, η_o is 0.78[10]. Therefore, the power requirement during cruise evaluates to 3.6 kW. The SFC is calculated using equation 3.2.8.

$$SFC = \frac{\dot{m}_{fuel}}{T} \quad (3.2.8)$$

The Pegasus GE70's power specific fuel consumption is 0.61 kg/kW/hr. \dot{m}_{fuel} is calculated, based on the power requirement, to be 0.0006 kg/s. The SFC is calculated to 1.54e-5 kg/s/N. Now, solving Equation 3.2.4 for the range requirement of 500 miles, the cruising fuel fraction is determined:

$$\beta_{cruise} = 0.88$$

The total fuel fractions over the flight are displayed in Table 3.3.

Table 3.3: Preliminary Fuel Fractions

$\beta_{takeoff,1}$	1
$\beta_{climb,1}$	0.99
β_{cruise}	0.88
$\beta_{landing,1}$	1
$\beta_{takeoff,2}$	1
$\beta_{climb,2}$	0.99
$\beta_{landing,2}$	1

The overall fuel fraction for the aircraft is the product of the fuel fraction of all segments, calculated to 0.86. Using the initial estimate of $W_{TO} = 120$ lbs., the required fuel evaluates to 16.8 lbs. The weight left for fuel in the preliminary estimate was 17.6 lbs. This means that the weight class and configuration would plausibly meet the aircraft requirements, and warrants further investigation.

3.3 Configuration Design

3.3.1 Fuselage Sizing

In order to meet the payload dimensions requirement (15" x 10" x 10"), the fuselage cross section was determined.

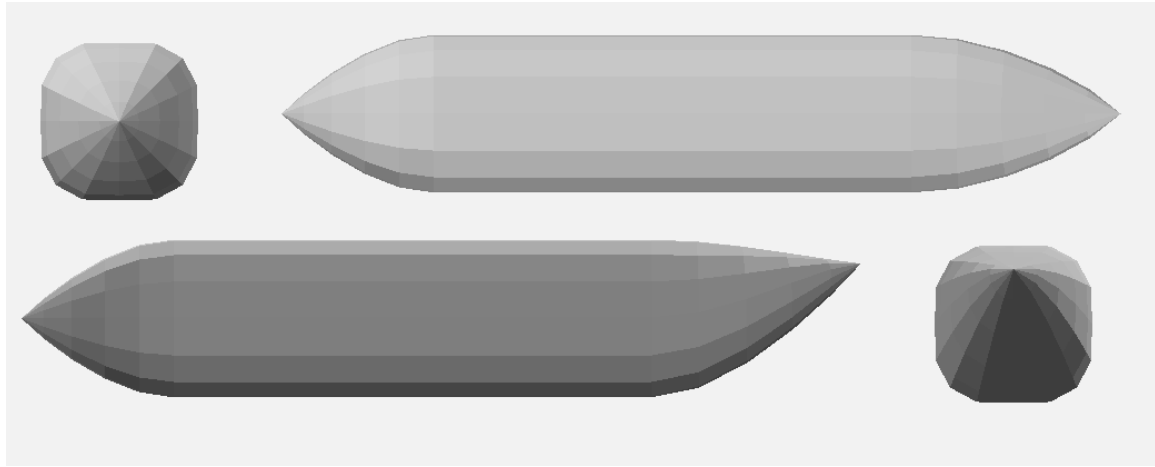


Figure 3.5: Rendering of initial fuselage in OpenVSP.

The fuselage's height and width are 10.5", and length was initially set at 56". Payload will only require 15" of fuselage length, however battery volume, fuel tank volume, gas generator volume, and other considerations must determine fuselage length.

3.3.2 VTOL Stability Considerations

EDF placement is an important consideration for stable flight in VTOL. There must be sources of Thrust in forward and to the rear of the center of gravity of the aircraft to maintain pitch control, and there must be an EDF to the left and right of the center of gravity for roll control. The fan layout is represented in Figure 3.6.

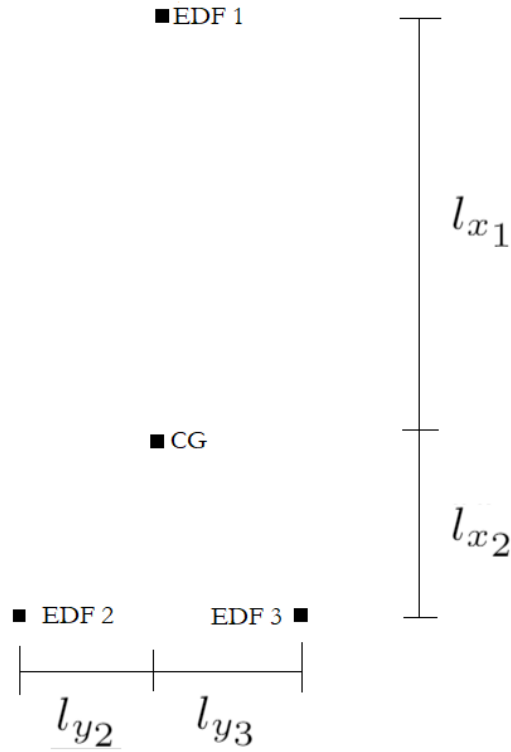


Figure 3.6: Tricopter EDF layout.

The forward propulsion system (EDF 1) was initially sized as the Vasy Fan 160mm EDF. Its diameter is 6.3”, so it can fit within the fuselage for stowage during forward flight. The rear propulsion system (EDFs 2 and 3) were initially sized as the Schubeler 195mm EDF. The ratio of rear propulsion to forward propulsion is given as:

$$\frac{T_{forward}}{T_{rear}} = \frac{33}{56 + 56} = 0.3$$

Thus, l_{x_1} should be approximately $3.33l_{x_2}$ for adequate pitch authority during VTOL.

Based on the CAD model of the fuselage, it was found that the furthest forward the forward EDF can be placed is 13.6” from the nose tip. Taking an initial estimate of 56” inches for fuselage length for housing of batteries, generator, fuel tank, and payload, and leaving approximately 12” of margin at the rear for adequate mounting of the rear EDFs, it is found that x_{cg} must be approximately 37” during VTOL.

3.3.3 Modelling Propulsion

The effects of propulsion on aerodynamics can be analyzed in OpenVSP using actuator disks. The parameters that define an actuator disk are the coefficient of thrust, coefficient of power, angular rate, and diameter. The calculations for these parameters is in Appendix A.

3.3.4 Wing, Tail, and EDF Placement

The center of gravity placement is also important for statically stable longitudinal flight. The target static margin is 0.2, which is defined as:

$$SM = \frac{x_n - x_{cg}}{\bar{c}} \quad (3.3.1)$$

Here, x_n and x_{cg} are the x-coordinates of the neutral point and center of gravity, respectively, and \bar{c} is the mean aerodynamic chord of the main wing. Based on the previous estimate of $x_{cg} = 37''$, and assuming that shifting x_{cg} between flight modes is an overly complex solution, the neutral point must obey the condition:

$$x_n > 37''$$

This indicates that the main wing must be toward the rear, approximately located with one-third of its mean aerodynamic chord at x_{cg} . A method that can be used to move the aerodynamic center further rearward is sweeping the wing. This moves the x location of the mean aerodynamic chord further rearward, which, in this case, is advantageous. Another decision was to add a kink in the wing, such that the rear fans may have room to tilt behind the swept wing, while remaining close to the center of gravity.

Figure displays a model of the kinked wing design. The total planform has a wing area of 2.69 ft^2 and an aspect ratio of 13.4.

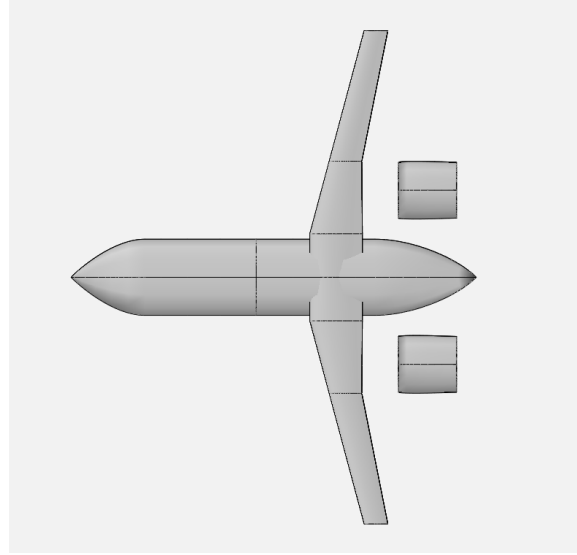


Figure 3.7: Top view of configuration with kinked wing.

The x-location of the wing is 33", and the root chord of the wing is 7.25". Since the diameter of the rearward EDFs is 7.7", in order to rotate, the x-coordinate of the EDFs must be sufficiently behind the wing to allow rotation from the VTOL configuration to the forward flight configuration.

$$x_{min,EDF} = 33'' + 7.25'' + \frac{8''}{2} = 44.25''$$

With this x-position of the rear EDFs, the moment arm balance becomes:

$$l_{x_1} = 3.23l_{x_2}$$

l_{x_1} is a slightly smaller multiple than the recommendation from section 3.3.2. The adequacy of the moment arm relations will be proven later in this thesis with simulation.

Based on the OpenVSP calculator, the length of the mean aerodynamic chord is 5.7", and the x-coordinate of the mean aerodynamic chord is 1.6" from the leading edge of the root chord. Therefore, $x_{cg} = 37"$ is located at 42% of the mean aerodynamic chord. The location of x_{cg} is slightly further toward the rear than the recommended 33% initial estimate. After the tail is added, the neutral point of the entire configuration will be analyzed to determine if adequate static margin is achieved.

Tail Sizing

The method chosen to size the aircraft's tail uses tail volume coefficients. The coefficients were chosen based on historical data for twin propeller aircraft in Roskam [13]. The resulting stabilizer areas are calculated as (see Appendix A for calculation):

$$S_{VT} = 0.55 ft^2$$

$$S_{HT} = 0.83 ft^2$$

The full configuration with tail is shown in Figures 3.8 and 3.9.

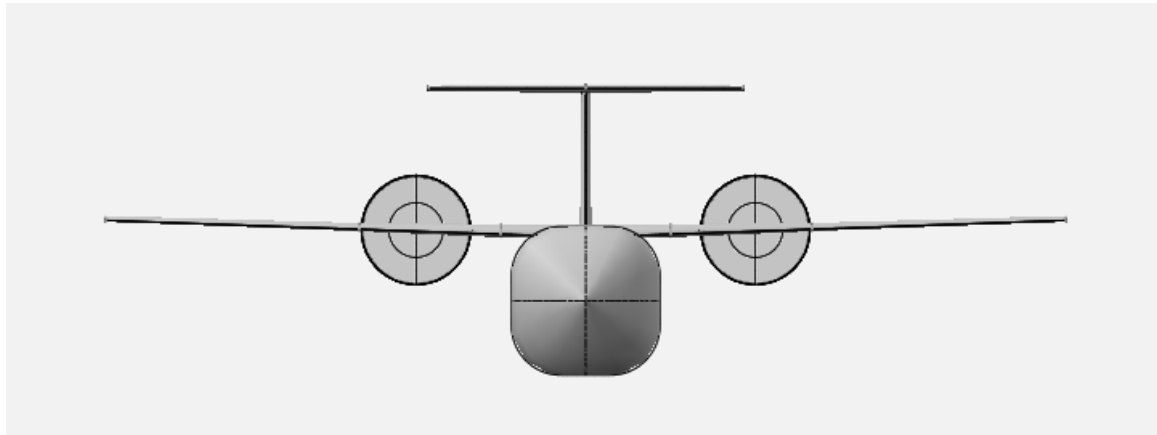


Figure 3.8: Front view of full configuration.

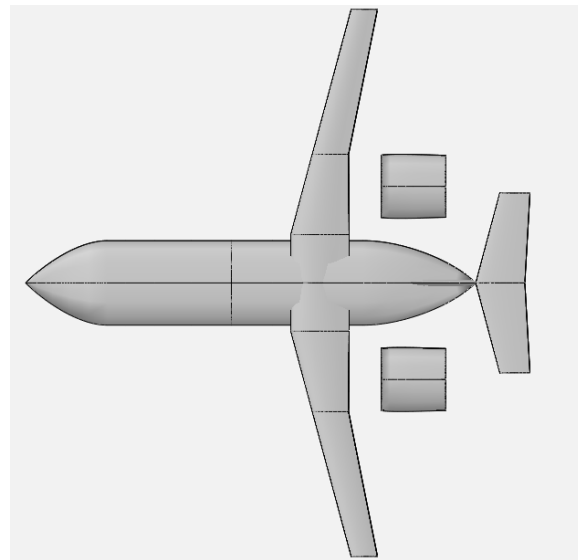


Figure 3.9: Top view of full configuration.

Neutral Point

To determine the static margin of this configuration, the neutral point must be calculated. The relevant equation to calculate the neutral point is:

$$\frac{x_n - x_{ref}}{\bar{c}} = \frac{x_{ref}}{\bar{c}} - \frac{\partial C_{m_{ref}}}{\partial C_l} \quad (3.3.2)$$

After a run of the full configuration in OpenVSP, $\frac{\partial C_{M_{ref}}}{\partial C_L}$ was calculated to be -6.75 (see Appendix A). Using Equation 3.3.2, the neutral point is determined to be located at $x = 38.3''$. Using equation 3.3.1, the static margin is determined to be 0.22. This surpasses the goal of 0.2, but careful care must be taken to make certain that the static margin does not decrease too greatly with x_{cg} shifts.

3.3.5 Aerodynamic Performance

Increased Aspect Ratio

After arriving at the full configuration, VLM in VSPAERO was utilized to analyze the aerodynamic performance. Figure 3.10 shows the trailing wakes generated in VSPAERO.

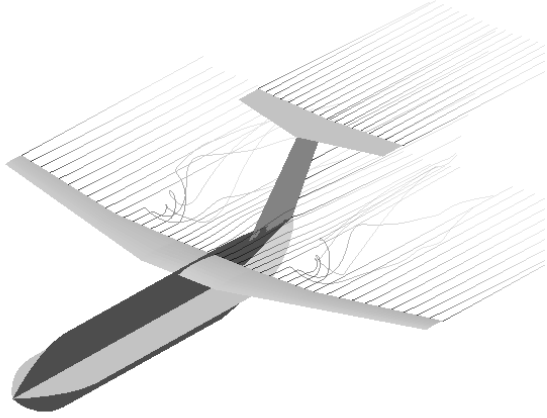


Figure 3.10: Trailing wakes generated by VSPAERO for full configuration

The L/D vs. α plot that results from this VSPAERO run is shown in Figure 3.11.

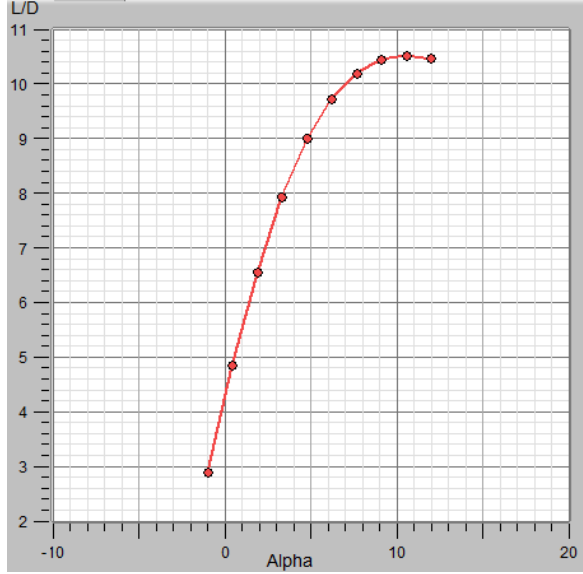


Figure 3.11: L/D vs. α for full configuration.

The maximum L/D is approximately 10.5. With some calculation, it was found that a L/D this low would put power requirements above that which the researched generator could provide, and would not allow the aircraft to meet the 500 mile range requirement. In order to solve this problem, it was decided to increase the aspect ratio of the aircraft to achieve better aerodynamic performance.

After some iteration, an aspect ratio of 17.3 was chosen. The results of the VLM run are shown in Figure 3.12 and the updated configuration is displayed in Figures 3.13 and 3.14.

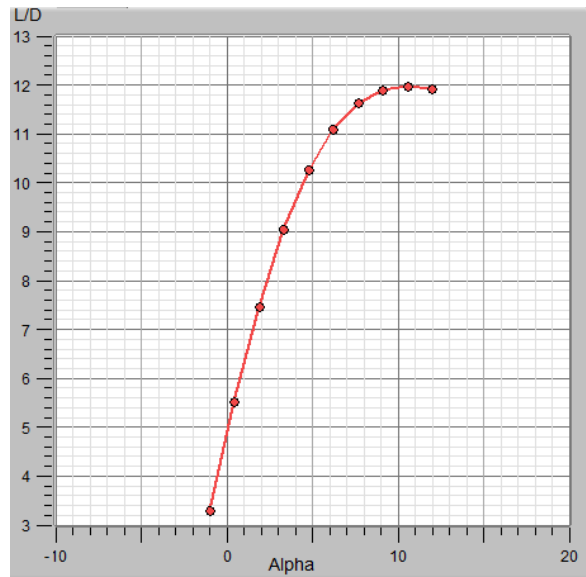


Figure 3.12: L/D vs. α for the new configuration.

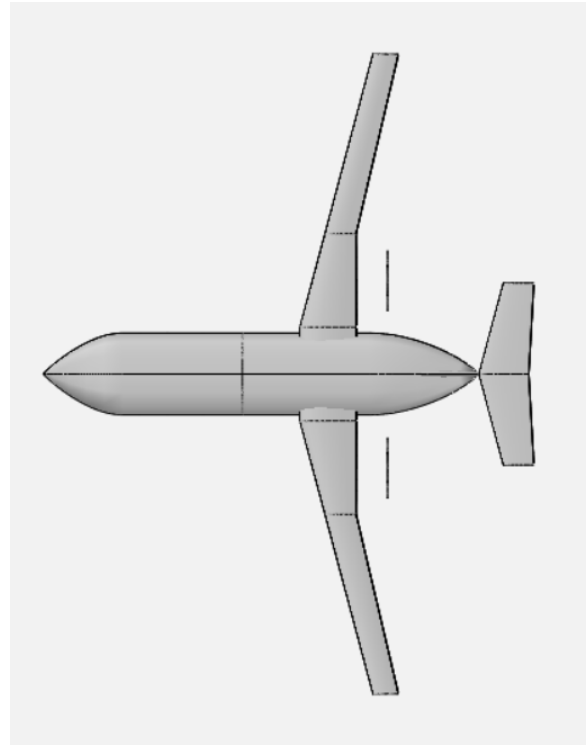


Figure 3.13: Top view of new configuration.

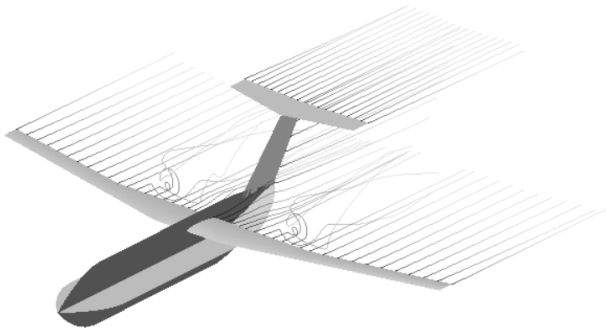


Figure 3.14: Trailing wakes on new configuration.

Wing Incidence Angle

Based on the results shown in Figure 3.15, it is apparent that the maximum L/D occurs around an angle of attack of 10 degrees. This would be a large trim angle of attack, so a wing incidence was implemented. After some iteration, a wing with an incidence angle of 6 degrees was chosen. The result of this VSPAERO run is shown in Figure 3.15.

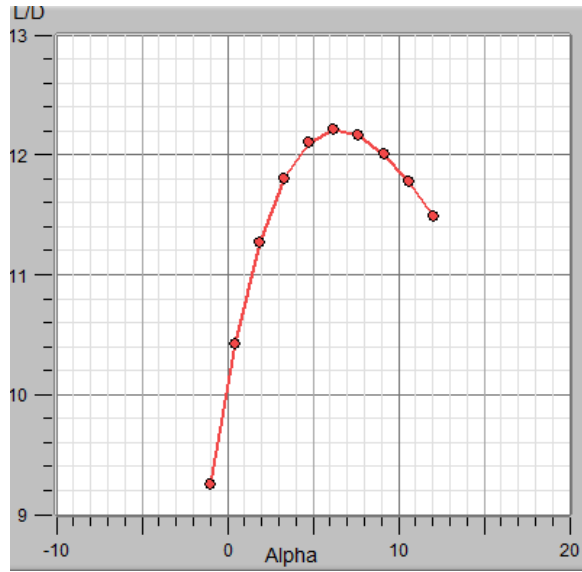


Figure 3.15: L/D vs. α for full configuration, 6° wing incidence.

At an angle of attack of 6°, we find that L/D reaches a maximum of 12.2. Thus, $\alpha_{trim} = 6^\circ$ and L/D= 12.2

Dihedral Angle

For roll stability, a 2° dihedral angle was added to the wing. The configuration with updated incidence and dihedral angles is pictured in Figure 3.16.

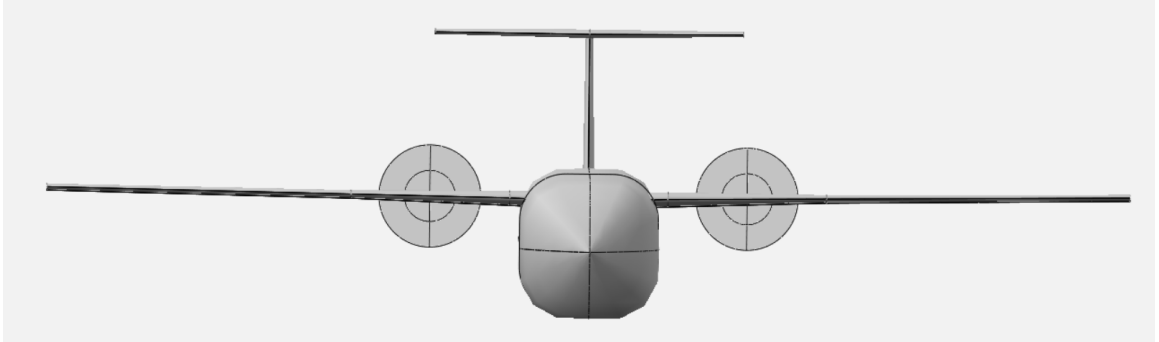


Figure 3.16: Front view of final configuration with 6° wing incidence and 5° dihedral

Updated Neutral Point

The wing has been changed, so the neutral point must be recalculated. The new \bar{c} is 5.50" and $\frac{\partial C_{M_{ref}}}{\partial C_L} = -7.00$. Therefore, $x_n = 38.5"$, and $SM = 0.27$. See appendix A for calculation.

3.3.6 Power Requirements

The power requirements can now be reevaluated based on the L/D obtained from the VSPAERO runs of the full configuration, assuming the L/D ratio is constant over all flight modes.

Climbing

We can determine the power requirement for climb from the equation for climb rate.

$$\frac{dh}{dt} = V \sin(\gamma) = V \frac{T - D}{W} = SEP \quad (3.3.3)$$

Here, SEP is specific excess power. The Power requirement is determined from power balance.

$$P_{req} = WV \frac{1}{\frac{L}{D}} + W * SEP \quad (3.3.4)$$

The generator power requirement is defined using Equations 3.2.7 and 3.3.4.

$$P_{req,generator} = \frac{1}{\eta_o} (\beta_i W_{TO} V \frac{1}{\frac{L}{D}} + \beta_i W_{TO} * SEP) \quad (3.3.5)$$

Cruising

The power requirement during cruise is given by

$$P_{req,generator} = \frac{1}{\eta_o} (\beta_i W_{TO} V \frac{1}{\frac{L}{D}}) \quad (3.3.6)$$

3.3.7 Updated Fuel Fractions and Range

As a result of the sizing process, the fuel burn and range over flight modes can be obtained. The power and fuel budget is displayed in Table 3.4.

Table 3.4: Fuel and Power Budget

Mode	t(s)	W(lbs)	P_b (kW)	E_b (kWh)	P_g (kW)	β	R(mi)
VTOL 1	30	120	45.2	0.375	0	0	0
Climb 1	103	120	1.8	0.045	4	0.999	4.3
Cruise 1		119.8	0	0	3.99	0.932	245.7
VTOL 2	30	111.7	45.2	0.375	0	0	0
Payload Removed							
VTOL 3	30	86.7	30	0.25	0	0	0
Climb 2	103	86.7	0.22	0.006	4	0.998	4.3
Cruise 2		86.5	0	0	2.88	0.932	245.7
VTOL 4	30	80.6	30	0.25	0	0	0
Total				1.05		0.866	500

For all calculations, see Appendix A.

3.3.8 Control Surface Sizing

The control surfaces were sized using historical data for twin-propeller aircraft in Roskam[13]. The calculation script is located in Appendix A. The calculated values are displayed in Table 3.5.

Table 3.5: Control Surface Parameters

Aileron area	0.17 ft^2
Aileron inner chord	0.14 ft
Aileron outer chord	0.13 ft
Aileron inner span location	2.05 ft
Aileron outer span location	3.08 ft
Elevator area	0.34 ft^2
Elevator root chord	0.18 ft
Elevator tip chord	0.17 ft
Rudder area	0.25 ft^2
Rudder root chord	0.29 ft
Rudder tip chord	0.24 ft

This concludes the sizing section of this thesis. The parameters determined throughout this section will now be synthesized throughout the detailed design and analysis sections to further demonstrate the feasibility of the proposed aircraft.

Chapter 4

Detailed Design

4.1 Powertrain

4.1.1 Propulsion

The design of the powertrain began with selection of a propulsion system. Electric motors in general offer many key advantages that make them an ideal choice for VTOL. Of note is the fact that electric motors are more efficient over a wider range of power outputs. Internal combustion engines(ICE) that provide enough thrust for hover can not be throttled down to meet the much lower power requirements of cruising flights without suffering huge losses in efficiency. More importantly, EDFs can be powered by batteries charged using clean sources of energy. Electric vehicles will be a major if not dominant player across all aspects of transportation and logistics. Among the options for electric motors. Electric ducted fans (EDFs) were selected as they offered a much higher thrust to disk size ratio compared to traditional propellers. EDFs reportedly create less noise pollution during operation. Lastly, the ducts shield people and property from the dangers of large blades spinning at high speeds. Public acceptance will play a major part in the widespread roll out of autonomous UAVs. Ducted fans result in a smaller, quieter, and safer vehicle, all of which are essential for any widely adoptable UAV technology.

4.1.2 Hybrid Electric

The ultimate goal of this project is to design a vehicle that is viable in the immediate and near future. Simply put all electric vehicles are likely to be the dominant form of

transportation moving forward. After evaluating possible designs to fulfill the chosen mission profile, it was readily apparent that today's battery technology is not yet sufficient for large payloads and long ranges. Current lithium based battery energy densities range from 150-200 Wh/kg. Battery densities of at least around 500 Wh/kg are likely to be needed before fully electric propulsion becomes the dominant system in aviation. In order to build a drone with commercial viability today, but long term viability moving forward, a hybrid electric system was chosen. In this system, a combination of battery packs and internal combustion engines are used.

The two forms of hybrid electric systems in propulsion are parallel hybrid and serial hybrid. In parallel hybrid systems, the ICE provides a portion of the overall propulsion power either by being connected to the same propeller shaft as the electric motors via a gearbox, or the ICE is connected directly to a different propeller than the electric motor and both propellers provide thrust.

In contrast, a serial hybrid electric powertrain uses electric motors to generate thrust. The source of the electricity can be from onboard batteries, or from an ICE connected to a generator.[7] In this configuration, batteries often provide the majority of power during takeoff, and the ICE acts as a range extender.

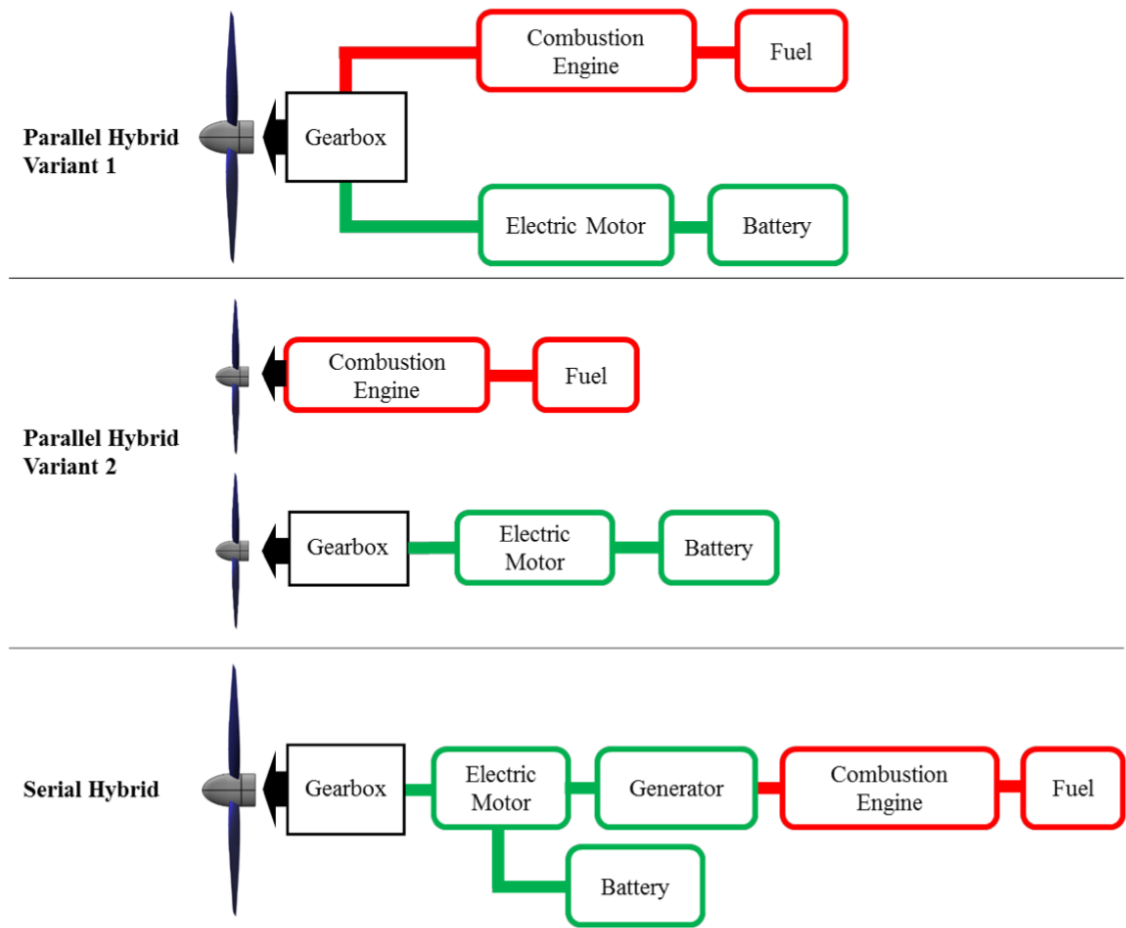


Figure 4.1: A comparison of serial and hybrid electric systems.[7]

A serial hybrid-electric configuration was chosen for this vehicle in order to use the Electric Ducted Fans, as well as to future-proof the vehicle. When battery technology reaches a critical energy and power density threshold, the ICE and fuel tank can be easily switched out for extra battery cells.

4.1.3 Batteries

Although a variety of battery chemistries exist, aerial vehicles generally only choose between the two most mature and readily available chemistries: Lithium Ion (LI-ION) and Lithium Polymer (LIPO). LIPO batteries were selected as their higher discharge capacity is better suited to the high current demands of the EDFs during VTOL, but LION batteries tend to be easier and cheaper to work with in a mass manufacturable

design.

In addition to considering different battery chemistries, different battery configurations were evaluated. Structural batteries, a design where the battery pack bears load and acts as part of the mechanical structure, are a very attractive option for UAVs due to their potential weight savings. The electric vehicle market, both aerial and ground, will likely move towards these types of battery packs as their benefits become more thoroughly understood and methods to cheaply manufacture them are developed. The vehicle outlined in this thesis would benefit from structural batteries, and may even implement them if the full scale design is actualized, but the design of a structural battery pack is outside the scope of this project. Instead, battery packs were designed by wiring together readily available lithium polymer cells wired in series and/or parallel.

Takeoff Sizing

Each motor had its own dedicated battery pack. The battery pack sizing begins by satisfying the max power requirements of the system during takeoff. Starting with the vehicle's max takeoff weight and a desired thrust to weight ratio, a required takeoff thrust is calculated. Using the motor curves provided by the manufacturer, a voltage corresponding to that thrust can be determined. This is the maximum voltage the system would need. Dividing the max takeoff voltage by the nominal voltage of each cell (usually around 3.6V) gives an estimate for the number of cells in series for that battery pack

Endurance Sizing

The total energy stored within the battery pack is determined by the capacity of each cell, but can be increased by wiring more cells in series. The total time the vehicle is hovering under battery power can be determined from the mission profile. Multiplying the average power requirement of the motor during VTOL by the total time the vehicle is using battery power for VTOL gives the total energy capacity required from the battery pack. Dividing the total battery capacity required by the battery capacity of one cell gives the number of cells required to be wired in series. A matlab script was created to optimize the total battery pack weight according to the mission profile, motor curves, and characteristics of readily available battery cells.

For each of the rear EDFs, a battery pack would be created using 14 cells wired in series and 2 cells in parallel. The cells used in this design was the GRP7945135 from

Grepow with a 30C discharge rating, a 4400mah capacity, and weighing 93 grams. The combined weight of the battery packs for the rear EDFs is 5208 grams.

For the front EDF, a battery pack would be created using 13 cells in series and 1 in parallel. For ease of manufacture, the pack could be made using 14 cells in series. The cells used in this pack would be the GRP8945150 from Grepow with a 35C discharge rating a capacity of 6000mah and weighing 128 grams. [6]

The battery pack could be optimized further in future research.

4.2 Structures and Airframe

4.2.1 Internal Frame

With the goal of producing a UAV that could be easily assembled and developed as a prototype vehicle, the general design of the airframe was centered around a body-on-frame approach, despite lower structural efficiency when compared to a more optimized monocoque frame. To save on weight, composites such as carbon fiber reinforced plastic were a preferred material choice; however, due to the complications involved in achieving sufficiently isotropic properties from accessible methods (such as pre-preg layup over custom printed molds), off the shelf components in the form of roll-wrapped tubing and carbon fiber plates were a first-choice for assembling the basic frame of the vehicle.

The underlying skeleton of the UAV was constructed around 4 spars that ran lengthwise along the longitudinal axis, braced with CFRP plates for mounting points and reinforcement. The three primary motivations for this approach were the availability of low-cost pre-made components, the ease of custom manufacturing via a laser-cutter for any parts cut from stock plate material, and the unbeatable strength-to-weight ratio of carbon fiber composites. Following construction and assembly, a lightweight non load-bearing outer fuselage hull will be custom-manufactured from low weight plastics for aerodynamic shielding. Figure 4.2 shows the general approach to early frame iterations designed with this while Figure 4.4 shows the how the external skin overlays the internal skeleton. In order to ensure no significant transmission of load to the outer skin, which is anticipated to be vacuum-formed ABS Plastic segment in early iterations)

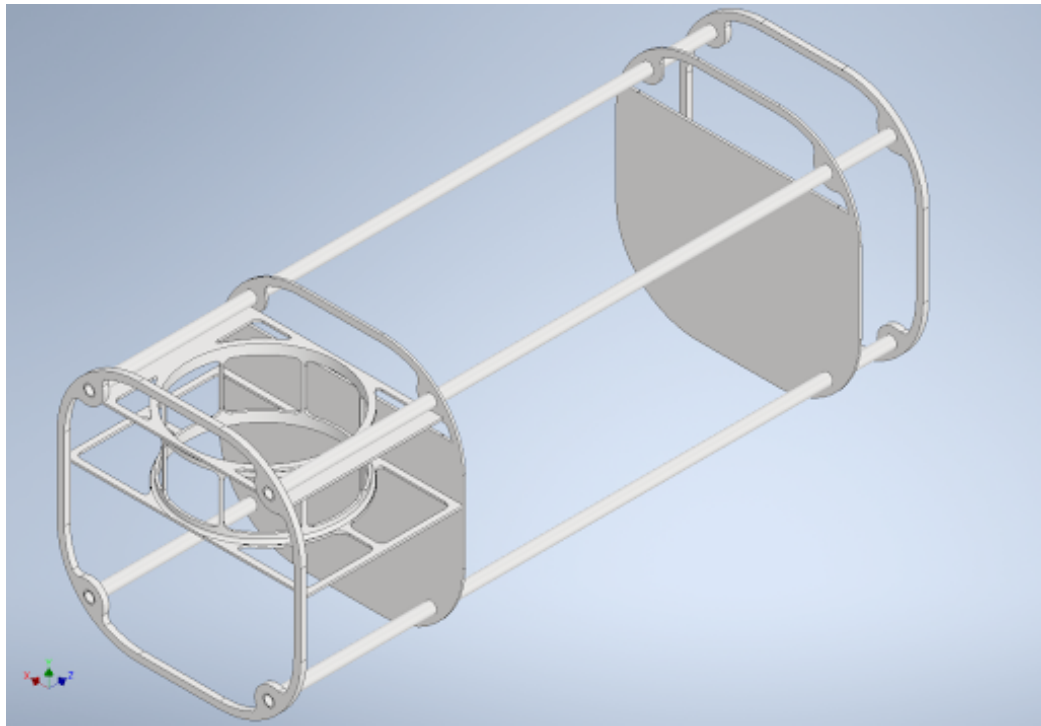


Figure 4.2: Early Internal Frame Iteration

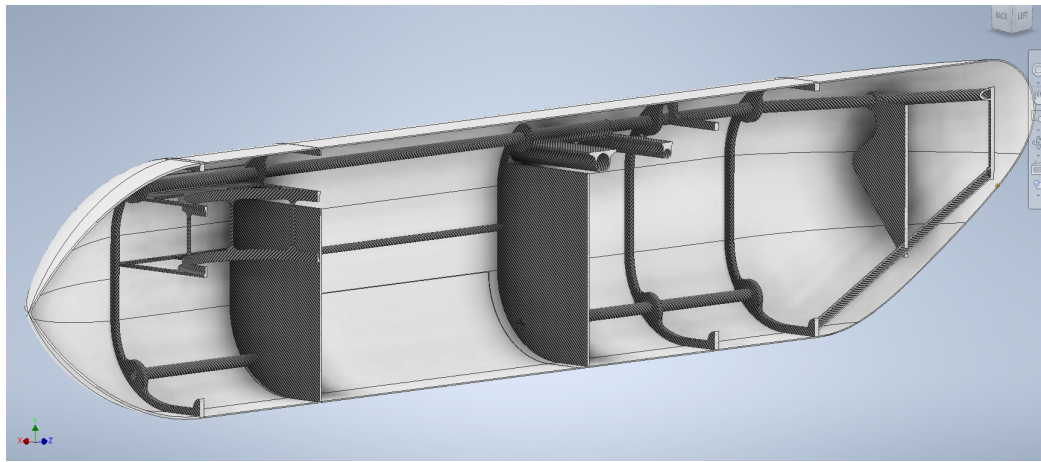


Figure 4.3: Fuselage Frame and Skin.

As discussed in earlier sections, the fuselage geometry was already roughly determined based on the payload volume requirements and Open VSP sizing. Additional adjustments were made in order to account more specifically for housing components such as the front EDF, the internal combustion engine and accompanying support equipment, and the large volume of batteries required for VTOL flight. With these,

an internal skeleton was iteratively developed to fit within a close approximation of the OML created in VSP, with space allocated for each major system, distributed according to initial CG placement estimates. Figure ?? shows this compartmentalization. Due to the wide distribution of batteries throughout the entire frame, they are not given a dedicated section in the figure, though they are primarily placed above the payload bay. A full view of the frame alone is shown in Figures 4.5. The final iteration of the fuselage frame is shown in Figures 4.12 and 4.5. The total weight of the CFRP fuselage skeleton without skin was 2.965 lbs.

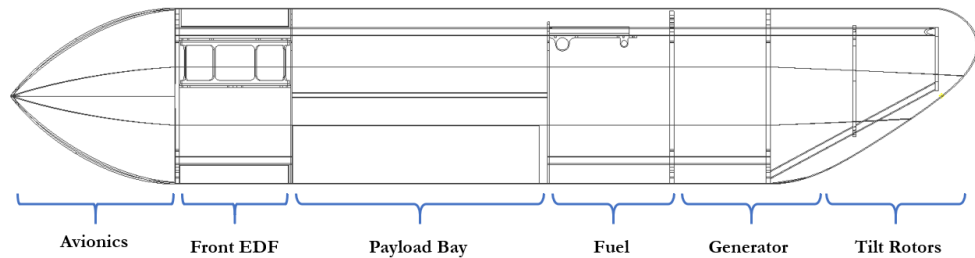


Figure 4.4: Fuselage Frame and Skin - Cutaway View

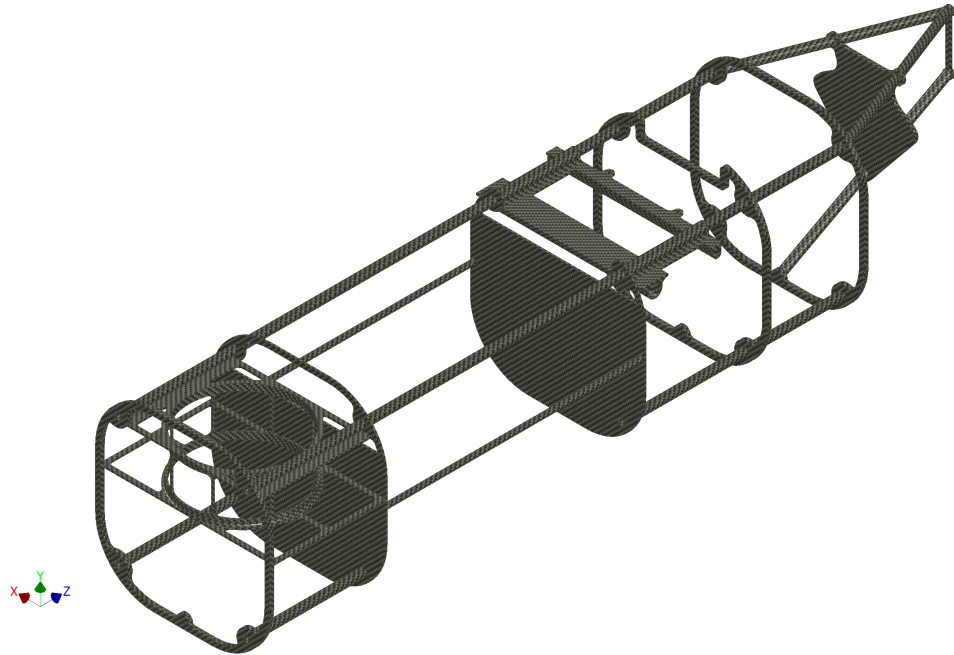


Figure 4.5: Final Fuselage Internal Frame (no mesh)

The entire front mount, shown in Figure 4.6, is intended to be assembled from two 0.1" thick carbon-fiber plates, laser-cut to dimension, and braced in the y-axis (as

defined in Figure 4.6) by additional strips of CFRP. All 3 components will be epoxied together, and then epoxied to the frame, as there is no anticipated need to remove this front mount in the future. Further, the outer shell of the front 160mm fan will be secured permanently to the mount with epoxy, as the internal motor and blades can be removed separately from the housing if maintenance is needed or damage is sustained.

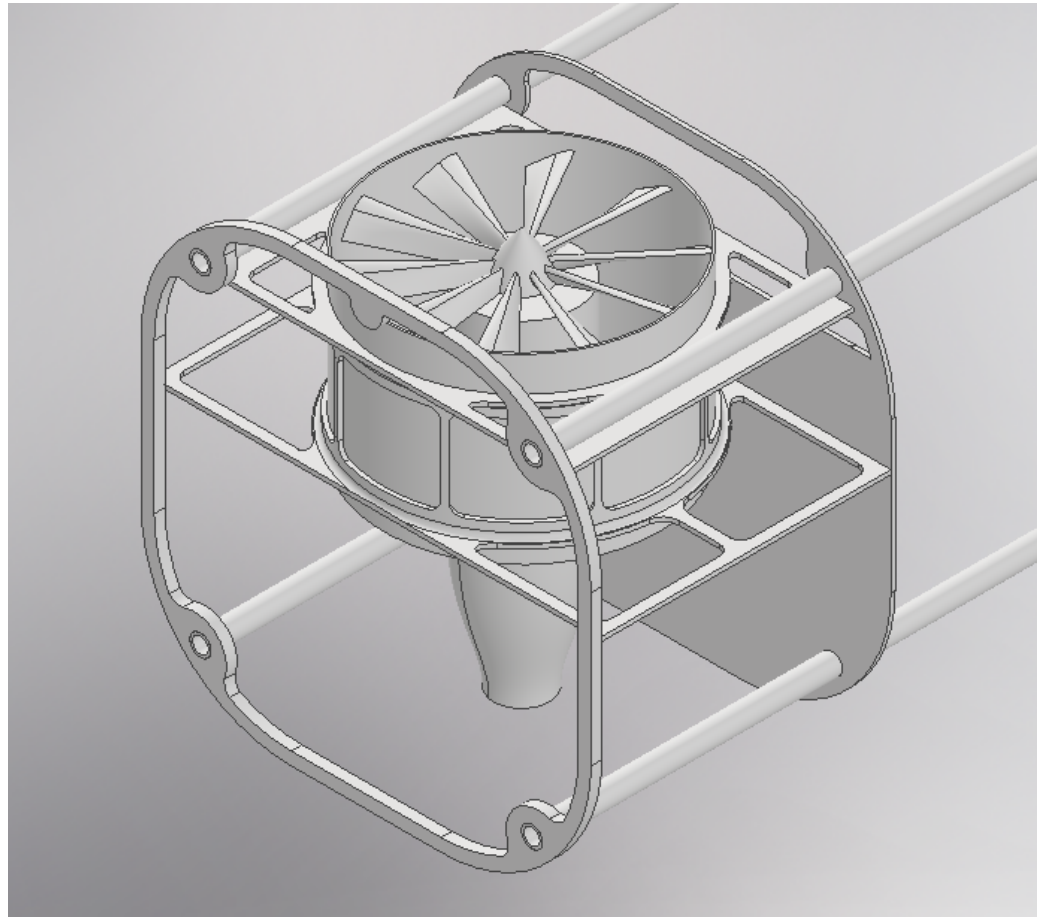


Figure 4.6: Front EDF Mount

The rear EDFs were both mounted to a rigid shaft which was fed through two bearings in the empennage, actuated by a 90 degree pneumatic rotary vane (See 4.5 for more detail regarding actuator mechanisms).

Wing Mounts

The wings have two spars formed from two different sizes of CFRP roll-wrapped tubing that extend beyond the root chord to fasten onto the main fuselage frame.

The body wing-mount, shown in Figure 4.7 is formed from 4 CFRP roll-wrapped tubes, 2 of which are sized within tolerance to act as sleeves for the frame, and 2 of which are sleeves for the wing spars. This mount is shown integrated into the overall frame in Figure 4.8 To fasten the wing in place, as shown in Figure ?? 2 10-24 bolts are screwed through the sleeve, the wing spar, and an internal mandrill (to prevent collapse of the thin-walled wing spar tubes), along with a cylindrical washer to apply clamp pressure to increase the surface area of the overall connection and reduce the likelihood of tearout. There are no substantial loads expected along the length of the spar, and the wing mount sleeve bears the majority of the aerodynamic loading from the wings. The shear strength of the steel bolts, at 150,000 psi, will not be exceeded, as even under the anticipated straight-and-level flight condition of 60lbs per wing, the anticipated shear stresses barely exceed 1000 psi with a simple back-of-the-envelope calculation of $\frac{F}{Area_{bolt}} = \tau$. Additionally, there are 6 holes drilled into the frame, which will act as a mounting surface for the ICE's radiator.

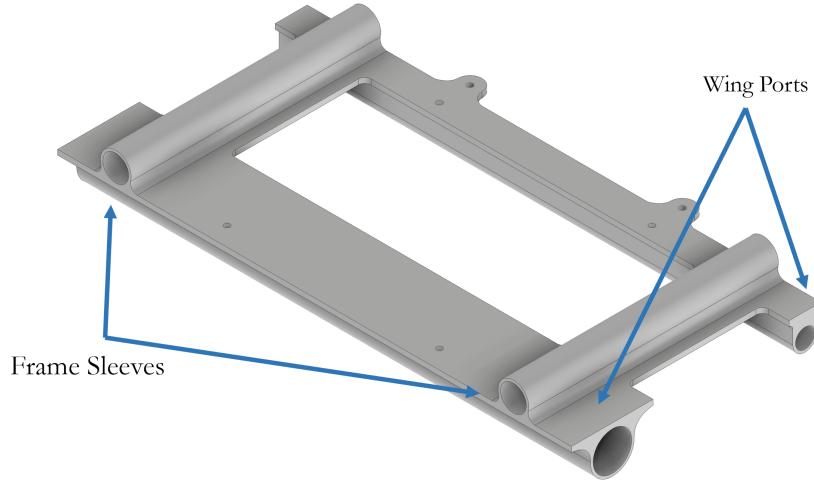


Figure 4.7: Main Wing Mount

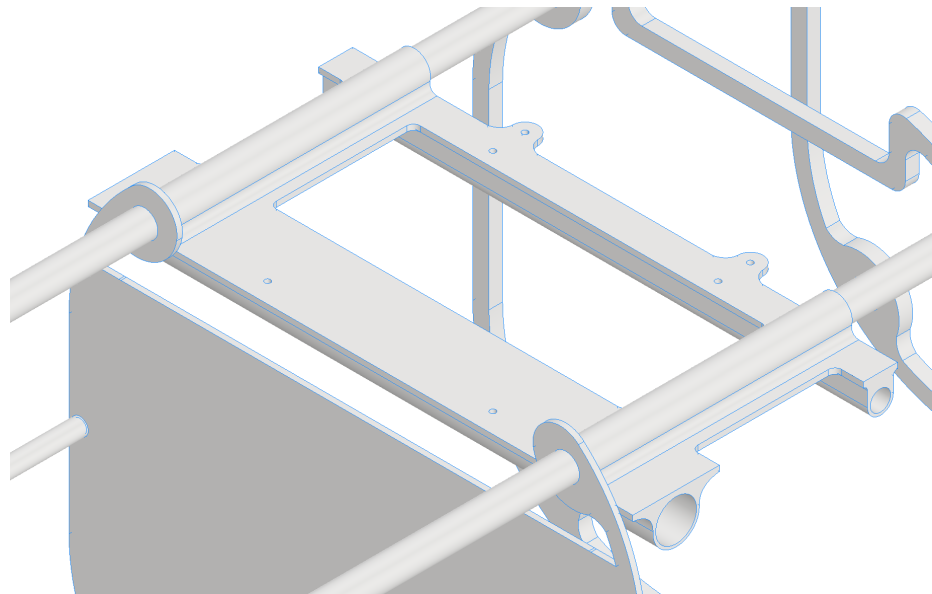


Figure 4.8: Installed Wing Mount

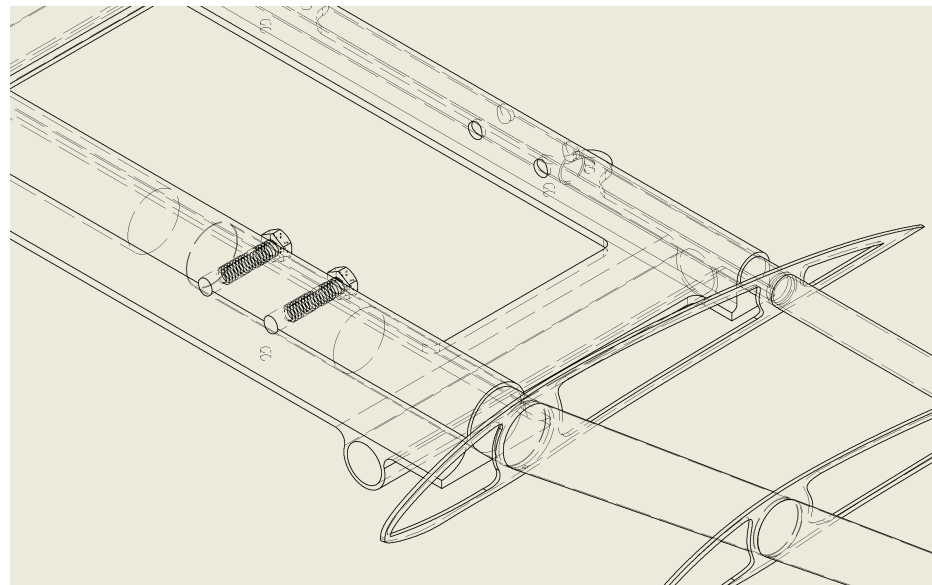


Figure 4.9: Wing Fasteners with Internal Mandrill

The wing-mount plate is manufactured from 3 CFRP tubes, 2x of ID 0.5", 1 of ID = 0.75", and 1 with ID 0.375", and one plate of 0.1" thick CFRP. Generous application of epoxy is currently proposed as the method of assembling these components; however, due to the potential alignment issues, potential for tolerance issues, and the robustness of the current component, molding the tube fittings around a stock

CFRP plate with epoxy and shredded carbon fiber filaments has been considered as a potential alternative method for manufacture.

Engine Mount

Due to a non-disclosure agreement (NDA) signed with the manufacturer of the internal combustion engine chosen for this vehicle, specifics regarding the integration of this system with the UAV will not be provided; however, general purpose diagrams demonstrating how the the engine and its support equipment were mounted in the frame are shown in Figures 4.10 and 4.11.

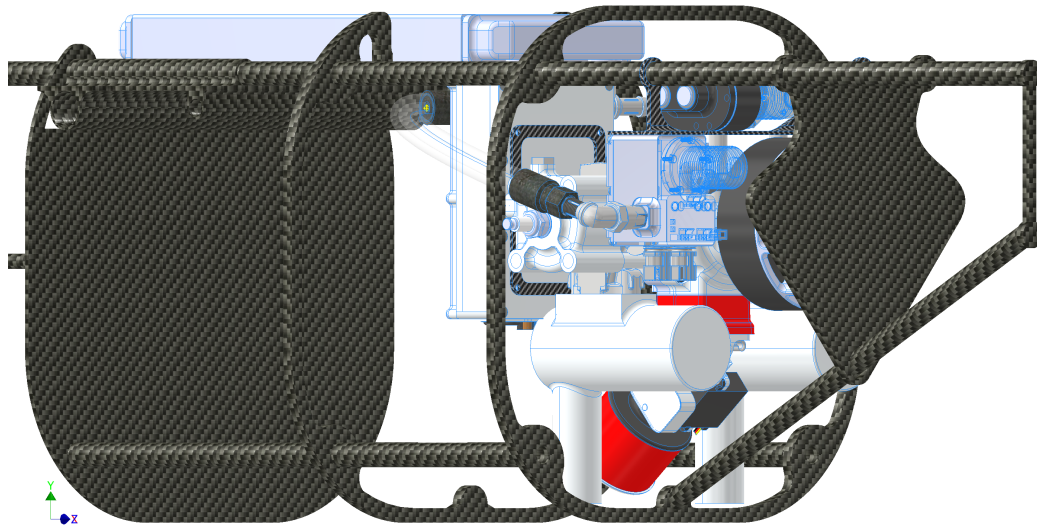


Figure 4.10: Fully Integrated Pegasus GE70

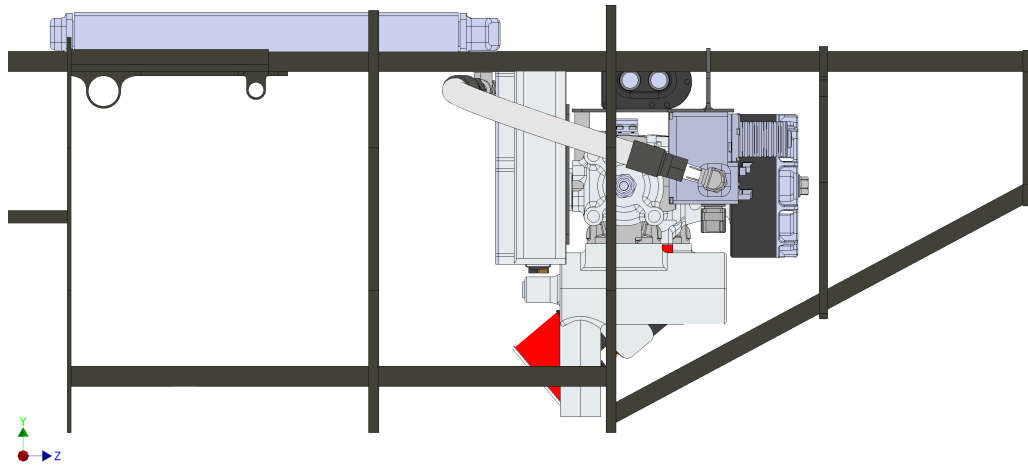


Figure 4.11: Pegasus G70 Mount (view 2)

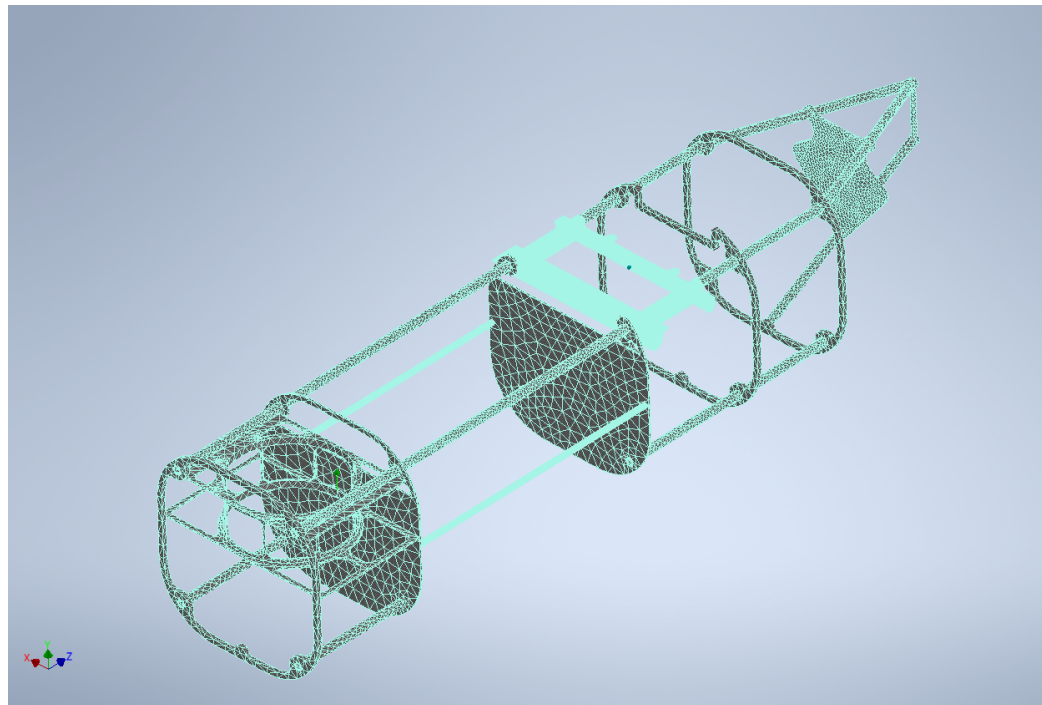


Figure 4.12: Final Fuselage Internal Frame (mesh)

4.2.2 Fuselage Skin

As mentioned previously, the fuselage skin was purely in place for aerodynamics and shielding components and was not intended to be a load-bearing element. As a result, 0.05" ABS plastic was chosen as a cheap, flexible, somewhat durable material for use

in the prototype vehicle as a skin. Additionally, its ability to be easily vacuum-formed to a mold allows for easy iteration on the manufacture of different panels and their placement. The fuselage is to be separated into multiple sections and epoxied to the frame where possible, while panels over sections that may require frequent maintenance, such as the ICE, fuel tank, or electronics bay, will be fastened to the frame via screws that secure to each bulkhead with L brackets. Holes are cut out from the airfoil shapes of intersection for both the vertical stabilizer and the wings, as labeled in ??

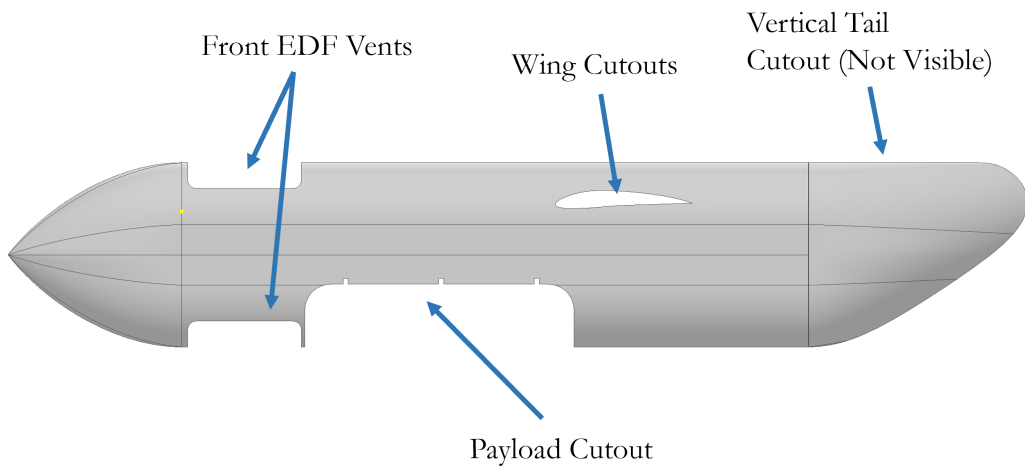


Figure 4.13: Labeled Skin (Assembled Panels)

Further, the fuselage skin is equipped with three cutouts, 1 of which serves as an opening for the payload compartment to deposit packages, while the other two serve as covers for the front EDF during cruising flight. Each door is formed from lightweight ABS and is actuated by the vehicle's pneumatic system, as discussed in Chapter 4.5. A cutaway view of the doors can be seen in 4.14 while 4.15 and 4.16 provide additional views of the components involved in the skin assembly.

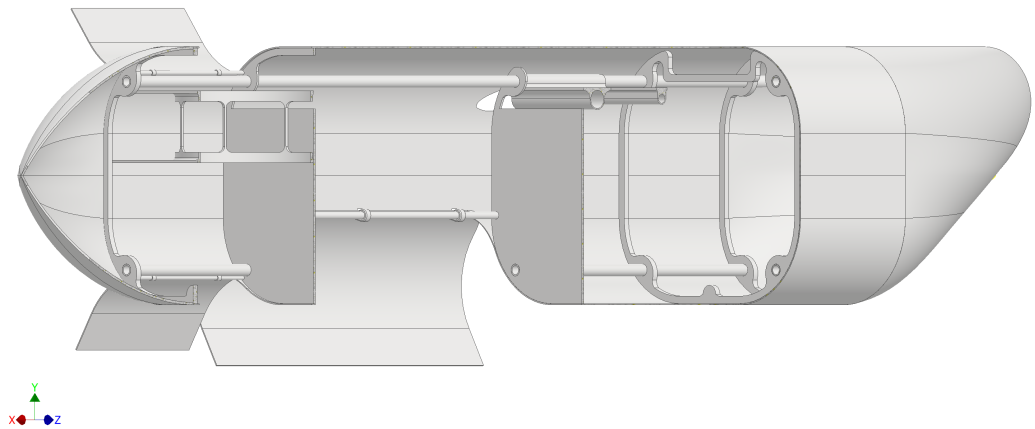


Figure 4.14: Cutaway view of payload skin with frame (doors open)

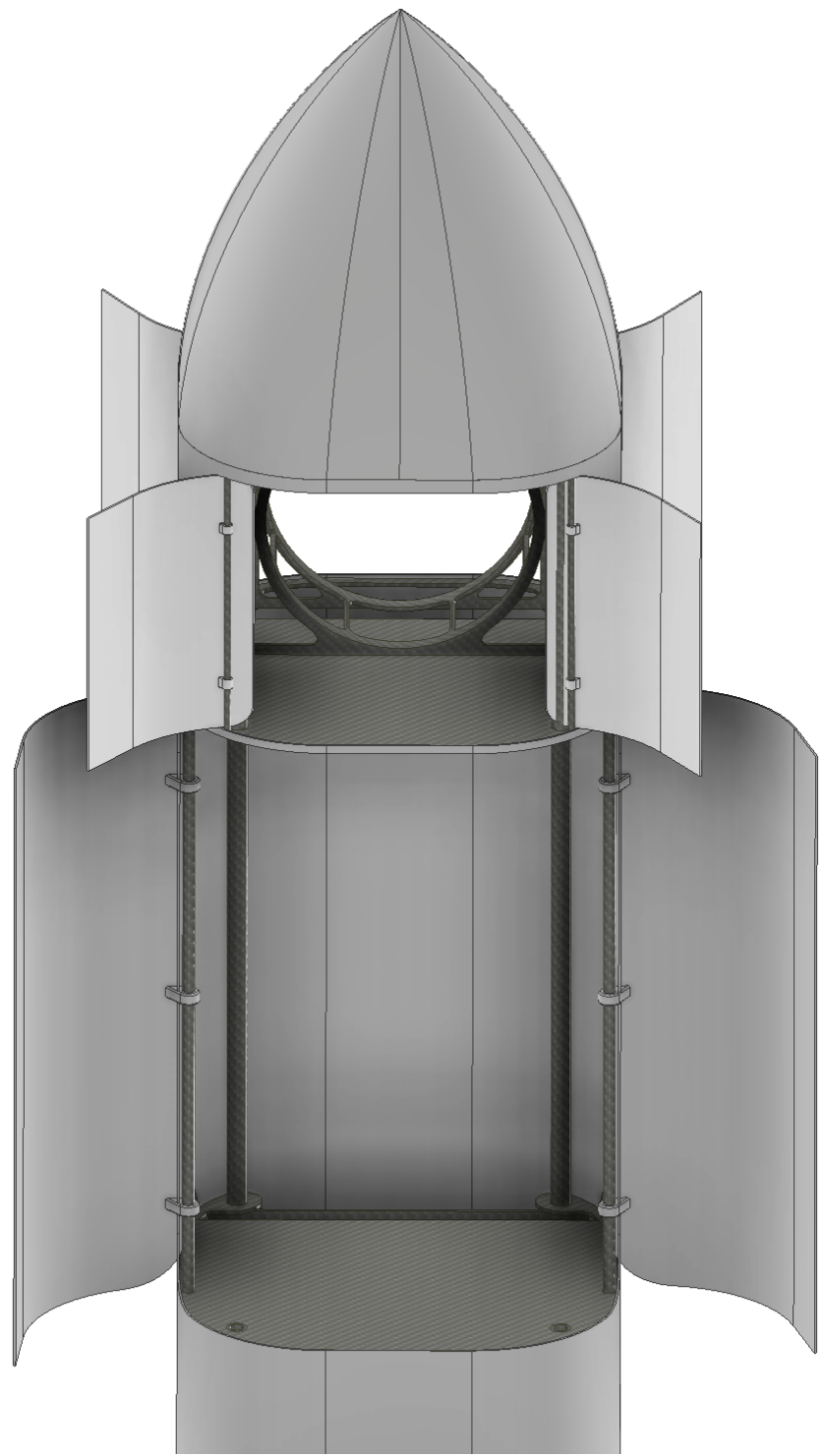


Figure 4.15: Bottom view of payload and EDF doors

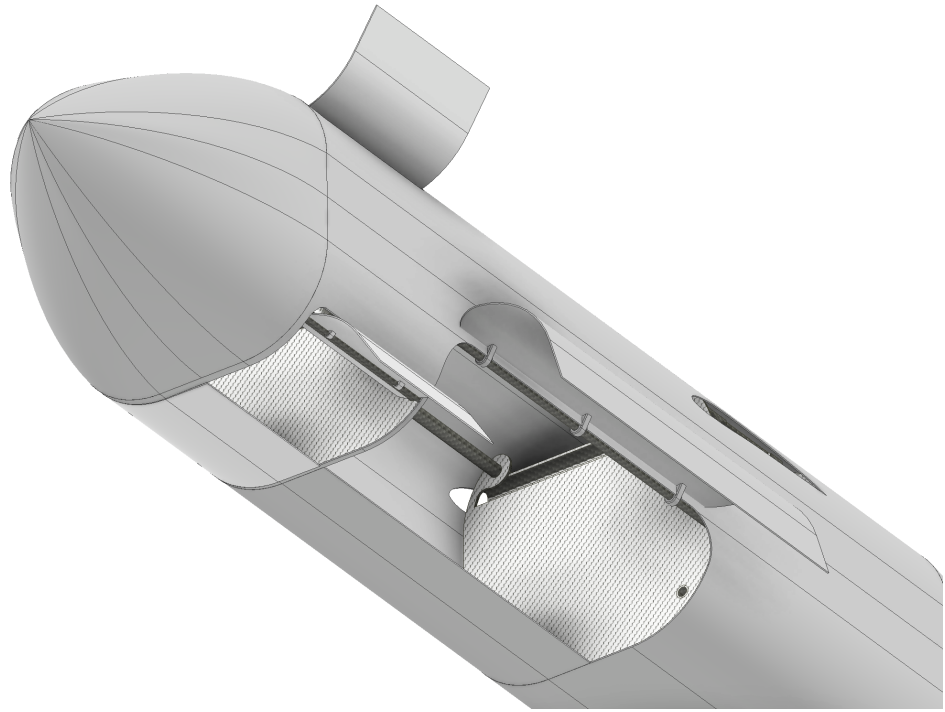


Figure 4.16: Representative view of skin assembly and half doors open

4.2.3 Wings and Tail

Four primary factors contributed to the weight of the final wing design: The high AR, the mid-spar break for the folding mechanism, the use of the wings as landing-gear, and the kink in the planform to avoid physical interference with the rear EDFs.

In order to maintain the small desired footprint of the craft, a folding-wing mechanism was implemented, allowing for improved aerodynamic characteristics in cruise with a small vehicle size during VTOL operations. Overall, folding the wing reduces the entire width of the vehicle to around 3 ft total on the ground, reducing total span by approximately 3.7 ft. Additionally, the sensitivity of the configuration’s L/D to small adjustments in physical geometry led to the decision to not use fixed landing gear and to instead implement a form of folding landing gear. With the fuselage alright under tight volume constraints, the feasibility of using the folded wings as two landing gear was explored.

The wing design was one of the more complicated structural tasks due to the decision to attempt to combine the folding-wing mechanism with the landing gear. While unconventional, it presented a promising way of combining both tasks into one and reducing the number of mechanisms required. When used as landing gear, the

heavy loading requirements placed on the relatively narrow outboard portions of the swept wing resulted in significant risk of buckling. As a result, while the rest of the fuselage is constructed with a light-weight, non-load-bearing ABS plastic for ease of manufacturability, the outer portion of the wings past the hinge must be constructed with a stressed CFRP skin layup in order to prevent buckling. The resulting wings were significantly over-engineered for landing in comparison to the loads sustained during flight; in the future, this design consideration would likely be revisited to consider the weight trade off of including a separate landing-gear mechanism in the body, allowing for weight reduction of the wings.

The tail employed a similar rib-spar design, manufactured by the same methods as the wing. The same sleeve-bolt mechanism as described in Figure 4.8 was used to secure the main spar, and an image of the final T-Tail empennage structure is shown in Figure 4.17. The same bolts were used to secure the horizontal stabilizer to the vertical tail for ease of disassembly.

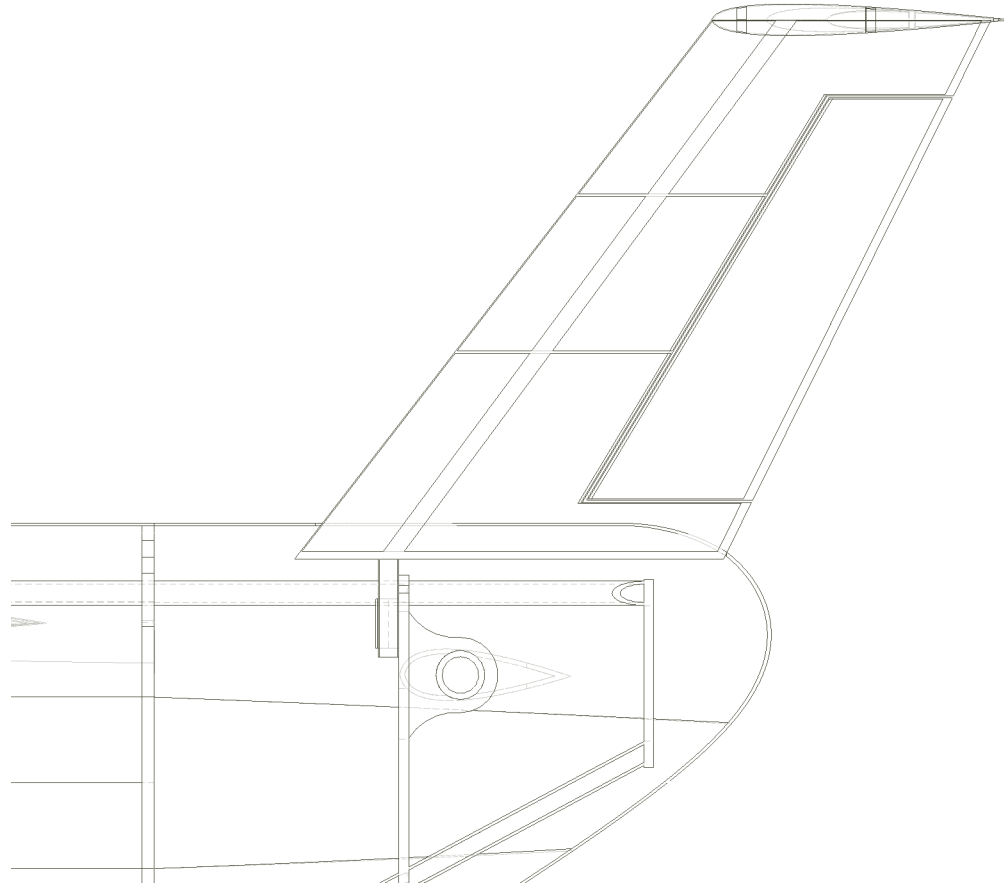


Figure 4.17: T-Tail Installation and Structure

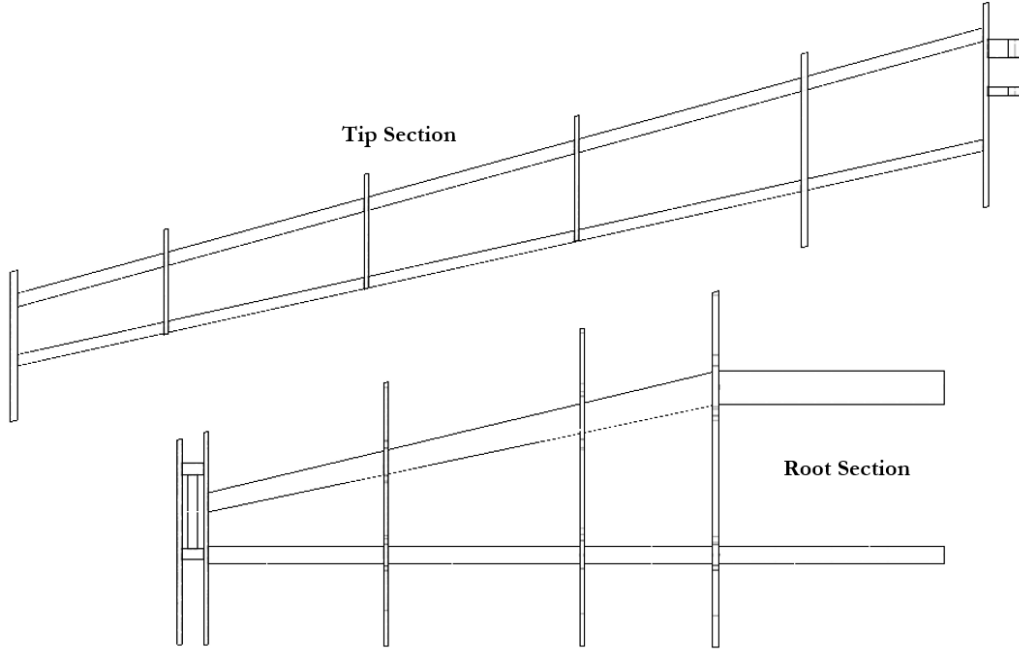


Figure 4.18: Two-Part Wing

As shown in figure 4.18, the wings are divided into two sections: the root and the tip. The tip begins at the hinge-point for the landing gear, and is constructed from two primary spars from stock CFRP tubing. The main spar in the root section of the wing is tapered to both reduce weight and compensate for the change in cross section due to the smaller chord at the tip.

Each rib within the wing will be laser cut from 0.1" thick CFRP plates using leftover material from sections cut out for the fuselage and other component mounts. When fitted over the spar, they will be epoxied into place, as the root and the tip are manufactured as separate pieces. Epoxy will be used to bond all laser-cut components as shown in the complete wing assembly in 5.6. Following the construction of the frame, a mold of the wing shape will be used to vacuum-form the skin out of ABS plastic for the root section, while carbon fiber pre-preg layup schedule will be utilized to create the composite skin for the wingtip. Durable pads damped with springs are then fastened to the wingtips to soften the landing of the vehicle.

4.2.4 Fuel & Batteries

The battery and fuel placement were some of the final elements of the structural design that were finalized due to tight space constraints within the fuselage and the flexible nature of placement for both of these items. Further, with the theoretical

center of gravity laid out by stability and control objectives, the batteries and fuel were among the most versatile elements to be placed to shift weight balance forward or backwards on the fuselage. The batteries are to be mounted above the payload bay, as shown in Figure ???. Additional empirical analysis may result in practical concerns requiring the battery packs for the three EDFs to be separated due to overheating; however, there is excess space within the fuselage to allow for adjustments to be made during a physical prototyping process. The Li-Po cells can fit within the wings, tail, and nose section of the vehicle, though considerations must be made regarding the effect of this placement on balance.

The final design was able to store 3.3 gallons of fuel in a tank made of high-density polyethylene (HDPE) plastic. The tank, shown installed in Figure 4.19, and independently in 4.21 was able to be placed directly below the wings to avoid significant shifting of the CG during fuel consumption. Further, baffles were added to the inside of the tank to minimize the sloshing of fuel during flight.

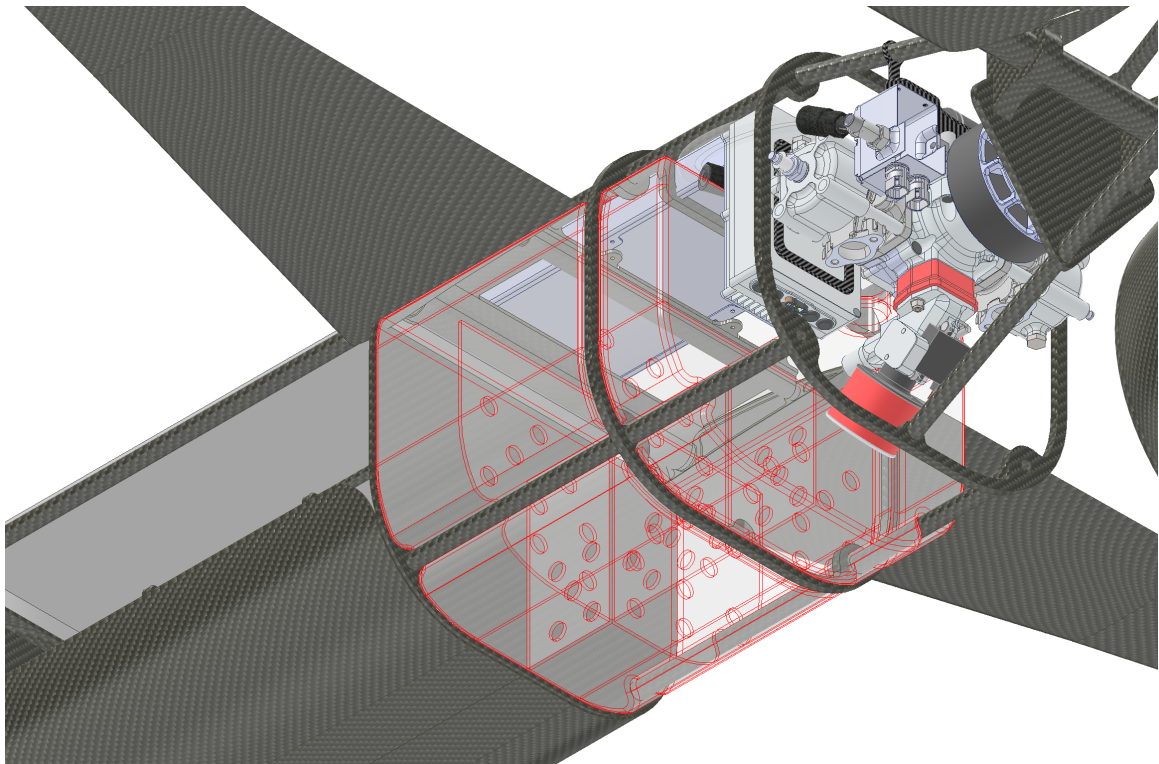


Figure 4.19: Integrated Fuel Tank.

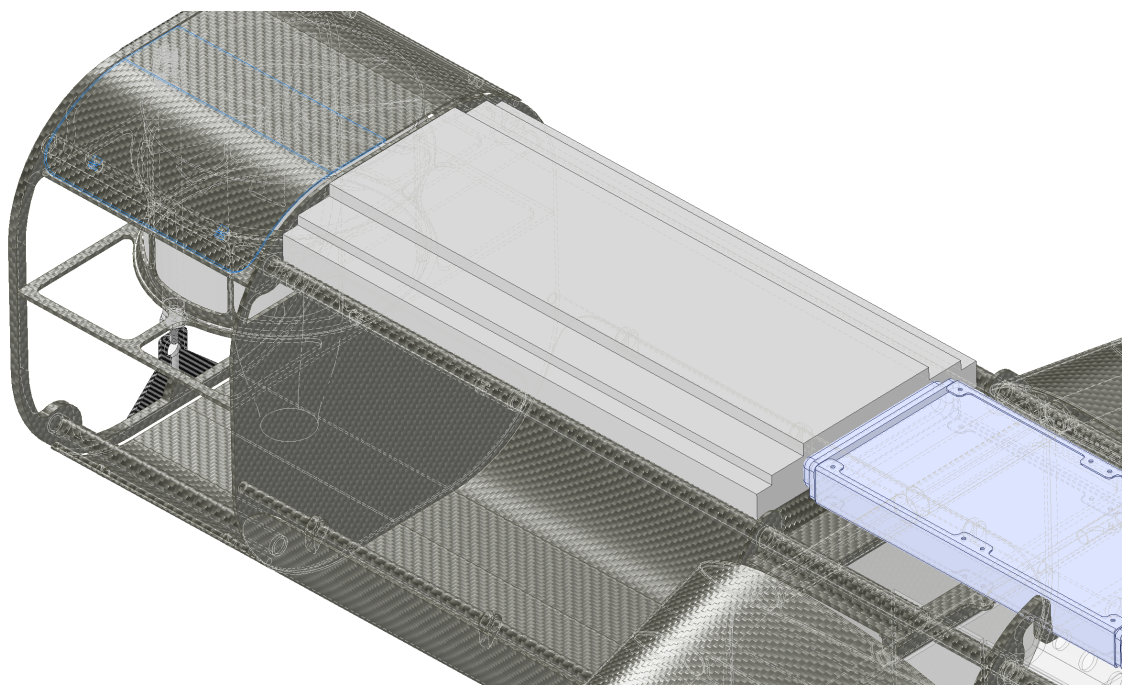


Figure 4.20: Battery storage area.

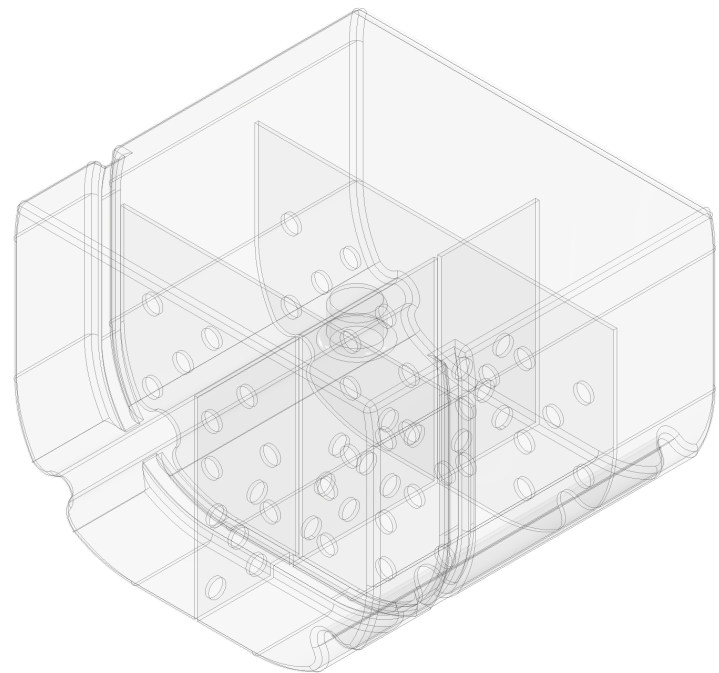


Figure 4.21: Fuel Tank

4.3 Guidance, Navigation, and Control

4.3.1 VTOL

Nonlinear Rigid-Body Equations of Motion

Throughout the GNC section, the NED axes convention is assumed to define signs of vectors. Thrusts are defined as positive.

The general rigid body equations of motion are written here, for a standard aircraft where $I_{xz} \neq 0$, $I_{yz} = 0$, and $I_{xy} = 0$, and assuming the angular momentum of the rotors is negligible. See [14].

$$\dot{x}_I = (c(\theta)c(\psi))u + (-c(\theta)s(\psi) + s(\phi)s(\theta)c(\psi))v + (s(\phi)s(\psi) + c(\phi)s(\theta)c(\psi))w$$

$$\dot{y}_I = (c(\theta)s(\psi))u + (c(\phi)c(\psi) + s(\phi)s(\theta)s(\psi))v + (-s(\phi)c(\psi) + c(\phi)s(\theta)s(\psi))w$$

$$\dot{z}_I = (-s(\theta))u + (s(\phi)c(\theta))v + (c(\phi)c(\theta))w$$

$$\dot{\phi} = p + (qs(\phi) + rc(\phi))t(\theta)$$

$$\dot{\theta} = qc(\phi) - rs(\phi)$$

$$\dot{\psi} = (qs(\phi) + rc(\phi))\sec(\theta)$$

$$\dot{u} = \frac{X_B}{m} - gs(\theta) + rv - qw$$

$$\dot{v} = \frac{Y_B}{m} + gs(\phi)c(\theta) - ru + pw$$

$$\dot{w} = \frac{Z_B}{m} + gc(\phi)c(\theta) + qu - pv$$

$$\dot{p} = \frac{I_{zz}L + I_{xz}N - \{I_{xz}(I_{yy} - I_{xx} - I_{zz})p + (I_{xz}^2 + I_{zz}(I_{zz} - I_{yy}))r\}q}{I_{xx}I_{zz} - I_{xz}^2}$$

$$\dot{q} = \frac{M - (I_{xx} - I_{zz})pr - I_{xz}(p^2 - r^2)}{I_{yy}}$$

$$\dot{r} = \frac{I_{xz}L + I_{xx}N - \{I_{xz}(I_{yy} - I_{xx} - I_{zz})r + (I_{xz}^2 + I_{xx}(I_{xx} - I_{yy}))p\}q}{I_{xx}I_{zz} - I_{xz}^2}$$

Now the external forces and torques on the rigid body will be defined. Since the only nominally nonzero component of velocity is along the body and NED z-axis, the only component of aerodynamic drag is in the z-direction. Also due to asymmetry about

the body and NED YZ plane, the only component of aerodynamic torque is in the y-direction.

$$X_B = 0$$

$$Y_B = T_1 \sin(\epsilon)$$

$$Z_B = \sum_i T_i + \frac{1}{2} C_D \rho A_{proj} w^2$$

$$L = \sum_i T_i l_{y_i}$$

$$M = \sum_i T_i l_{x_i}$$

$$N = T_1 \sin(\epsilon) l_{x_1} + \sum_i (-1)^{i+1} b \omega_i^2$$

Here, ϵ is the thrust deflection angle of the front EDF. The term $\sum_i (-1)^{i+1} b \omega_i^2$ is the reaction yawing torque from the propellers, ω_i is the angular speed of propeller i , see [11]. These equations define the nonlinear equations of motion on the aircraft. After developing the controller, it will be tested on the nonlinear system for validation.

Reduction to Linear Time-Invariant System

In order to develop a controller, the nonlinear time-varying system will be approximated as a linear time-invariant system. The linear time-invariant system will be put into the state-space form:

$$\dot{x} = Ax + Bu$$

$$y = Cx + Du$$

$$x = \begin{bmatrix} x \\ y \\ z \\ \dot{u} \\ \dot{v} \\ \dot{w} \\ \psi \\ \phi \\ \theta \\ \dot{\psi} \\ \dot{\phi} \\ \dot{\theta} \end{bmatrix} \quad u = \begin{bmatrix} T_1 \\ T_2 \\ T_3 \\ \epsilon \end{bmatrix}$$

It is beneficial to shift to earth inertial coordinate system from body coordinates for velocity. The transformation through the Tait-Bryan angles is:

$$\vec{r}_I = H_B^I \vec{r}_b$$

$$H_B^I = \begin{bmatrix} c(\theta)c(\psi) & -c(\phi)s(\psi) + s(\phi)s(\theta)c(\psi) & s(\phi)s(\psi) + c(\phi)s(\theta)c(\psi) \\ c(\theta)s(\psi) & c(\phi)c(\psi) + s(\phi)s(\theta)s(\psi) & -s(\phi)c(\psi) + c(\phi)s(\theta)s(\psi) \\ -s(\theta) & s(\phi)c(\theta) & c(\phi)c(\theta) \end{bmatrix}$$

To resolve the forces in the earth inertial coordinate system, rotate the body vector of forces by this rotation matrix:

$$\begin{bmatrix} X_I \\ Y_I \\ Z_I \end{bmatrix} = H_B^I \begin{bmatrix} X_B \\ Y_B \\ Z_B \end{bmatrix}$$

$$= H_B^I \begin{bmatrix} 0 \\ T_1 \sin(\epsilon) \\ \sum_i T_i + \frac{1}{2} C_D \rho A_{proj} w^2 \end{bmatrix}$$

Since the VTOL flight is non-rotating, the following approximations can be made:

$$\ddot{\psi} = \dot{r}$$

$$\ddot{\theta} = \dot{q}$$

$$\ddot{\phi} = \dot{p}$$

The flight is linearized about hover, such that all angles and angular rates are considered small and components of velocity are small. A further assumption is made that $I_{xz} = 0$ for mathematical simplicity. Removing state and control variable nonlinearities, the equations of motion become:

$$\dot{x}_I = \dot{x}_I$$

$$\dot{y}_I = \dot{y}_I$$

$$\dot{z}_I = \dot{z}_I$$

$$\ddot{x}_I = \frac{\sum_i T_i}{m} \theta$$

$$\ddot{y}_I = -\frac{\sum_i T_i}{m} \phi$$

$$\ddot{z}_I = \frac{\sum_i T_i}{m}$$

$$\dot{\psi} = \dot{\psi}$$

$$\dot{\phi} = \dot{\phi}$$

$$\dot{\theta} = \dot{\theta}$$

$$\ddot{\psi} = \frac{T_1 \epsilon l_{x_1}}{I_{zz}}$$

$$\dot{\phi} = \frac{\sum_i T_i l_{y_i}}{I_{xx}}$$

$$\ddot{\theta} = \frac{\sum_i T_i l_{x_i}}{I_{yy}}$$

Three nonlinearities remain in the equations for \ddot{x}_I , \ddot{y}_I , $\ddot{\psi}$. The nonlinearities in the equations for \ddot{x}_I and \ddot{y}_I can be alleviated by assuming that nominal thrust is $T_{total} = -mg$ during hover. The nonlinearity in $\ddot{\psi}$ can be alleviated by assuming that the nominal thrust during hover is $T_1 = T_{1,max}$. Therefore, the new equations become:

$$\ddot{x}_I = -g\theta$$

$$\ddot{y}_I = g\phi$$

$$\ddot{\psi} = \frac{T_{1,max}\epsilon l_{x_1}}{I_{zz}}$$

Now the state matrices are defined:

$$A = \begin{bmatrix} 0 & 0 & 0 & 1 & 0 & 0 & 0 & 0 & 0 & 0 & 0 & 0 \\ 0 & 0 & 0 & 0 & 1 & 0 & 0 & 0 & 0 & 0 & 0 & 0 \\ 0 & 0 & 0 & 0 & 0 & 0 & 1 & 0 & 0 & 0 & 0 & 0 \\ 0 & 0 & 0 & 0 & 0 & 0 & 0 & 0 & 0 & -g & 0 & 0 \\ 0 & 0 & 0 & 0 & 0 & 0 & 0 & 0 & 0 & g & 0 & 0 \\ 0 & 0 & 0 & 0 & 0 & 0 & 0 & 0 & 0 & 0 & 0 & 0 \\ 0 & 0 & 0 & 0 & 0 & 0 & 0 & 0 & 0 & 0 & 0 & 0 \\ 0 & 0 & 0 & 0 & 0 & 0 & 0 & 0 & 0 & 0 & 0 & 0 \\ 0 & 0 & 0 & 0 & 0 & 0 & 0 & 0 & 0 & 0 & 1 & 0 \\ 0 & 0 & 0 & 0 & 0 & 0 & 0 & 0 & 0 & 0 & 0 & 1 \\ 0 & 0 & 0 & 0 & 0 & 0 & 0 & 0 & 0 & 0 & 0 & 0 \\ 0 & 0 & 0 & 0 & 0 & 0 & 0 & 0 & 0 & 0 & 0 & 0 \\ 0 & 0 & 0 & 0 & 0 & 0 & 0 & 0 & 0 & 0 & 0 & 0 \end{bmatrix} \quad B = \begin{bmatrix} 0 & 0 & 0 & 0 \\ 0 & 0 & 0 & 0 \\ 0 & 0 & 0 & 0 \\ 0 & 0 & 0 & 0 \\ \frac{-1}{m} & \frac{-1}{m} & \frac{-1}{m} & 0 \\ 0 & 0 & 0 & 0 \\ 0 & 0 & 0 & 0 \\ 0 & 0 & 0 & 0 \\ 0 & 0 & 0 & 0 \\ 0 & 0 & 0 & \frac{T_{1,max}l_{x_1}}{I_{zz}} \\ 0 & \frac{l_{y_2}}{I_{xx}} & \frac{-l_{y_3}}{I_{xx}} & 0 \\ \frac{l_{x_1}}{I_{yy}} & \frac{-l_{x_2}}{I_{yy}} & \frac{-l_{x_3}}{I_{yy}} & 0 \end{bmatrix}$$

$$C = I_{12} \quad D = 0_{12,4}$$

For the aircraft designed in this thesis, the parameters are listen in Table 4.1.

Table 4.1: Linear Plant Parameters

I_{xx}	2.99 slugft 2
I_{yy}	4.34 slugft 2
I_{zz}	1.79 slugft 2
m	3.72 slug
$T_{1,max}$	33 lbs
l_{x_1}	2.2 ft
l_{x_2}	0.69 ft
l_{x_3}	0.5 ft

Controller Development

The controller must be able to track a z-velocity reference. This can be achieved with state feedback:

$$u = K(r - x)$$

K is determined with the LQR method, using the cost function:

$$J = \int_0^{\infty} (x^T Q x + u^T R u) dt$$

A method to choose the LQR gains follows Bryson's Rule, as shown in [4].

$$Q_{ii} = \frac{1}{\text{maximum acceptable value of } x_i^2}$$

$$R_{ii} = \frac{1}{\text{maximum acceptable value of } u_j^2}$$

Table 4.2 displays the chosen maximum accepted values of each state and control variable during ascent.

Table 4.2: Maximum Acceptable Values of State and Control Variables, Ascent

x_I	1 ft
y_I	1 ft
z_I	∞ ft
\dot{x}_I	1 $\frac{ft}{s}$
\dot{y}_I	1 $\frac{ft}{s}$
\dot{z}_I	0.1 $\frac{ft}{s}$
ψ	0.1
ϕ	0.1
θ	0.1
$\dot{\psi}$	1.5 $\frac{1}{s}$
$\dot{\phi}$	1.5 $\frac{1}{s}$
$\dot{\theta}$	1.5 $\frac{1}{s}$
T_1	33 lbs.
T_1	56 lbs.
T_1	56 lbs.
ϵ	0.5

After solving the Algebraic Riccati Equation in MATLAB, the optimal feedback

gain matrix is found.

$$K = \begin{bmatrix} -30.1 & -2.5 & 0 & -42.0 & 0 & -135 & 0 & 0 & 454 & 0 & 0 & 44.1 \\ 16.2 & 39.6 & 0 & 22.5 & 55.7 & -361 & 0 & 621 & -242 & 0 & 66.5 & -23.0 \\ 16.2 & -39.6 & 0 & 22.5 & -55.7 & -361 & 0 & -621 & -242 & 0 & -66.5 & -23.0 \\ 0 & 0 & 0 & 0 & 0 & 0 & 5.0 & 0 & 0 & 0.62 & 0 & 0 \end{bmatrix}$$

This controller will be analyzed on the linear and nonlinear systems in Chapter 5.

4.3.2 Aerodynamic Coefficients and Simulation

From the early stages of the design, the mass-balance of the aircraft was considered at a high level for the two required modes of flight: VTOL and fixed-wing cruise. As discussed in the previous sections, for VTOL, a center of gravity (CG) towards the aft of the vehicle was desired to allow for pitch control during ascent without the need for an overpowered front rotor which would not be used during cruising flight. Unfortunately, in order to maintain aerodynamic stability during fixed-wing flight, a CG forward of the neutral point of the aircraft was desired to maintain a positive static margin.

6DOF - Simulation Development

In order to develop a robust simulation environment for testing control laws, aircraft stability, and simulating transitional flight, a model needed to be developed to account for nonlinearities in the vehicle's equations of motions and accurately represent the aerodynamic characteristics at a variety of flight conditions. The software OpenVSP was chosen due to its versatility in aircraft modeling as a preliminary design tool.

Due to inconsistencies in the results of VSP Aero's stability analysis in the body-frame, the wind-axis coordinate system was used for simulations, and was subsequently transformed into body axis coordinates for use in the 6-DOF equations of motion. The 6 degrees of freedom required for flight simulation in the wind-axis are the three primary orthogonal force directions, Lift (F_L), Drag (F_D), and Side-Force (F_S), and the three moments along those axes: Rolling Moment (M_R), Pitching Moment (M_P), and Yawing Moment (M_Y). With these quantities known, given the mass properties and inertial matrix of the vehicle, along with starting conditions for the full state of 3 lateral and 3 rotational velocities, the exact motion of the vehicle can be simulated.

$$\begin{aligned}\dot{u} + qw - rv + g\sin(\theta) &= \frac{F_X}{m} \\ \dot{v} - pw + ur + g\cos(\theta)\sin(\phi) &= \frac{F_Y}{m} \\ \dot{w} + pv - qu + g\cos(\theta)\sin(\phi) &= \frac{F_Z}{m}\end{aligned}$$

Each aerodynamic coefficient is highly dependent on the vehicle's state, and is influenced by the angle of attack, side-slip, Mach number, altitude, and control deflections. In order to approximate vehicle motion, the forces and moments are non-dimensionalized by $\frac{1}{2}\rho v^2 S_{ref}$ and $\frac{1}{2}\rho v^2 S_{ref} \bar{c}$, respectively. Using these, the vehicle motion at each time step can be derived by calculating $F_i = \frac{1}{2}\rho v^2 S_{ref} C_{Fi}$ and $M_i = \frac{1}{2}\rho v^2 S_{ref} \bar{c} C_{Mi}$ for each orthogonal axis if the 6 primary coefficients are known. The following simplifications were made to capture the influence of the state on the coefficients, and these were then implemented in Simulink and MATLAB using aerodynamic tables constructed from OpenVSP simulations, computed across a range of α 's from -10 to 20 degrees. Figures 4.22 and 4.23 show a sample run of flight conditions for varying alpha at the fixed cruising altitude around 1000ft, and the overall 6DOF simulation in MATLAB, respectively. The simulation was only able to be debugged to reliably demonstrate flight in longitudinal dynamics using the VSP outputs. The use of lookup tables as a function of α is shown in 4.24 for the 3DOF longitudinal simulation.

$$L = Q \cdot S_{ref} \cdot C_l(\alpha, \beta, M, h, \delta_e, \delta_a, \delta_r)$$

$$\begin{aligned}C_l &= C_{l0} + \frac{\partial C_l}{\partial \alpha} \alpha + \frac{\partial C_l}{\partial \delta_e} \delta_e + \frac{\partial C_l}{\partial q} q \\ C_d &= C_{d0} + \frac{\partial C_d}{\partial \alpha} \alpha + \frac{\partial C_d}{\partial \delta_e} \delta_e + \frac{\partial C_d}{\partial q} q \\ C_s &= C_{s0} + \frac{\partial C_s}{\partial \beta} \beta + \frac{\partial C_s}{\partial \delta_r} \delta_r\end{aligned}$$

$$C_{Mx} = C_{Mx0} + \frac{\partial C_{Mx}}{\partial \alpha} \alpha + \frac{\partial C_{Mx}}{\partial \beta} \beta + \frac{\partial C_{Mx}}{\partial r} r + \frac{\partial C_{Mx}}{\partial p} p + \frac{\partial C_{Mx}}{\partial \delta_r} \delta_r + \frac{\partial C_{Mx}}{\partial \delta_a} \delta_a$$

$$C_{My} = C_{My0} + \frac{\partial C_{My}}{\partial \alpha} \alpha + \frac{\partial C_{My}}{\partial \delta_e} \delta_e + \frac{\partial C_{My}}{\partial q} q$$

$$C_{Mz} = C_{Mz0} + \frac{\partial C_{Mz}}{\partial \beta} \beta + \frac{\partial C_{Mz}}{\partial r} r + \frac{\partial C_{Mz}}{\partial p} p + \frac{\partial C_{Mz}}{\partial \delta_r} \delta_r + \frac{\partial C_{Mz}}{\partial \delta_a} \delta_a$$

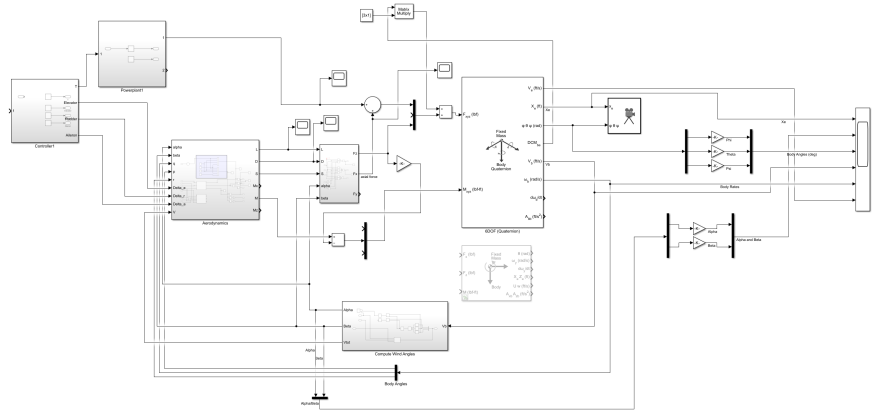


Figure 4.22: 6 DOF Aerodynamic Simulation in MATLAB and Simulink

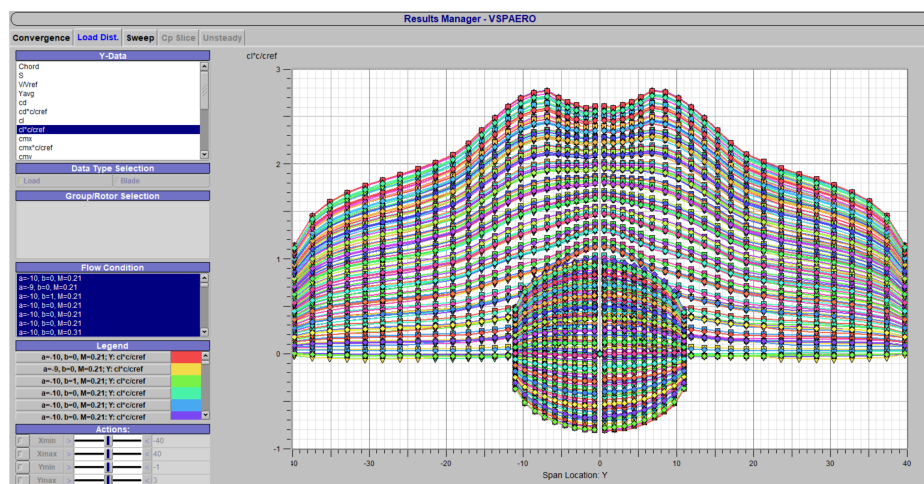


Figure 4.23: Sample VSP Run for Populating Aero Database

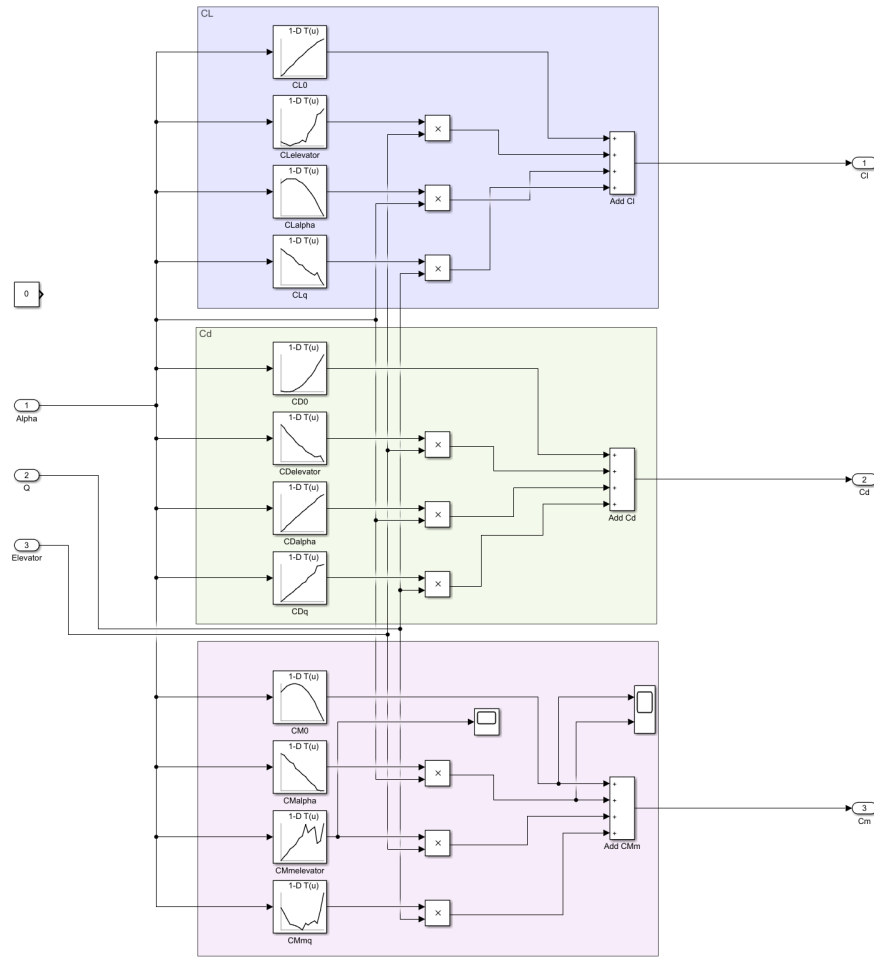


Figure 4.24: 3 DOF Aerodynamic Database Developed for Modeling and Simulation

Chapter 5

Analysis and Simulation

5.1 Structures and Airframe

5.1.1 Fuselage Skeleton

FEA simulations were run iteratively throughout the design process to determine robustness against yield (static failures) and buckling, which was initially a concern due to the use of long narrow rods to construct the frame. Loading conditions and constraints for this analysis were primarily derived from the mounting points of critical load-bearing elements: the EDF mounts (front and rear), wing mounts, and generator mounts.

As discussed in Chapter 4.2, two classes of EDFs were used in this vehicle, with one performing a control function for pitch-axis balance in VTOL, and the other two serving as dual-purpose tilt rotors for both cruising propulsion and VTOL flight. Loads on the front frame were assessed by isolating the front portion of the vehicle, just aft of the payload bay, applying a 6DOF Fixed constraint to the cross section of the 4 longitudinal rods, and applying a bearing load to the mount in the vertical direction equal to 2x the expected maximum thrust of the front motor. Results of this isolated analysis, (static and buckling) are shown in Figures ?? and 5.3. As seen, even under conservative loading conditions, the frame is anticipated to withstand both stresses and resist deformation to avoid buckling of the non-load-bearing skin.

This bearing was subjected to the full combined thrust of the larger 195mm fans at full power (112 lbf, rounded to 120lbf for some margin in simulation.) As shown in the full analysis of the frame with these forces, Figures 5.1 and 5.2 the frame is

anticipated to resist both buckling and static failure during anticipated during VTOL and flight.

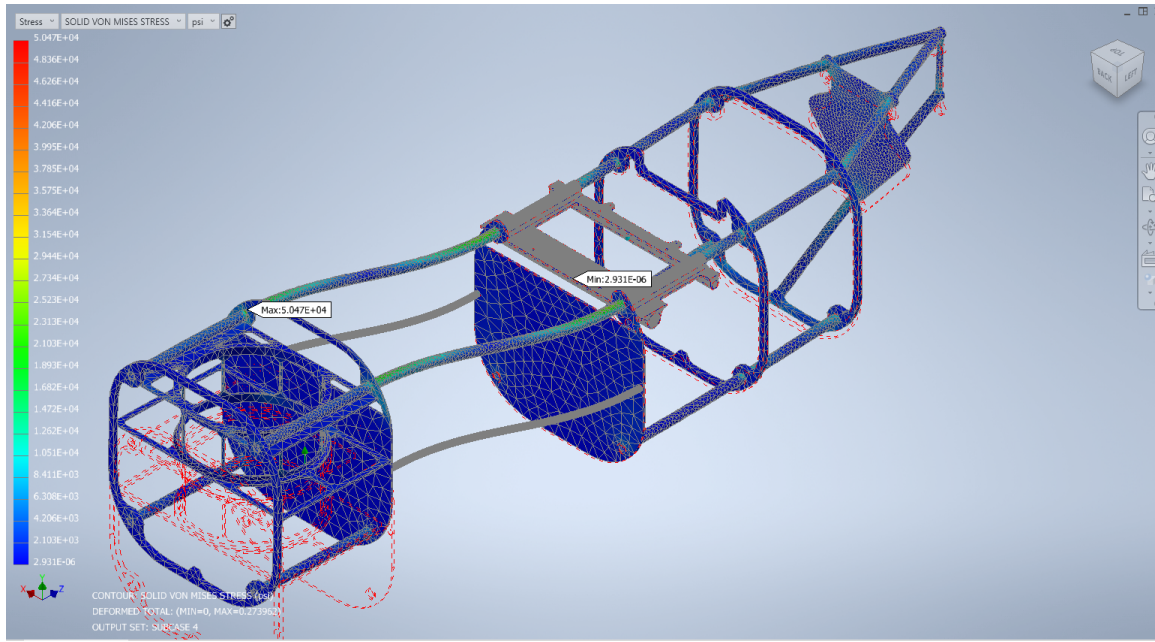


Figure 5.1: Final Frame Static Stress Analysis

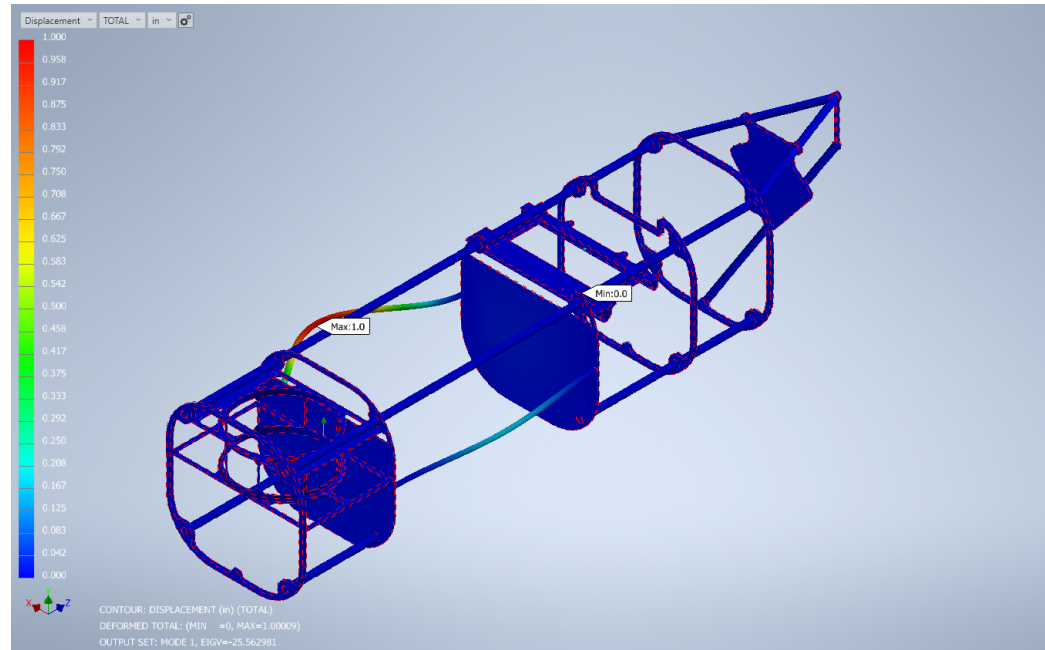


Figure 5.2: Final Frame Buckling Analysis (Only 1 significant mode)

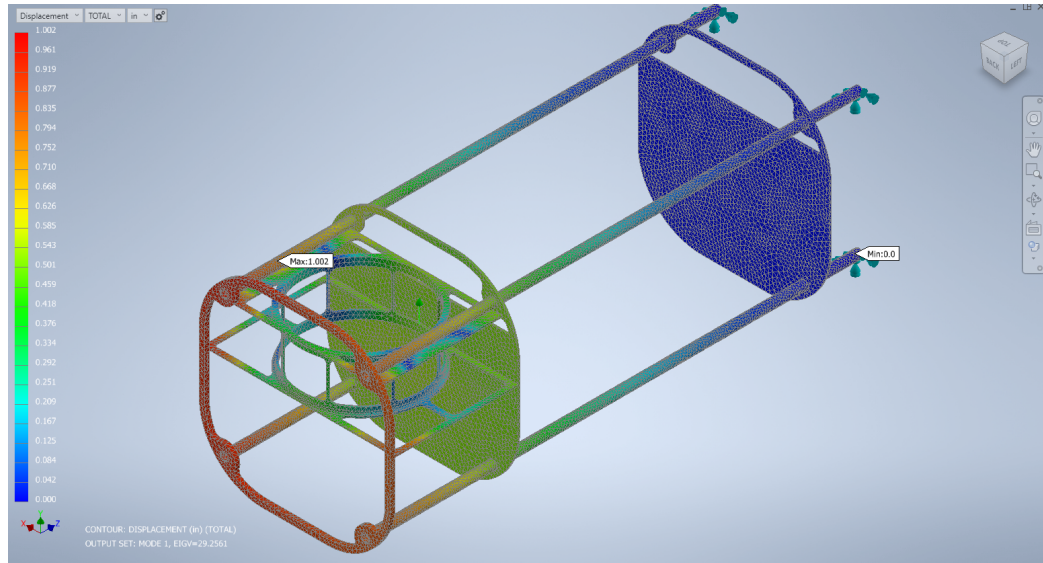


Figure 5.3: Figure : Linear Buckling Analysis (Mode 1; eig = 29.5)

5.1.2 Wings

As discussed in 4.2, the wings are secured to a component manufactured from CFRP plates and tubes that is fastened to the main longitudinal rails of the vehicle. A simple linear static and buckling analysis of this component under anticipated loads of straight-and-level flight demonstrates sufficient robustness against aerodynamic loading as shown in Figures 5.4 and 5.5

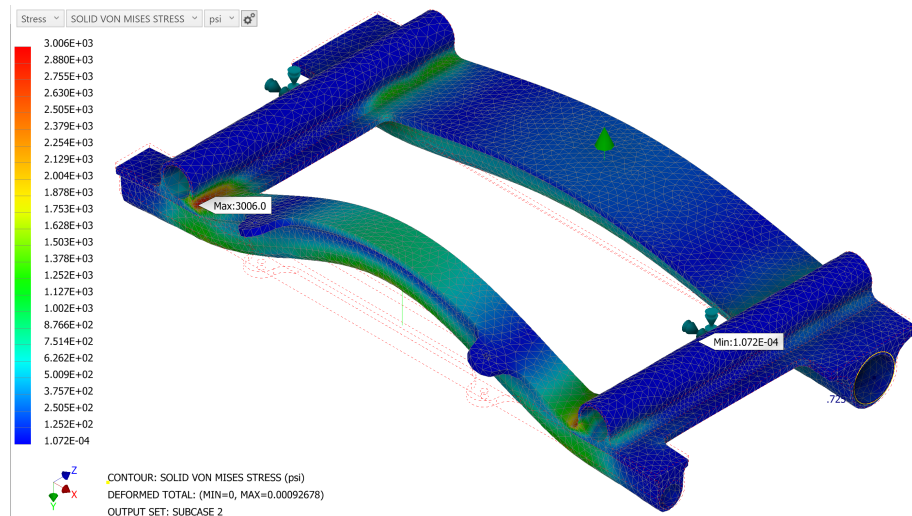


Figure 5.4: Wing-Mount Static Analysis (140 lbs)

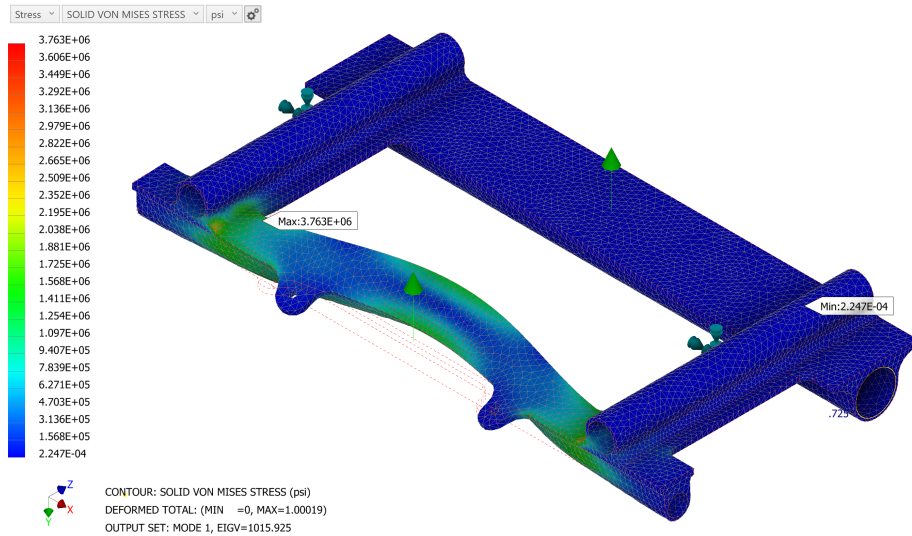


Figure 5.5: Wing-Mount Buckling: Mode 1 Eigenvalue = 1015.93, 140 lbs

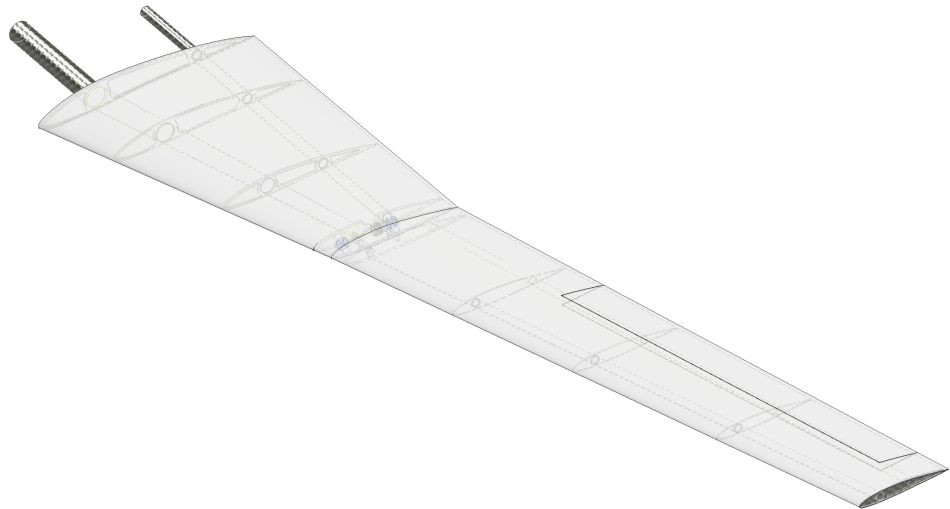


Figure 5.6: Full Wing Assembled

Early iterations of the wings suffered from severe buckling, as shown in Figure 5.7, leading to the decision to use a second spar, in addition to a carbon fiber skin for the wingtip, as it was responsible for bearing the bulk of the axial load from landing and impact forces, requiring significant reinforcement to even support the weight of the craft. The later iteration of the wing with CFRP skin is shown resisting buckling with a BLF of in Figure 5.8. The third landing gear is responsible for supporting the

front end of the vehicle and is extended through the UAV's pneumatic circulatory system.

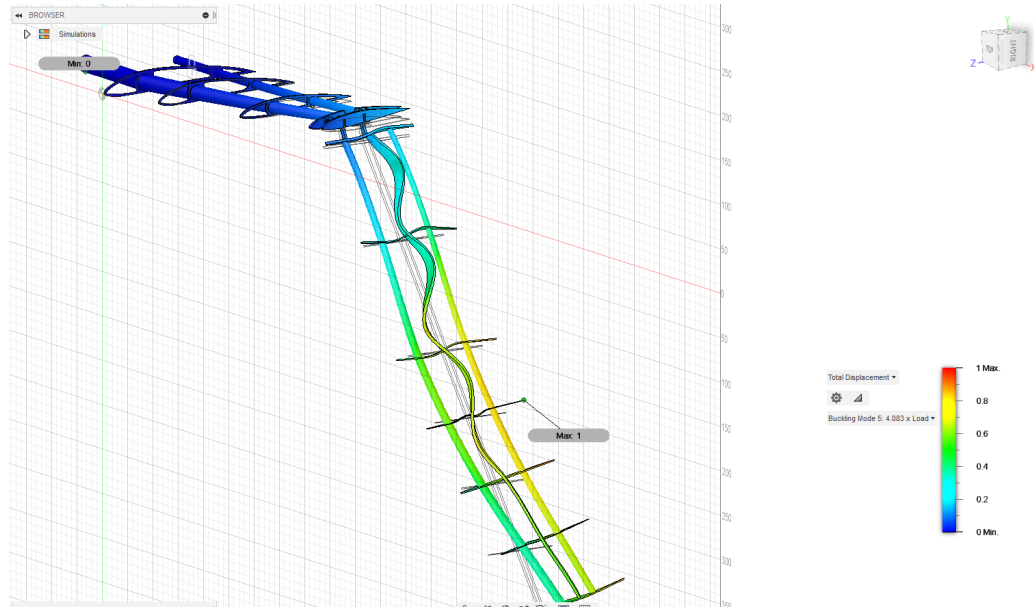


Figure 5.7: Frame-Only Wing Buckling



Figure 5.8: Wing Buckling with Skin, 60 lbf load. BLF = 3.9

5.1.3 Weights & Balance

Finally, the computed point of the neutral point of the vehicle dictated that the C.G. should be approximately 37" aft of the nose for stable longitudinal flight. As shown in Figure 5.9, the C.G. lies about 36.5" aft of the vehicle nose, and can be flexibly adjusted with battery placement. This location for the CG provides a static margin of 0.27.

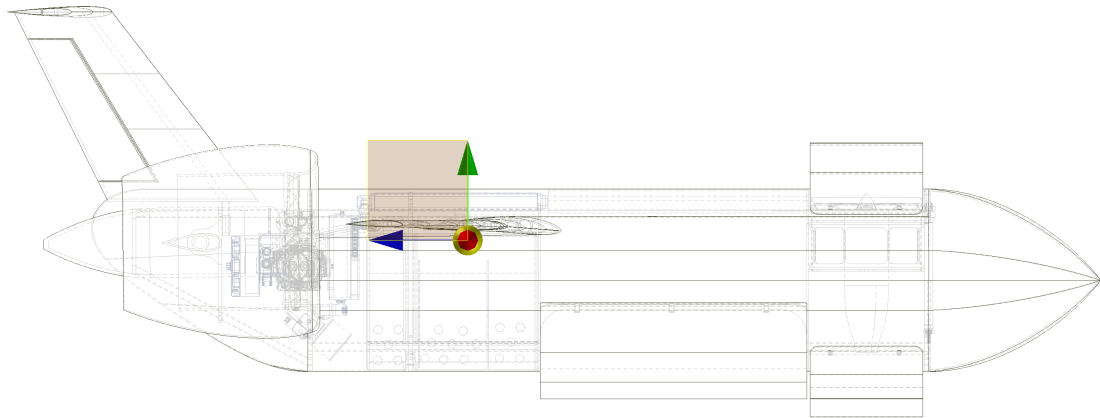


Figure 5.9: Final CG Location: 37" aft of nose

5.2 Guidance, Navigation, and Control

5.2.1 VTOL Ascent

Linear response

The linear system was modelled in Simulink and is shown in Figure 5.10.

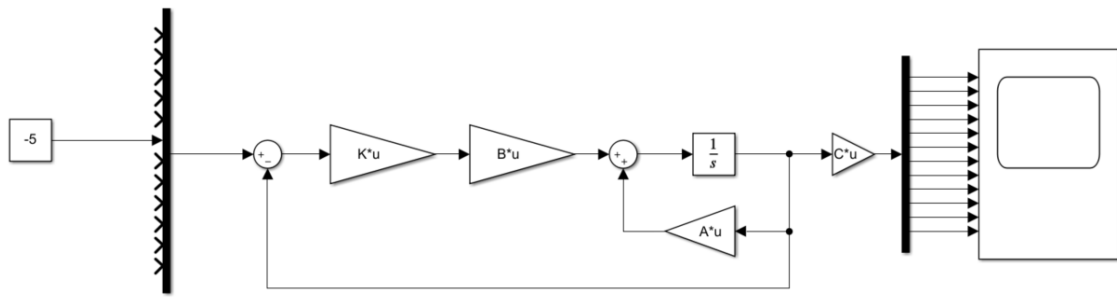


Figure 5.10: State Space Representation in Simulink

A step input of -5 ft/s z-velocity was fed into the system, which gives us the response:

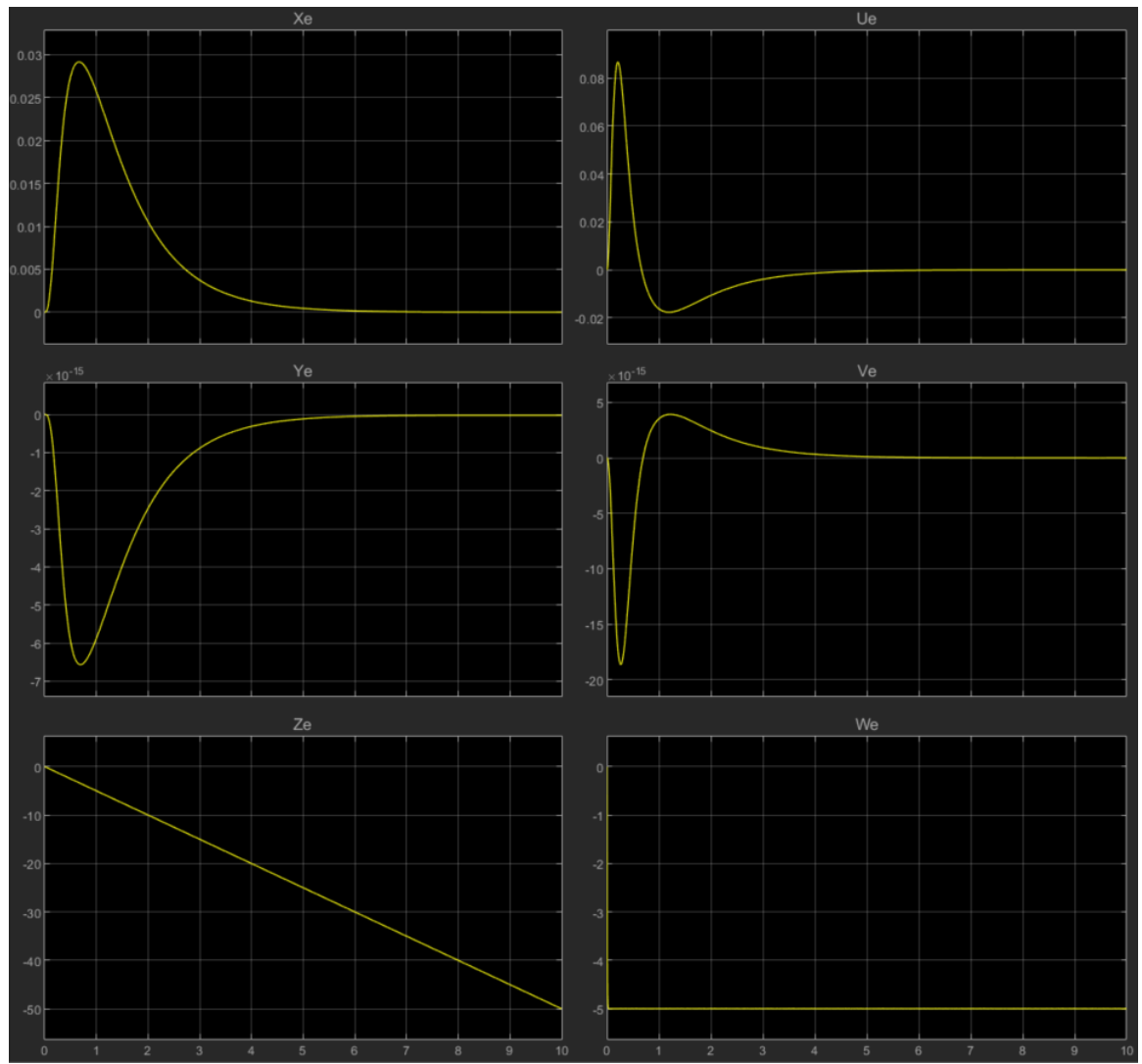


Figure 5.11: Linear response to a -5 ft/s z-velocity step input

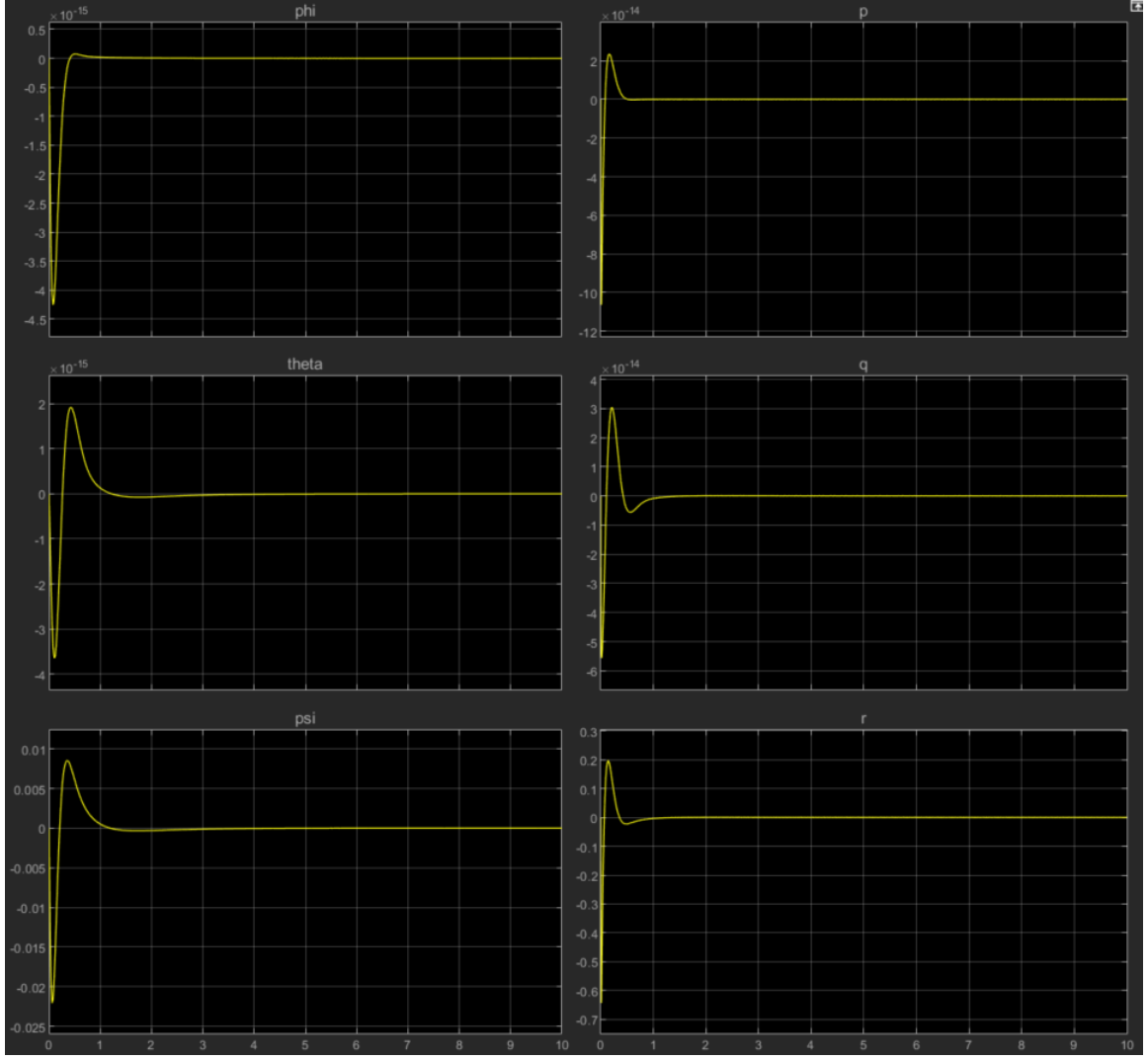


Figure 5.12: Linear response to a -5 ft/s z-velocity step input

As can be seen in Figures 5.11 and 5.12 linear response to a step input of -5 ft/s z-velocity has approximately zero steady state error in the states, including the step input. The linear response is good, but it assumes that thrust can be positive or negative, with no limit. Additionally, none of the nonlinearities in the dynamics are represented. The analysis will now turn toward controller simulation on the nonlinear, time-varying system.

In order to simulate the nonlinear rigid-body dynamics in Simulink, the 6DOF quaternion equations of motion block from the Aerospace Blockset was used. This block propagates the nonlinear equations of motion using quaternions, so gimbal lock is not a concern. The entire inertia tensor was used in the simulation, using the values pulled off the Inventor CAD model. Additionally, aerodynamic effects were added to

create a higher fidelity model. These are propeller counter torque and z-direction drag, shown in Equations. The parameters necessary to model these aerodynamic effects are listed in Table 5.1.

$$Z_B = \frac{1}{2} C_D \rho A_{proj} w^2$$

$$N = \sum_i (-1)^{i+1} b \omega_i^2$$

Table 5.1: Parameters for Nonlinear System

Parameter	Value
A_{proj}	8.8 ft^2
C_D	1
b_1	1.67e-09 $\frac{Nm}{RPM^2}$
$b_2 = b_3$	9.57e-09 $\frac{Nm}{RPM^2}$

The propeller counter torque coefficients were estimated based on values obtained in [11]. These could be better estimated through empirical testing with the chosen EDFs. With these parameters, the nonlinear model can now be created in Simulink. The layout is shown in Appendix C.

During takeoff, the z-velocity reference input should not be a step input. Takeoff should immediately be slow to avoid injuring bystanders and for object avoidance. A ramp z-velocity reference was tested on the nonlinear system with a slope of -0.5 ft/s. The plots of position and inertial velocities are shown in Figure 5.13. Body rate and Euler angle plots are in Appendix C.

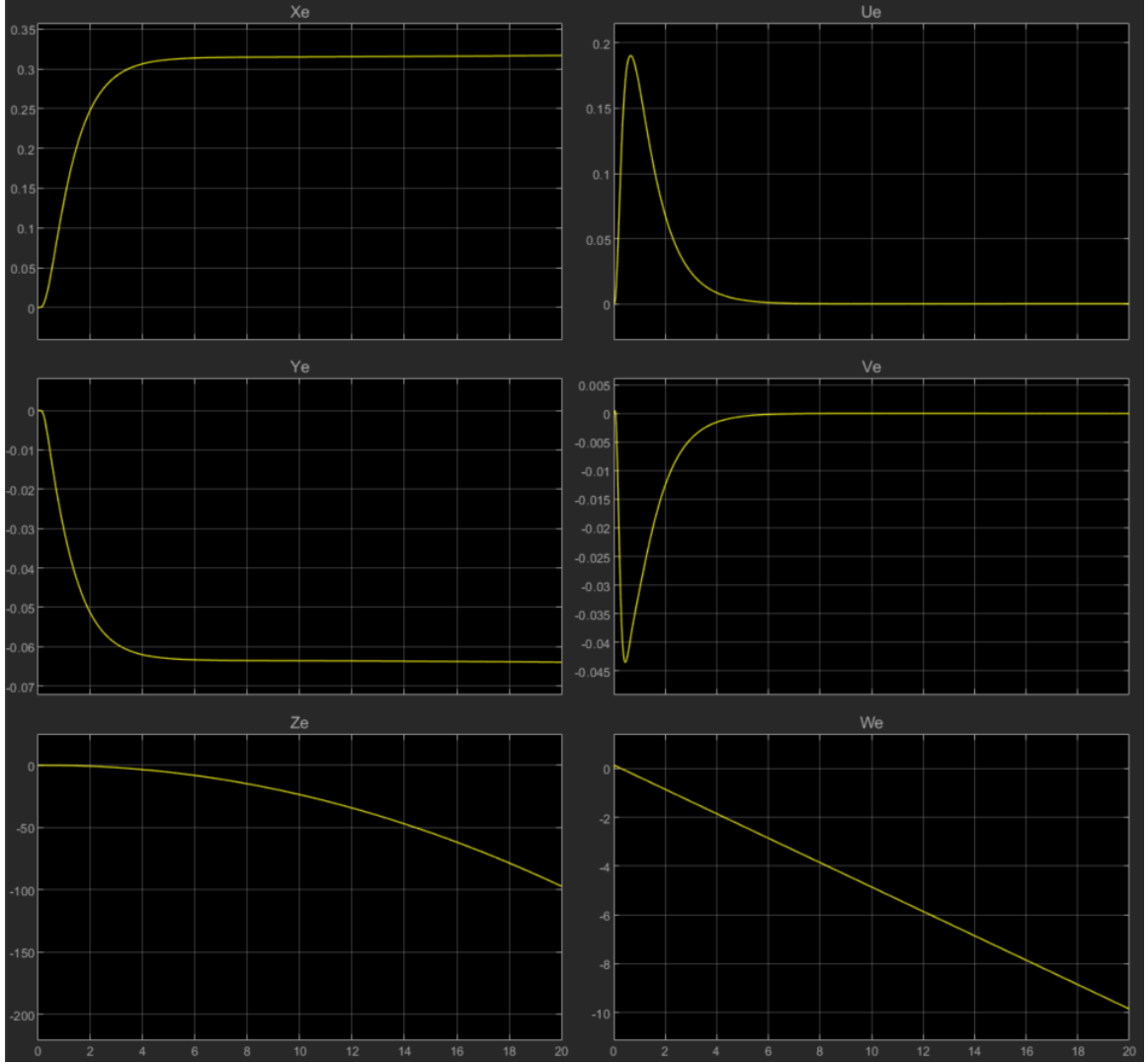


Figure 5.13: Position and velocity response to a -0.5 ft/s ramp input.

Analyzing the plots, steady state error can be observed in the plots of x_I and y_I . Inertial z-velocity tracks the -0.5 ft/s reference well but with some error. These errors could be mitigated by implementing an LQI (Linear Quadratic Integrator) controller, and is worth further investigation but outside the scope of this thesis. Examining the z-coordinate plot, it can be seen that the aircraft reaches 100 ft in 20 seconds, 10 seconds less than the 30 second budget. This could be improved further, but is dependent on the accuracy of the C_D estimate. Further research on this topic would involve flight testing to determine maximum VTOL climb rate.

An effect that was not modelled was the phase lag in the EDF thrust. This could be captured using thrust command vs. time measurements on a test stand. Modelling this effect was outside the scope of this thesis but will be the topic of

further investigation.

5.2.2 VTOL Descent

The descent problem is slightly different than the ascent problem. After cruise drops the aircraft off around 100 feet altitude, there will be some nominal error between the x_I, y_I coordinates of the aircraft and the target landing area. For the purposes of this analysis, it is assumed that at the end of cruise the translation error will be less than 100 feet. In order to control the translational position as well as the inertial z-velocity, a different controller must be derived. Again, using Bryson's rule to determine LQR gains, the maximum acceptable error values of each state and control variable are presented in Table 5.2.

Table 5.2: Maximum Acceptable Values of State and Control Variables, Descent

x_I	0.5 ft
y_I	0.5 ft
z_I	∞ ft
\dot{x}_I	$\infty \frac{ft}{s}$
\dot{y}_I	$\infty \frac{ft}{s}$
\dot{z}_I	0.1 $\frac{ft}{s}$
ψ	0.1
ϕ	0.1
θ	0.1
$\dot{\psi}$	$2 \frac{1}{s}$
$\dot{\phi}$	$2 \frac{1}{s}$
$\dot{\theta}$	$2 \frac{1}{s}$
T_1	33 lbs.
T_1	56 lbs.
T_1	56 lbs.
ϵ	0.5

After solving the Algebraic Riccati Equation in MATLAB, the optimal gain matrix is obtained.

$$K = \begin{bmatrix} -60.3 & 0 & 0 & -40.6 & 0 & -134.5 & 0 & 0 & 437 & 0 & 0 & 41.4 \\ 32.3 & 79.2 & 0 & 21.7 & 54.6 & -362 & 0 & 602 & -232 & 0 & 63.2 & -21.5 \\ 32.3 & -79.2 & 0 & 21.7 & -54.6 & -362 & 0 & -602 & -232 & 0 & -63.2 & -21.5 \\ 0 & 0 & 0 & 0 & 0 & 0 & 5.0 & 0 & 0 & 0.58 & 0 & 0 \end{bmatrix}$$

The nonlinear Simulink model used to analyze the descent controller is the same as the ascent model, except a simple guidance outer loop has been implemented. The controller is fed a ramp x-position command of 4 ft/s, saturated at the 100 ft target x-position. The z-velocity command is 3.3 ft/s, so the descent is controlled. At 10 feet altitude, the z-velocity command ramps down to 0.5 ft/s for a soft and safe landing. The descent guidance algorithm developed is shown in Figure 5.14.

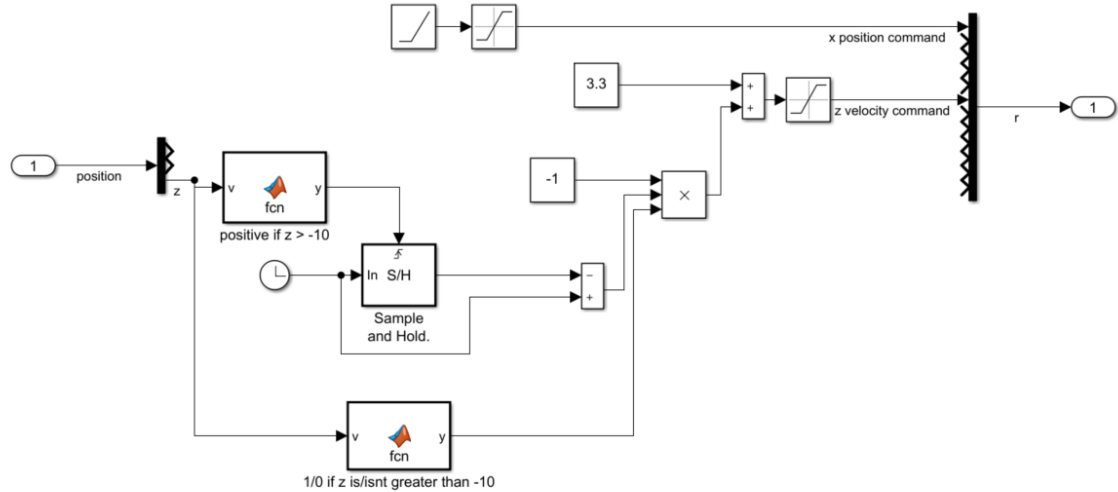


Figure 5.14: Descent Guidance Algorithm

The position and inertial velocity plots are shown in Figure 5.15. Body rate and Euler angle plots are in Appendix C.

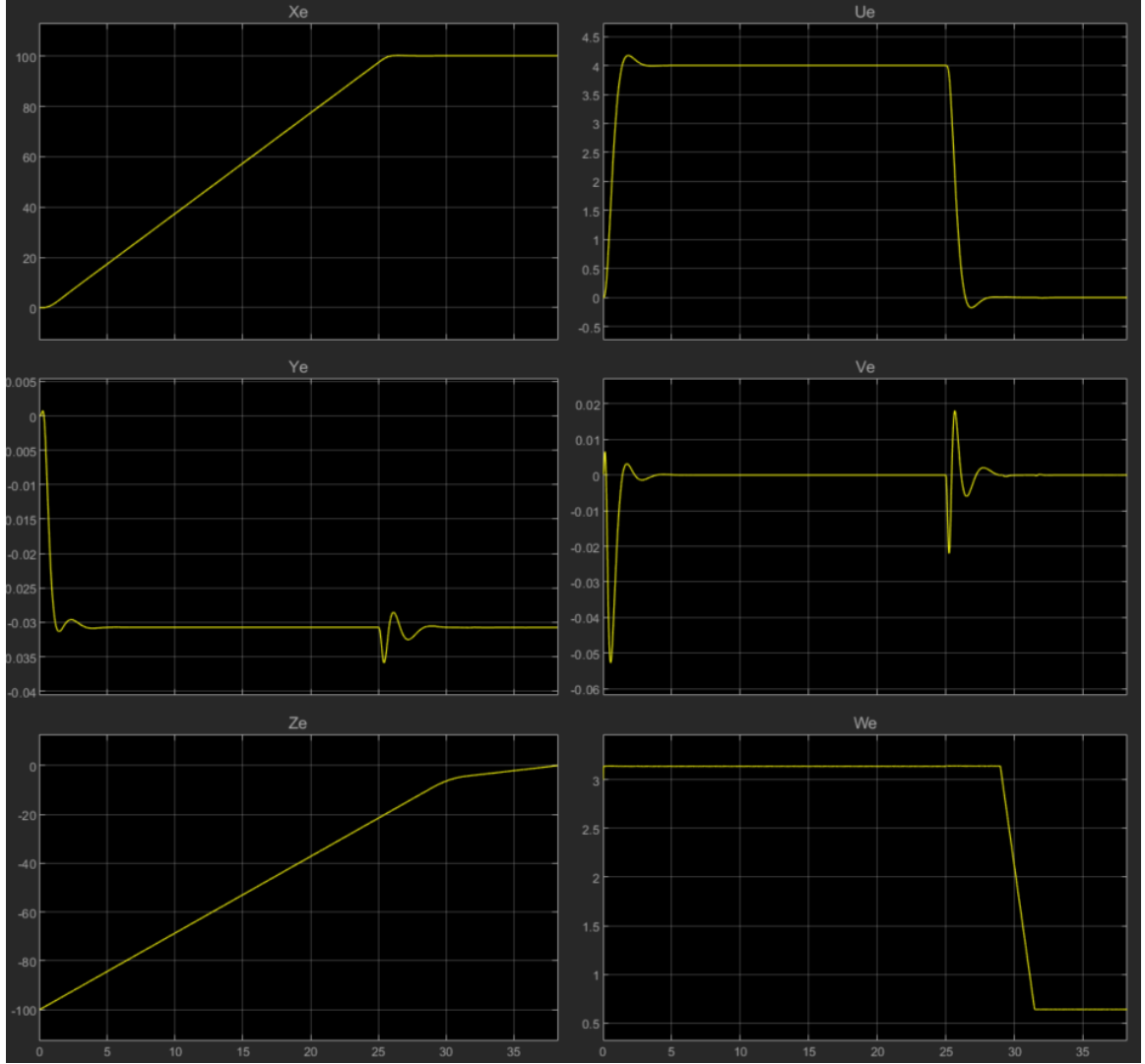


Figure 5.15: Position and velocity response to descent guidance.

As can be seen in Figure 5.15, the aircraft tracks the 4 ft/s ramp reference input until the saturation of 100 ft is reached, a value it holds until landing. On the z-velocity plot it can be seen that the controller holds the constant input of 3 ft/s with approximately 0.1 ft/s of error, until the z-coordinate reaches -10 ft, where it ramps down to 0.6 ft/s for landing. Similarly to the conclusion reached after the VTOL ascent analysis, these steady state errors could be mitigated by implementing an LQI controller.

Further work on GNC for this aircraft will involve analyzing the end-of-cruise control problem and better quantifying the translational error that results after cruise.

5.3 Updated Mass Budget

The updated mass budget is displayed in Table 5.3. This reflects the improvements made since the preliminary estimates. The structure frame of the carbon fiber aircraft is only 11.8 lbs. The detailed design of the structure outfitted the fuselage with a 3.3 gallon fuel tank, which corresponds to 29 pounds of fuel. Additionally, the battery was sized down to 15.1 lbs. after the detailed design.

Table 5.3: Final Mass Budget

Component	Mass (lbs.)
Payload	25
Structure Frame	11.8
Generator	9.7
EDFs	25.4
Battery	15.1
Fuel	27
Actuators, Compressor, Miscellaneous	6
Total	120

5.4 Updated Range

With the updated mass budget numbers, an updated range must be calculated. Solving equation 3.2.4 again for range with the updated fuel fraction of $\beta_{total} = 93/120 = 0.775$, the range is calculated to be 656 miles. (See appendix D). This greatly increases the abilities of the aircraft; the maximum survivable radius for a two-way mission becomes 328 miles.

Chapter 6

Small-Scale Prototype



Figure 6.1: Version 3 prototype.

6.1 Overview

In addition to designing, modeling, and simulating this novel UAV configuration, several small scale prototypes were created to serve as a proof of concept. The goal

was twofold:

1. To prove the viability of the design
2. To gain a greater understanding of the systems, failure points, and manufacturing techniques to aid in creating a full-scale design that can be practically implemented and manufactured by a small team or in an early stage startup setting.

The small scale prototype attempted to stay as true to the large scale design as possible given the time, resources, and tools allotted.

6.1.1 Constraints

Due to the temporary suspension of in person instruction caused by the COVID-19 pandemic, access to labs, tools, and equipment was limited. The design of the small scale prototype was constrained by readily available equipment which included:

- Hand Saw
- Electric drill
- 3D printing
- Soldering Iron
- M1-M5 nuts and bolts
- JB Weld epoxy
- Tape

6.2 Scaling Considerations

Many of the relationships that govern this aircraft do not scale down linearly. When possible, the scale model's dimensions and specifications were chosen to match the full-size vehicle. The scale factors for the prototype were first limited in range by availability of components (often dictated by RC plane and RC drone hobbyist community) as well as manufacturing and testing feasibility. From there the values were further chosen to align with the full size in terms of:

- Wingspan to body length ratio
- EDF diameter to fuselage diameter ratio
- Moment balance of (EDF thrust * Length to Cg) about the CG and CL
- Percent of total thrust contributed by each motor

Additionally, the prototype was similar to the large scale in terms of:

- Battery chemistry: Lithium Polymer 60C 4000mah cells
- Electronic Ducted Fans: DC brushless motor with 12 blades
- Location of Cg and Cl
- Flight computer hardware and software
- Tilt rotor mechanism

The key differences between the prototype and the large scale include:

- Powertrain: fully electric instead of hybrid electric
- Actuators: Digital Servos instead of pneumatic
- Yaw control: Tilted EDF instead of thrust vaning
- Payload: Portion of Max takeoff mass allocated to payload were not correlated

6.3 Hephaestus: Small Scale Prototype Version 1: [Powertrain testing rig]

After choosing viable parameters and dimensions for the scale model, the powertrain was designed. A simple low fidelity mockup was quickly created out of wood using 2x4's and wooden dowels in order to safely secure the powertrain for preliminary testing.

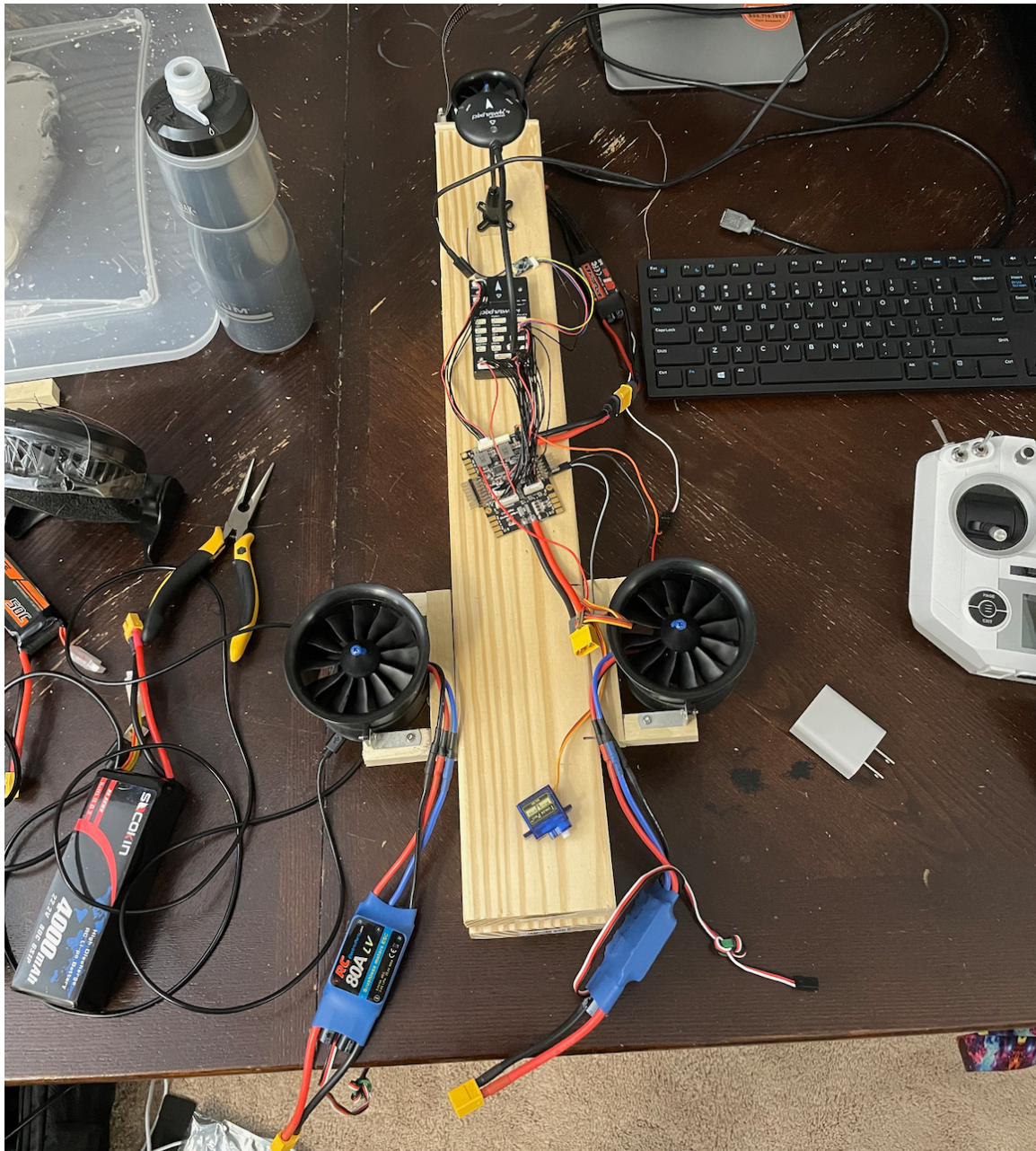


Figure 6.2: Version 1 prototype.

The propulsion system features:

- Two rear EDFs to provide thrust during VTOL and Cruise
 - 70mm diameter with 12 blades
 - 2300KV-6s DC Brushless motor
- Two 80A Electronic Speed Controllers (ESC)

- 5v 28 battery eliminating circuit (BEC)
- Two 6s LIPO batteries (ESC)
 - 4000mah 60C
- One front EDF to provide thrust during VTOL and Yaw control
 - 50mm diameter with 12 blades
 - 4900 KV-3s DC Brushless motor
- One 40A Electronic Speed Controllers (ESC)
 - 5v 28 battery eliminating circuit (BEC)
- One 3s LIPO battery (ESC)
 - 2300mah 50C

6.3.1 ESC Calibration and Motor Testing:

With the motors securely attached to testing rig, each motor was tested First, the ESC's were tested and calibrated. The ESC's use an older PWM communication protocol which has largely been replaced by faster analog protocols such as Oneshot and Multishot and the newer digital DShot protocol which offer much better performance, reduced jitter, and reduced delay

The ESC requires a PWM signal with a pulse length around 1000-2000ms. To simulate the PWM signal to the ESC, a 50HZ square wave was generated. Varying the duty cycle created a pulse length in the appropriate range. In addition to calibrating the upper and lower bounds of the ESC's, the minimum motor spin speed was measured, and the relationship between throttle input and motor thrust was recorded.

The two rear EDF's produced a maximum thrust of 2207 grams with 1640 watts of power. The front EDF produced 760 grams of thrust with 480 watts of power.

6.4 Chiron: Small Scale Prototype Version 2 [Core Systems and Hover Test]

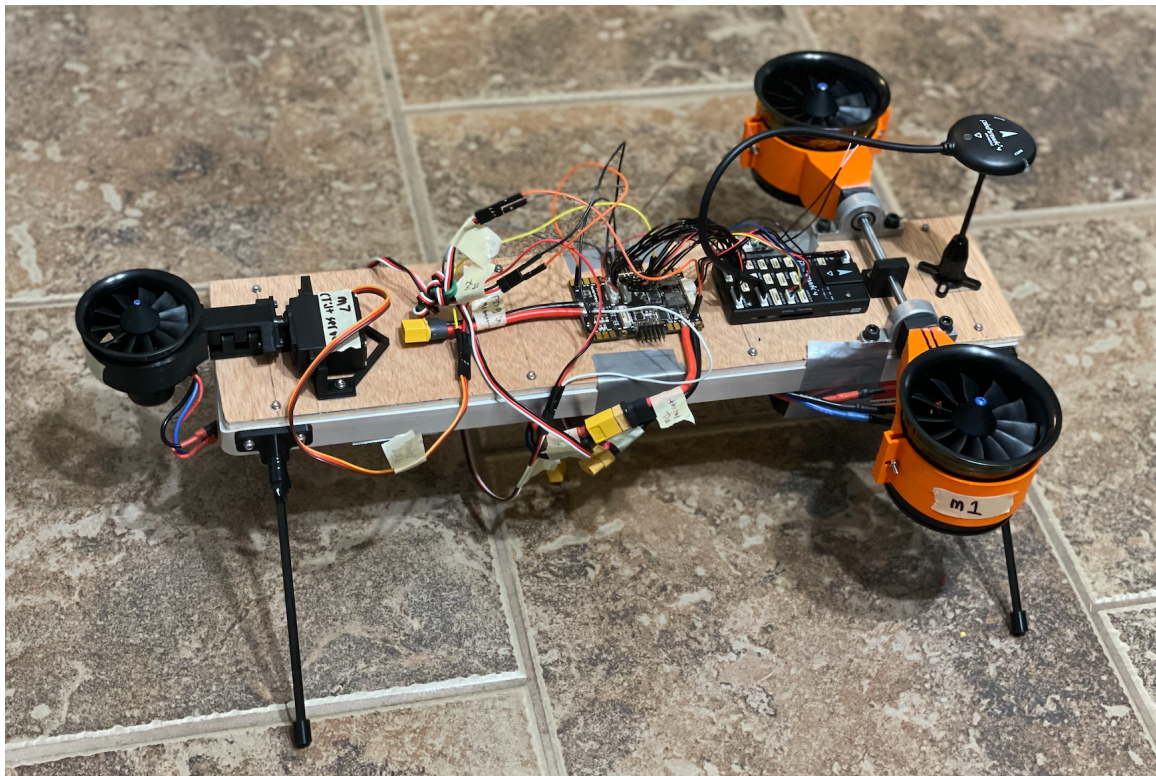


Figure 6.3: Version 2 prototype.

6.4.1 Goal

The goal of the second prototype iteration was to design the remaining core systems, as well as prove this specific tricopter configuration was stabilizable in hover (corresponding to the VTOL mode on the full scale).

The version 2 prototype was intended to be a testing platform that facilitated rapid testing, easily swappable components, and a frame which would be robust to the inevitable countless crashes as the controller gains were tuned.

6.4.2 Design considerations

Frame

The design of Chiron started with creating a lightweight, durable frame. In order to create a strong, rigid frame that could resist impacts, a rectangular skeleton was created by bending 3/4” aluminum angle using a press brake. The available alloy was AL6061 T6, which has desirable material properties but is notorious for cracking during bending. A notch was cut on the inside of each bend. In order to successfully achieve the desired bending radius without cracking, a ‘quick and dirty’ shop trick was used wherein the aluminum is ‘annealed’ using a torch, bent in its annealed state, then quenched. A thin layer of wood was added on top of the Al frame to increase rigidity of outer frame and serve as a base to mount components to.

Flight Computer and Electronics

After initial testing using an Arduino Mega and IMU sensor modules, a Consumer off the shelf (COTS) flight computer was selected in order to utilize the large open source UAV codebase called Ardupilot.

Ardupilot started in 2009 as a project to create an open source Arduino based flight computer for quadcopters. It has grown and evolved to encompass a vast array of autonomous flight capabilities, supporting tools, numerous vehicle configurations, and a very active user and developer community. Many commercially operating drone solutions use ardupilot or variations of ardupilot. In addition to flight controller firmware and software, ardupilot also features ground control software to send and receive telemetry from the vehicle, plan autonomous missions using waypoints, record detailed event logs from vehicle hardware, and much more. One of the most important features was the presence numerous failsafe and safety protocols to ensure safe and reliable operation. There is a large learning curve associated with the ecosystem, but sufficient documentation is provided, and help can be easily found in the active developer discord channel. Researchers interested in similar projects should highly consider Ardupilot as the basis for flight computer software and firmware.

There are many boards that support Ardupilot. The HolyBro Pixhawk 4 flight computer was selected as it featured sufficient I/O ports to support the relatively large number of motors, actuators, and sensors required. Several additional accessories were selected to create a robust electronics stack, including a power distribution board with I/O breakout pins, an external compass and GPS module, and a telemetry

transmission system to facilitate remote monitoring and control. Remote control operation was performed using a 2.5GHZ 16 channel FRSKY R-XSR SBUS receiver and a 2.5GHZ Taranis QX7 transmitter running open Tx

Technical Challenges

Once the testing frame was assembled, the path to a successful hover test was blocked by numerous technical bugs and challenges. For brevity, this section will only focus on mechanical challenges, and detailed discussion about debugging electronics, Ardupilot configuration, and code will be omitted.

Yaw stability

Multicopters tend to use an even number of motors so that opposite motors can rotate in opposite directions so that the torques generated by the spinning motors cancel out. In a tri-copter configuration, there is an odd number of motors meaning a resultant torque is inevitable. In the small scale design, all motors rotate the same direction. The two ways to counteract the yaw effect created by this torque are to tilt the front motor along the longitudinal axis of the craft, or to create vectored yaw control by differentially tilting the left and right motors independently. The vectored yaw control reduces the need for an extra servo, as the left and right motors already need to tilt for cruising flight, but tilting the front motor can be more effectively implemented in the large scale by using thrust vaning. A motor mount was designed that could transfer the lifting force generated by the front motor to the vehicle without applying any shear forces to the servo.

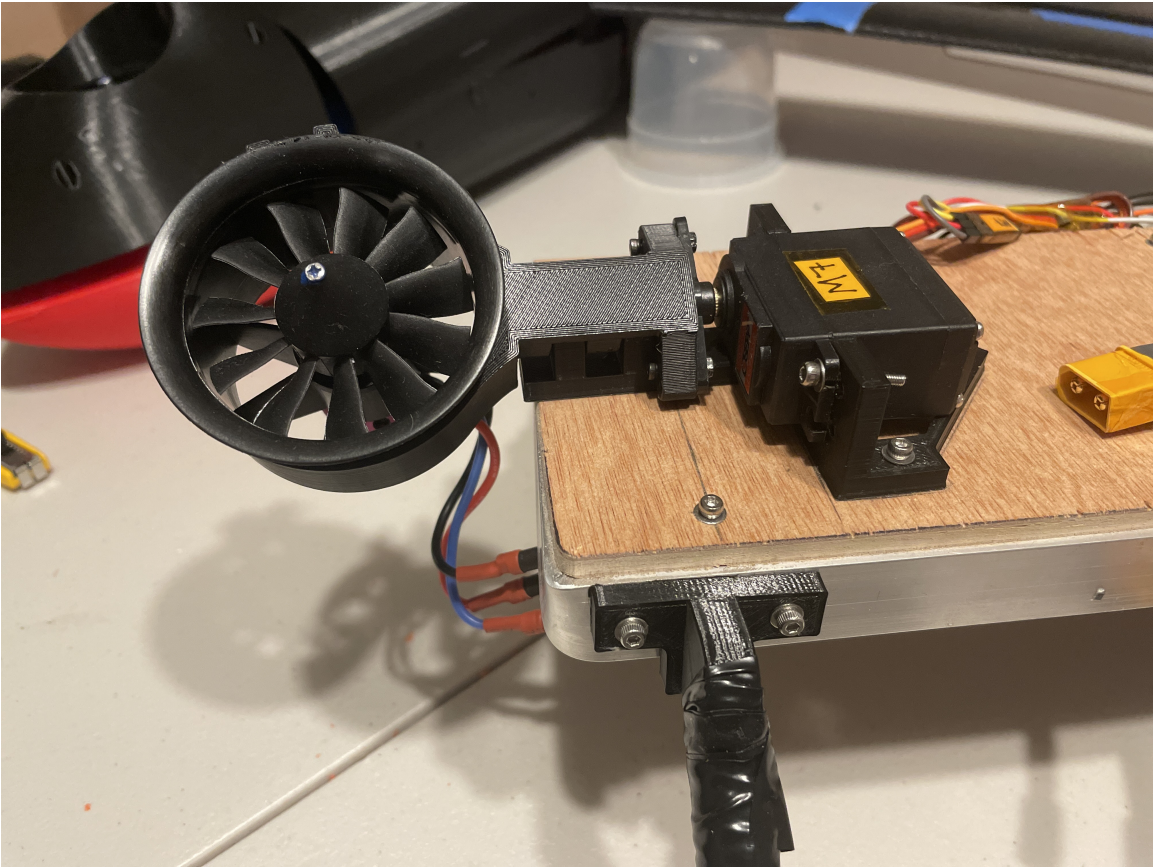


Figure 6.4: Front Tilt Mechanism.

Landing Gear

The landing gear was designed to provide the vehicle a wide base for stable takeoff and landing, while remaining as lightweight as possible. The legs are comprised of 5mm carbon fiber tubes connected to 3D printed brackets which are bolted directly to the aluminum frame. The legs are capped with "feet" made of a flexible, elastic 3D printing filament called TPU. The landing gear was designed to intentionally have a small degree of flexibility to help cushion impacts. During the testing and tuning phase, the landing gear experienced critical failure several times. The vehicle experienced much rougher landings than expected, and often landed in unpredictable orientations. When the vehicle landed with most or all of the impact on one leg instead of all 4, the landing gear would snap at the point where the rod inserted into the 3D printed bracket. The initial brackets were printed out of PLA, which has moderate material properties but the highest ease of manufacture. The initial landing gear design was based on the material properties of PLA, but in practice the parts

failed along layer lines, a failure mode inherent to Fused Deposition Modeling. The next version of the landing gear featured thicker walls, added ribs, and was printed so that the layer lines were orthogonal to applied stresses. Despite revisions, this generation of landing gear also experienced occasional failure throughout the testing process, as PLA is inherently not well suited for high impact applications. Despite having relatively high strength and stiffness, PLA is brittle and PLA parts have poor durability and resilience. The next iteration of landing gear was created using 3D printed Nylon, which in contrast has low strength and stiffness, but is flexible and can undergo significant elastic deformation without breaking. This made the landing gear extremely impact resistant, but also quite 'springy.'

6.4.3 Testing and Results

Once the vehicle was assembled, several static tests were performed. These tests included fastening the drone to a test stand in order to test motor control, servo direction, failsafes, safety switches, and ground control station communication. With the vehicle prepared for safe operation, the onboard sensors were calibrated (magnetometer, gyroscope, accelerometer, barometer, GPS).

The hover tests were performed, with tuning and troubleshooting between iterations. Detailed log data from every flight system, sensor, and RC input was recorded and analyzed in Matlab. The vehicle was operated in "stabilize" mode wherein vehicle dynamics are determined by remote operator RC inputs, but the system is actively stabilized using a PID controller and onboard sensors. To tune the PID gains, the Ziegler–Nichols method was used initially. By flight test 12, relatively stable hover flight was successfully demonstrated, experimentally proving that this vehicle configuration was stabilizable using closed loop feedback.

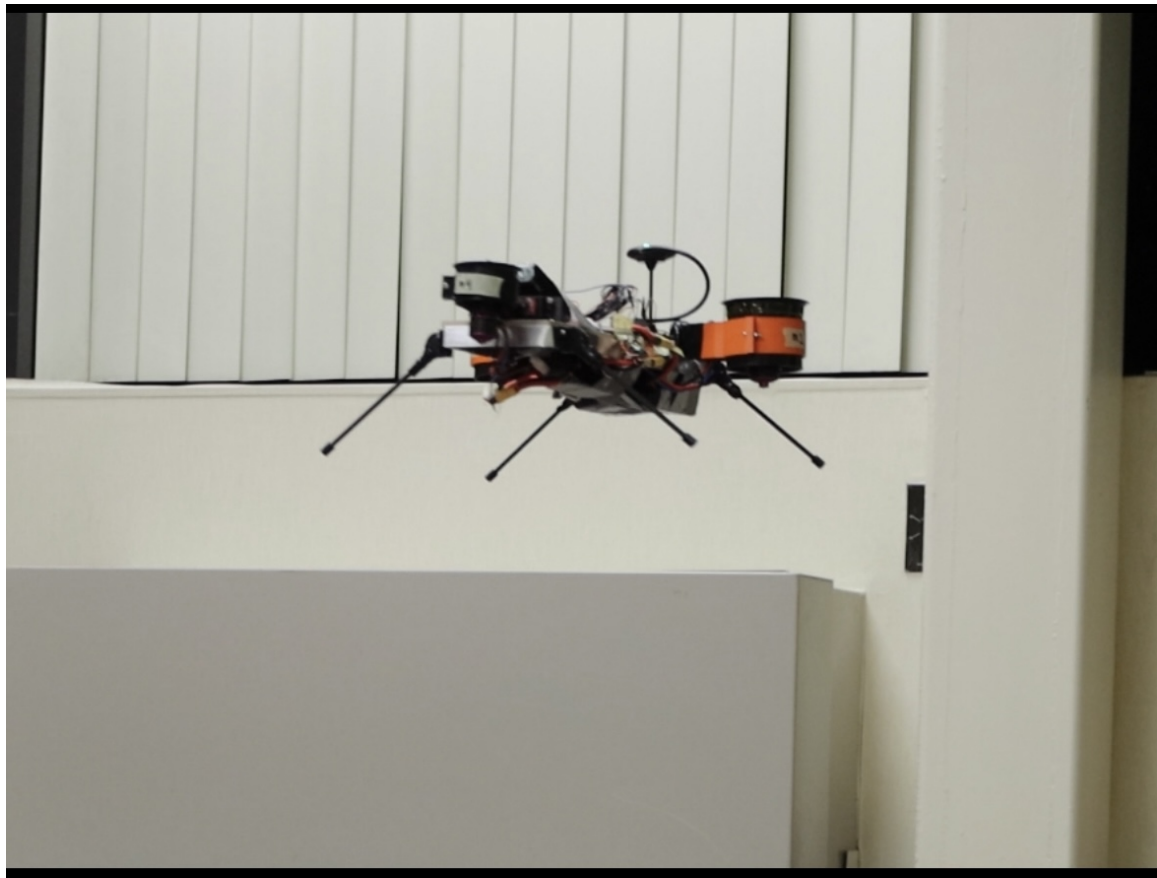


Figure 6.5: Stable hover test.

6.5 Hermes: Small Scale Prototype Version 3

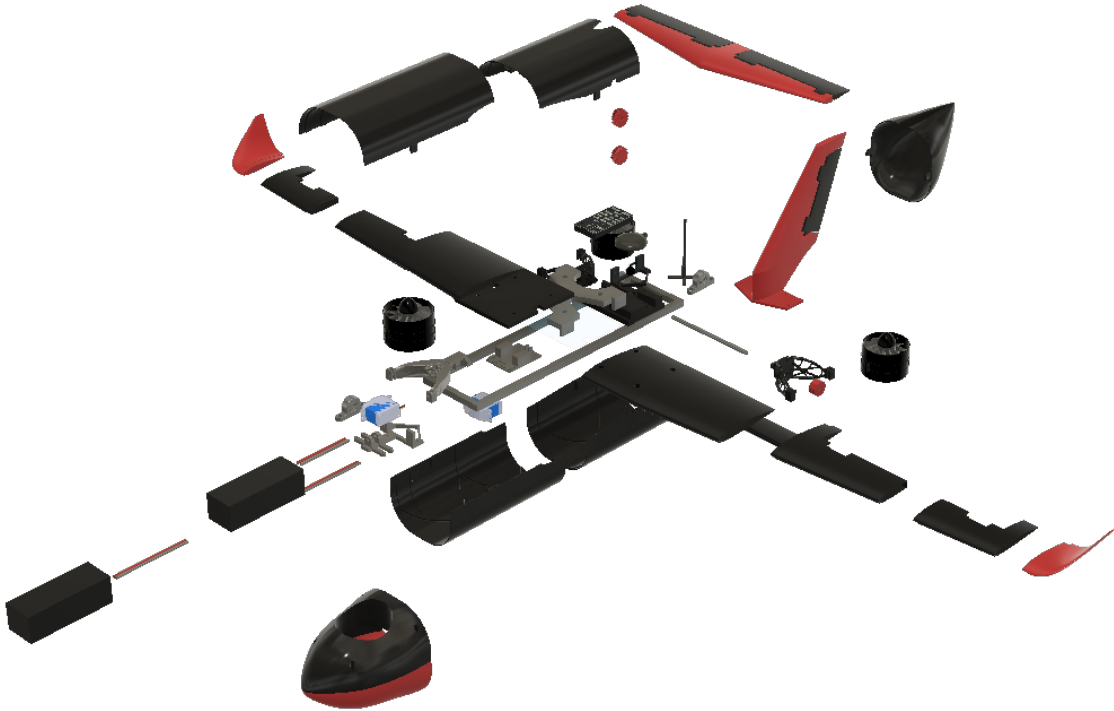


Figure 6.6: Version 3 prototype.

6.5.1 Goal

After validating the safety and reliability of the core systems, and successfully demonstrating stable hover, the final step of the prototyping process was to build a vehicle capable of completing an autonomous mission analogous to the full scale vehicle's proposed mission profile. The vehicle would take off in VTOL mode, tilt the rear EDFs forward, and autonomously cruise in fixed wing mode, before transitioning back to VTOL mode to land.

6.5.2 Results

Using a variety of rapid prototyping techniques (relying heavily on FDM 3D printing), a vehicle was fabricated capable of fulfilling the aforementioned scope. Each aspect and subsystem of the final mission profile was successfully demonstrated individually. At the time of publication, the final test of the full mission profile is awaiting

permission to use a suitable testing location that complies with all safety and legal regulations.

6.5.3 Addressing Issues of Prior Iteration

Several known issues and design flaws were discovered during the experimental testing of the Chiron prototype.

The first main issue involved the frame. The design of the Chiron frame suffered from being too heavy, and highly susceptible to twisting and torsion, making it poorly suited to the requirements of the aircraft. A lightweight, stiff, and durable frame is desirable. A variety of frame options were evaluated such as body-on-frame, monocoque, stressed skin, and space-frame. A ladder-frame design was chosen wherein square carbon fiber tubes connected by 3D printed brackets formed the main structure. This design was chosen as it offered a high stiffness at a low weight, it was easy to manufacture, and it made it easier to make modifications.

The second issue with Chiron was that the front motor was slightly underpowered. The 50mm front EDF generated 770 grams of thrust compared to 2200 grams of thrust generated by each of the rear EDFs. While the system worked with the 50mm EDF, performance was improved by switching to a larger front EDF. A 70mm EDF with a 3400kv DC brushless motor powered by a 2300-4000mah 4S LIPO battery was selected.

The third issue was with the mechanism used to mount the rear EDFs. The first iteration of the design was unnecessarily heavy, difficult to secure to the tilt rotor shaft, and was prone to vibrations. These issues were addressed by the redesigned mechanism discussed below.

6.5.4 Tilt Rotor Mounting Mechanism

The tilt rotor subsystem features the two rear EDFs, an axle supported on two bearings which is rotated by a gearbox, and a mounting mechanism to attach the EDFs to the axle.

Mounting to Axle

One drawback of 3D printed designs is that it is difficult to integrate them with other non-plastic components. When attaching the plastic motor mounts to the steel axle, the two main degrees of freedom that need to be constrained are (1) Sliding

along the axle and (2) Slippage wherein the mount rotates independently of the axle. The two most effective solutions to this in theory would be to epoxy the axle in place or to bore a hole into the axle and pin or bolt the plastic mount to the axle. Neither of these approaches could be considered as the epoxy was too permanent and would make it impossible to disassemble the tilt rotor mechanism, and the equipment required to safely bore into a 1/4" hardened steel shaft was not readily accessible. The first attempt to solve this problem relied on a tight press fit, but several attempts revealed that 3D printed PLA easily deforms and press fits were prone to loosening during use. The second attempt was to use a shaft collar. The round steel axle was replaced with a D profile axle to eliminate rotational slippage between mount and axle. A 3D printed shaft collar was quite effective at securing the shaft, but had the drawback of being difficult to attach to the mounting mechanism. The last set of iterations involved using a set screw. A brass threaded insert was melted into the plastic to provide threads for the set screw to hold onto. In order to tighten the set screw sufficiently, the forces on the threaded insert would cause it to pull out of the surrounding plastic. Ultimately, a final design was converged upon using two set screws and a thick plastic ring around the shaft with slots to hold captive nuts and washers. The set screw could be tightened sufficiently with minimal risk of pulling the captive nut through the plastic. This design was also used to fasten the tilt rotor gearbox to the same axle.

Tilt Rotor Gearbox

In order to use a servo motor to tilt the rear motors during transition from VTOL to cruising flight, a mechanism was required to transfer torque from the servo to the axle. Due to the angular limits of the servo(180°, the maximum gear ratio is 2:1. Using an all metal gear digital servo with 25kg.cm torque means a lower gear ratio can be used. The gearbox and gears were fabricated out of PLA. In theory, more durable 3D printer filament materials are better suited for making gears such as Nylon, PETG, and ABS, but given the low speeds and low cycle count of this application PLA was selected as it is easier to print with and offers higher dimensional accuracy with better print tolerances. 3D printed gears are prone to breaking off teeth, binding due to surface imperfections, and often must be printed very large and very heavy to compensate for those shortcomings. In order to design a more compact gearbox under the same material limitations, a Herringbone gear (often referred to as double helical gear) was selected. Compared to the traditional spur gears, these gears have

increased contact ratio, and a smoother transition between teeth. The simple shape of Herringbone gears make them hard to manufacture using traditional techniques but ideal for additive manufacturing, as the geometry can be more easily printed without imperfections or inaccuracies. With a given 3D printer, it is likely that a Herringbone gear can be printed faster, and more accurately resulting in a smaller gear box that is smoother, quieter, and less likely to fail. They are also self centering and self retaining which increases the robustness of the gearbox given the potential for inaccuracies and misalignment. The geometry of gears means they must be printed with layer lines perpendicular to the axis of rotation. When transmitting torque from the gear to the shaft, 3d printed gears often fail due to shearing a face along a layer line. To combat this, the mechanism that attaches to the shaft was printed as a separate body in two halves with layer lines orthogonal to those of the gear, then glued together and inserted as a "+" shaped peg into a "+" shaped hole in the gear and glued into place. The sum of these design and manufacturing considerations results in a gearbox that is quieter, smoother, more reliable, smaller, and lighter than traditional 3D printed gearboxes.

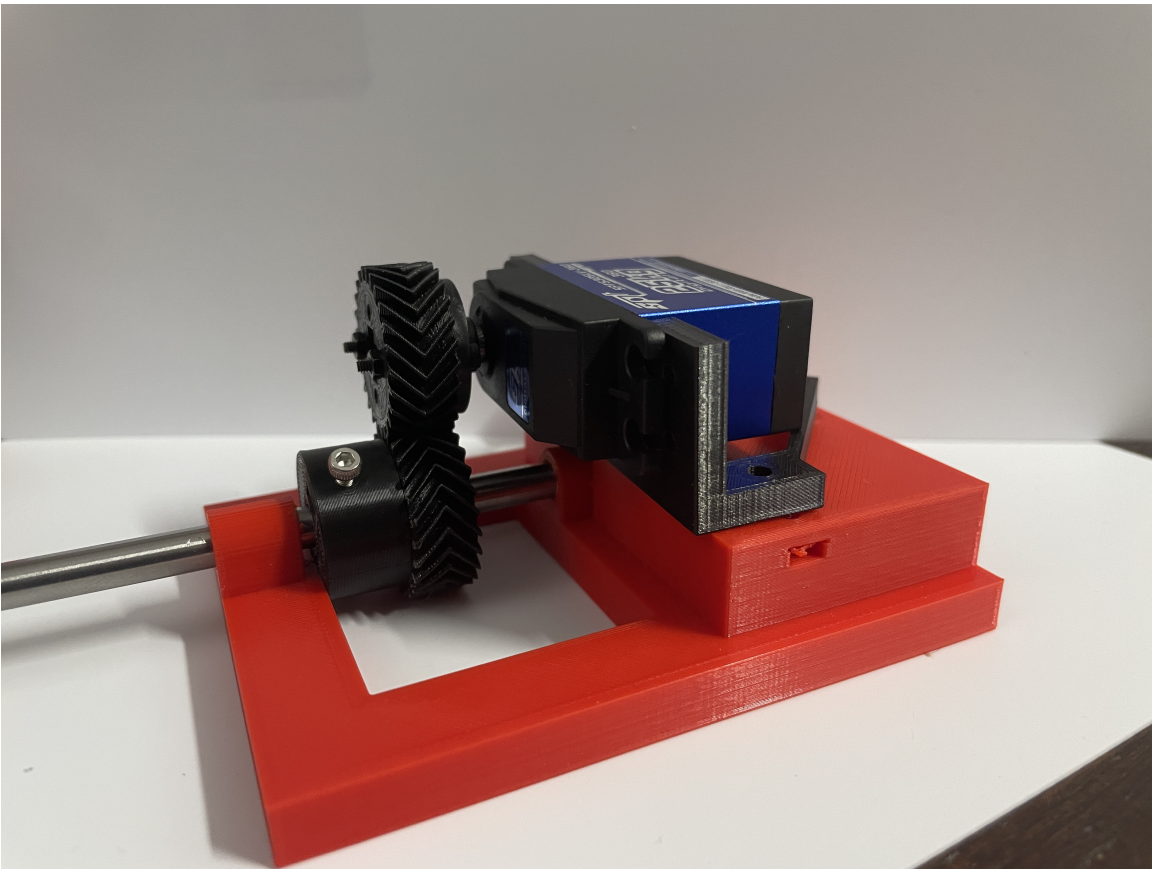


Figure 6.7: Gear box for tilting rear EDFs.

6.5.5 Generative Design

In general, FDM 3d printed parts are not well suited to aerospace applications. They tend to be larger, heavier, and more susceptible to a variety of failure modes than alternative materials and manufacturing methods. Despite these drawbacks, 3D printed parts offer several key advantages as they can be rapidly manufactured at a low cost, and can be created in geometries that are difficult or impossible to replicate using other manufacturing techniques.

In order to optimize several 3D printed components to be lighter, stronger, and stiffer several computational tools were used.

The first tool used is generative design, a computational tool where "Designers or engineers input design goals into the generative design software, along with parameters such as performance or spatial requirements, materials, manufacturing methods, and cost constraints. The software explores all the possible permutations of a solution, quickly generating design alternatives. It tests and learns from each iteration

what works and what doesn't." [5]

This tool was used to optimize the EDF motor mounts. The generatively designed mounts had a weight reduction of 74.2% compared to the original design.

The tool is able to optimize parameters taking into account specific manufacturing methods, materials, and real world per unit costs. Manufacturing methods include additive manufacturing, 3-5 axis CNC mill, 2D cutting, and Die casting. This tool provided detailed insight into manufacturing costs and how they scale with quantity. Additionally, the tool made it easy to consider a variety of materials side by side and compare outcomes across a vast array of parameters. This tool was useful in generating meshes that were 3D printed and tested. Users could compare and evaluate outcomes based on which orientation it should be printed on, as well as specify the limitations specific to their machine such as maximum overhang angle and minimum wall thickness.



Figure 6.8: 3D printed, generatively designed motor mount.

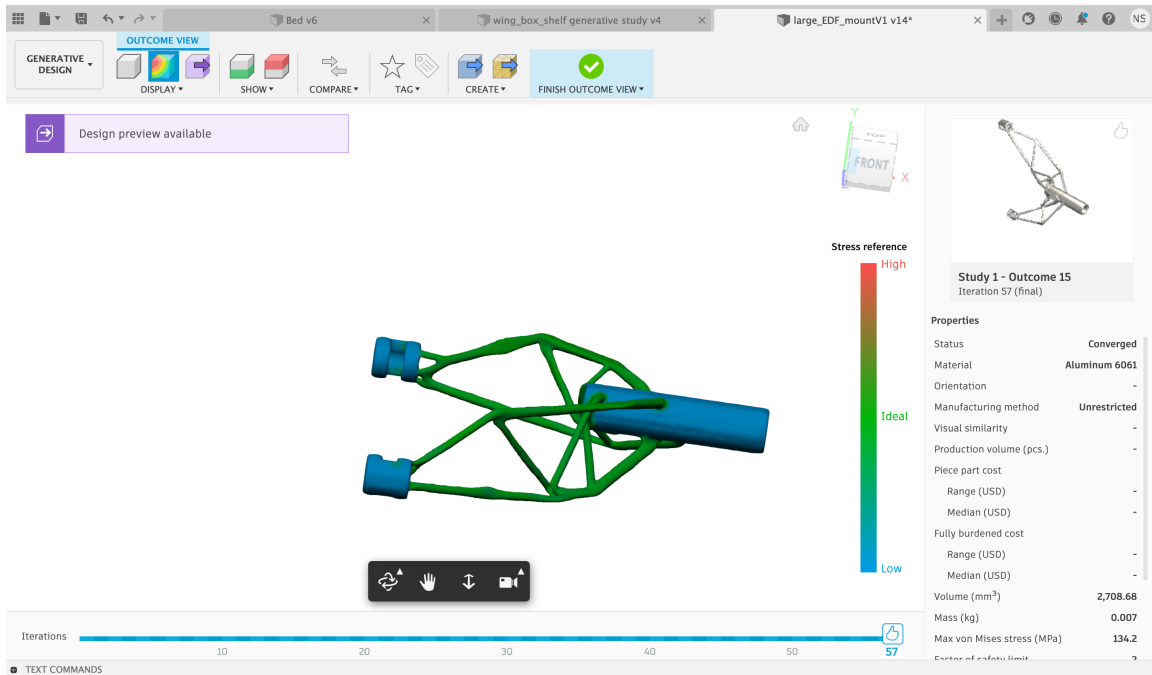


Figure 6.9: 3D printed, generatively designed motor mount.

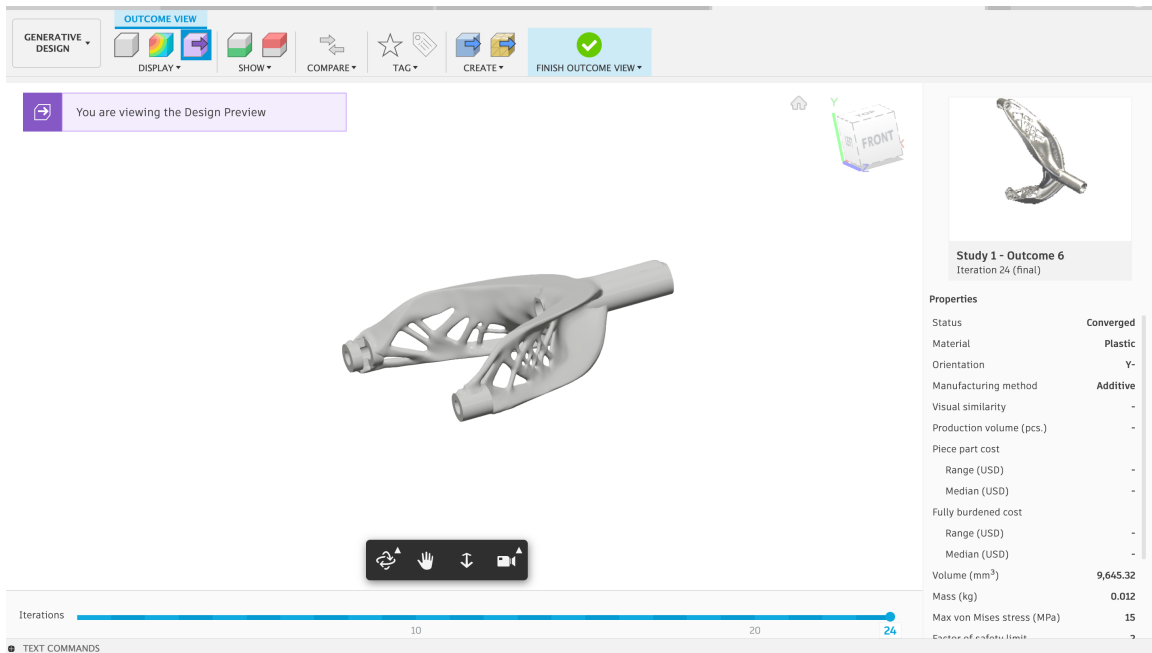


Figure 6.10: 3D printed, generatively designed motor mount.

This tool, while not applicable in all contexts, can significantly increase strength and reduce weight of parts used throughout the prototyping process. Moving forward,

this tool is especially useful in deriving design and manufacturability insights for the larger scale design. For example, after modeling an idealized part in CAD, the a generative design study can be run to evaluate whether the design would be better served by a carbon fiber part or an aluminum part (as well as choosing between different alloys of aluminum), and evaluate the best manufacturing technique. It creates an optimal design for every permeation of material and manufacturing process, and enables the designer to select designs to compare or further evaluate.

6.5.6 Topology Optimization

Similar to the generative design tool, the topology optimization tool takes a CAD design and a set of parameters, and iteratively optimizes a part for minimum mass or maximum stiffness. This tool was used to optimize the wing box, which connects the wings to the body frame. Rather than using the computer optimized design directly, it was used as a reference to guide manual design improvements. The design based on the recommendations from the topology optimization study was 30% lighter and 62% stiffer.

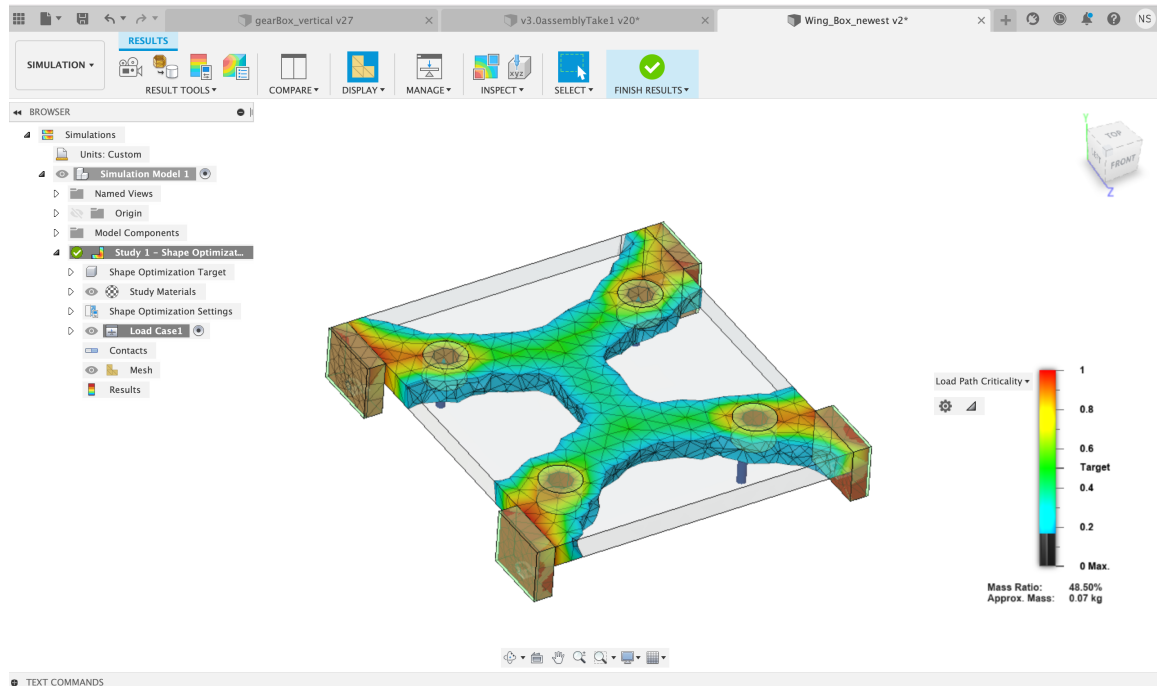


Figure 6.11: A mesh showing the wing box after topology optimization.



Figure 6.12: Sections of the fuselage.

6.5.7 Future Considerations

The current vehicle is awaiting a fully autonomous flight test. Revisions will be made depending on the results of that mission. Many revisions can be made to reduce weight of various components. Another set of improvements could be made related to the autonomous capabilities of the electronics stack. A computer vision system can be mounted to allow the vehicle to detect a landing pad with a specific marker on it in order to improve landing accuracy.

Chapter 7

Conclusions and Future Directions

As a result of this design process, it was determined the proposed compact, heavy-lift VTOL drone is a capable configuration. The starting range goal was 500 miles, and was surpassed with a final range of 656 miles. A MIMO controller was also developed to analyze the VTOL flight characteristics in ascent, as well as a guidance law for analyzing descent. Further work on this project will be to develop the subscale model into a functional aircraft that can VTOL, transition, and cruise. Further work on the controller will be to develop an LQI controller that can mitigate steady state errors.

We hope to continue on this project together by further developing the aircraft, filing for a patent, and developing a business.

Bibliography

- [1] Fast Facts on Transportation Greenhouse Gas Emissions, 2021.
- [2] Pegasus Aeronautics. GE70, 2021.
- [3] Kenneth J. Arrow, Leonid Hurwicz, and Hirofumi Uzawa. Constraint qualifications in maximization problems. *Naval Research Logistics Quarterly*, 8:175–191, 1961.
- [4] Astrom and Murray. *Feedback Systems: An Introduction for Scientists and Engineers*. Princeton University Press, Princeton, 2012.
- [5] Autodesk. Generative Design, 2021.
- [6] Shenzhen Grepow Battery Co. High Discharge LiPo Pouch Cells, 2021.
- [7] Carsten Braun D. Felix Finger. An initial sizing methodology for hybrid-electric light aircraft. *Aviation Technology, Integration, and Operations Conference*, pages 1–20, 2018.
- [8] Vasy Fan. VasyFan VF-160, 2021.
- [9] Morgan Forde. Research conflicts on drone delivery costs, efficiency as parcel carriers scale operations, 2021.
- [10] Schubeler Technologies GmbH. DS-215-DIA HST (195mm), 2021.
- [11] Eswarmurthi Gopalakrishnan. Quadcopter flight mechanics model and control algorithms. Unpublished paper, 2016.
- [12] Daniel P. Raymer. *Aircraft design: A conceptual approach*. American Institute of Aeronautics and Astronautics., Washington, D.C., 1989.
- [13] Jan Roskam. *Airplane Design Part II: Preliminary Configuration Design and Integration of the Propulsion System*. DARcorporation, Lawrence, 1997.

- [14] R.F. Stengel. *Flight Dynamics*. Princeton University Press, Princeton, 2004.
- [15] Tianyuan Zhao. Propulsive battery packs sizing for aviation applications. *Embry-Riddle Aeronautical University*, 8:175–191, 1961.

Appendix A

Sizing Calculations

A.1 Carpet Plot Generation

```
AR = 13;
Cd0 = 0.02;
e = 0.6;
k = 1/(Pi*AR*e);
Cd[CL_] := Cd0 + k*CL^2;
Clreq[WS_, beta_] := (beta*WS)/(qbar);
rho = 1.19;
rhosl = 1.25;
a = 339;
M = 0.21;
V = M*a;
qbar = 0.5*rho*V^2;
Btakeoff = 1;
Bclimb = 0.99;
alphatilde = rho/rhosl;
dhdt = 2.7;
LDmax = (1/(2*(k*Cd0)^0.5));
TWcruise[WS_, beta_, alpha_] := ((beta/alpha)*(Cd[Clreq[WS, beta]]*qbar))/(WS);
TWclimb[WS_, beta_, alpha_] := (((beta/alpha)*(Cd[Clreq[WS, beta]]*qbar))/(WS)) + (1/V)*(dhdt);
Clmax = 1;
FindMinimum[V*TWcruise[W, Bclimb*Btakeoff, alphatilde], {W, 1000}, WorkingPrecision -> 10]
FindMinimum[V*TWclimb[W, Bclimb*Btakeoff, alphatilde], {W, 1000}, WorkingPrecision -> 10]

{4.187696409, {375.44 -> 2132.342646} }

{6.887696409, {375.44 -> 2132.342646} }
```

Figure A.1: Mathematica Script for carpet plot generation and match point calculation.

A.2 Actuator Disk Parameters

```
bschub = 2.866 * 10^-7;
Treq = 120 / 12.2 / 2; (* Thrust required for each EDF *)
wrpm = (Treq / bschub)^0.5;
wrps = wrpm / 60;
d = 7.7 * 0.0254; (* diameter in meters *)
rho = 1.225;
Ct = (Treq * 4.45) / (rho * wrps^2 * d^4);
Cp = (Treq * 4.45 * V) / (rho * wrps^3 * d^5);

Print["Coefficient of thrust: ", Ct]
Print["Coefficient of power: ", Cp]
Print["Diameter: ", d, " m"]
Print["RPM: ", wrpm]

Coefficient of thrust: 2.56156
Coefficient of power: 13.505
Diameter: 0.19558 m
RPM: 4142.45
```

Figure A.2: Mathematica script to determine actuator disk parameters

A.3 Tail Sizing

```
: (* tail sizing *)
bw = 68 / 12;
Sw = 344 / 144;
Lht = (57 - 36) / 12;
Lvt = (51 - 36) / 12;
cbar = 5.67 / 12;
cvt = 0.051; (* vertical stabilizer volume coefficient *)
cht = 1.29; (* horizontal stabilizer volume coefficient *)
Svt = (cvt * bw * Sw) / (Lvt);
Sht = (cht * cbar * Sw) / (Lht);
Print["Vertical stabilizer wing area: ", Svt, " ft2"]
Print["Horizontal stabilizer wing area: ", Sht, " ft2"]

Vertical stabilizer wing area: 0.552311 ft2
Horizontal stabilizer wing area: 0.83205 ft2
```

Figure A.3: Mathematica script for tail sizing.

A.4 Neutral Point Calculations

AoA	Cmy,ref	CL	Cmy,ref/Cl
-1	-1.37743	0.20445	
0.444	-2.42359	0.36095	-6.6847284
1.889	-3.48589	0.51887	-6.7268237
3.333	-4.55314	0.67702	-6.7483402
4.778	-5.61987	0.83477	-6.7621553
6.222	-6.68006	0.99147	-6.7657307
7.667	-7.73323	1.14697	-6.7727974
9.111	-8.76381	1.2998	-6.7433096
10.556	-9.77194	1.44994	-6.7145997
12	-10.7531	1.59679	-6.6814436

Figure A.4: $\frac{\partial C_{M_{ref}}}{\partial C_L}$ for full configuration, AR = 13.4

AoA	CMy	CL	Cmy/Cl
-1	-5.06253	0.746	
0.444	-6.15928	0.90247	-7.00933
1.889	-7.25781	1.05853	-7.03915
3.333	-8.32606	1.211	-7.0063
4.778	-9.38482	1.36188	-7.01723
6.222	-10.4171	1.50936	-6.99939
7.667	-11.4205	1.65357	-6.95791
9.111	-12.392	1.79376	-6.92995
10.556	-13.3235	1.92934	-6.87041
12	-14.2067	2.05924	-6.79885

Figure A.5: $\frac{\partial C_{M_{ref}}}{\partial C_L}$ for full configuration, AR = 17.3

A.5 Flight Mode Power and Range Calculations

```
(* flight mode analysis *)
(* climb 1 *)
wAinitial = 120; (* initial weight, lbs *)
Preq = (V * (1 / LD) * wAinitial * 4.45 + wAinitial * 4.45 * dhdt) / 0.78; (* total power requirement, W *)
PreqCLIMB1GEN = 4; (* generator power requirement, kW*)
mdot = 0.61 * PreqCLIMB1GEN / (3600); (* mdot fuel , kg/s*)
timeclimb = 102; (* TOF, s *)
fuelburn = (mdot * timeclimb) * 2.2; (* fuel burn, lbs. *)
wAc11 = wAinitial - fuelburn; (* final weight, lbs. *)
betaC11 = wAc11 / wAinitial; (* beta climb 1 *)
m2mi = 0.000621371;
rC11 = 71.2 * .96 * 102 * m2mi; (* range climb 1 *)
Print["Climb 1 flight mode "]
Print["Total power requirement: ", Preq/1000, " kW"]
Print["Power requirement, generator: ", PreqCLIMB1GEN, " kW"]
Print["Range: ", rC11, " mi"]
Print["beta: ", betaC11]

Climb 1 flight mode
Total power requirement: 5.84336 kW
Power requirement, generator: 4 kW
Range: 4.33214 mi
beta: 0.998733
```

Figure A.6: Mathematica Script for climb 1 flight mode calculation

```
(* cruise 1 *)
wAinitial = wAc11; (* initial weight, lbs. *)
PreqCRUISE1 = (V * (1 / LD) * wAinitial * 4.45) / 0.78; (* generator power requirement, W*)
Treq = wAinitial * 4.45 / LD; (* thrust required, N *)
mdot = 0.61 * PreqCRUISE1 / (3600 * 1000); (* mass flow rate of fuel, kg/s *)
TSFC = mdot / Treq; (* Thrust specific fuel consumption, SI units *)
rCr1 = 245.7; (* range, mi *)
NSolve[rCr1/m2mi == (1/10) (V / TSFC) (LD) Log[1/(beta)], beta]
betaCr1 = .932;
wAc1 = betaCr1 * wAinitial; (* final weight, lbs. *)
Print["Cruise 1 flight mode "]
Print["Power requirement, generator: ", PreqCRUISE1/1000, " kW"]
Print["Range: ", rCr1, " mi"]
Print["beta: ", betaCr1]
{{beta → 0.932013} }

Cruise 1 flight mode
Power requirement, generator: 3.98984 kW
Range: 245.7 mi
beta: 0.932
```

Figure A.7: Mathematica Script for cruise 1 flight mode calculation

```

(* climb 2 *)
wAinitial = wAcr1 - 25; (* initial weight, lbs. *)
Preq = (V*(1/LD)*wAinitial*4.45 + wAinitial*4.45*dhdt)/0.78; (* Total power required, W *)
PreqCLIMB2GEN = 4;
mdot = 0.61*PreqCLIMB1/(3600); (* mass flow rate of fuel, kg/s *)
timeclimb = 102; (* TOF, s *)
fuelburn = (mdot*timeclimb)*2.2; (* weight of fuel burned, lbs. *)
wAcl2 = wAinitial - fuelburn; (* final weight, lbs. *)
betac12 = wAcl2/wAinitial;
Print["Climb 2 flight mode "]
Print["Total power requirement: ", Preq/1000, " kW"]
Print["Power requirement, generator: ", PreqCLIMB2GEN, " kW"]
Print["Range: ", rCr1, " mi"]
Print["beta: ", betac12]

Climb 2 flight mode
Total power requirement: 4.22174 kW
Power requirement, generator: 4 kW
Range: 245.7 mi
beta: 0.998246

```

Figure A.8: Mathematica Script for climb 2 flight mode calculation

```

(* cruise 2 *)
wAinitial = wAcl2; (* initial weight, lbs. *)
PreqCRUISE2 = (V*(1/LD)*wAinitial*4.45)/0.78; (* Power requirement, W *)
Treq = wAinitial*4.45/LD; (* Thrust required, N *)
mdot = 0.61*PreqCRUISE2/(3600*1000); (* mass flow rate fuel, kg/s *)
TSFC = mdot/Treq; (* TSFC, SI units *)
NSolve[rCr1/m2mi == (1/10) (V/TSFC) (LD) Log[1/(beta)], beta]
betaCr2 = .932;
wAcr2 = betaCr2*wAinitial; (* final weight, lbs. *)
betatotal = betaCl1*betaCr1*betaCr2*betac12;
Print["Cruise 1 flight mode "]
Print["Power requirement, generator: ", PreqCRUISE1/1000, " kW"]
Print["Range: ", rCr1, " mi"]
Print["beta: ", betaCr2]
Print["total beta: ", betatotal];
{{beta → 0.932013} }

Cruise 1 flight mode
Power requirement, generator: 3.98984 kW
Range: 245.7 mi
beta: 0.932
total beta: 0.866001

```

Figure A.9: Mathematica Script for cruise 2 flight mode calculation

A.6 Control Surface Sizing

```
(* control surface sizing *)
Sw = 389 / 144;
cbar = 5.5 / 12;
bw = 82 / 12;
cv = 7.27 / 12;
ch = 5.14 / 12;
Sv = 0.55;
Sh = 0.83;
Sr = Sv * 0.45;
crr = 0.48 * cv;
crt = 0.41 * cv;
Sa = 0.064 * Sw;
cain = 0.3 * cbar;
caout = 0.29 * cbar;
aspanlocin = 0.6 * (bw / 2);
aspanlocout = 0.9 * (bw / 2);
Se = 0.41 * Sh;
cer = 0.42 * ch;
cet = 0.39 * ch;
Print["Aileron area: ", Sa, " ft2"]
Print["Aileron inner chord location: ", cain, " ft"]
Print["Aileron outer chord location: ", caout, " ft"]
Print["Aileron inner span location: ", aspanlocin, " ft"]
Print["Aileron outer span location: ", aspanlocout, " ft"]
Print["Elevator area: ", Se, " ft2"]
Print["Elevator root chord: ", cer, " ft"]
Print["Elevator tip chord: ", cet, " ft"]
Print["Rudder area: ", Sr, " ft2"]
Print["Rudder root chord: ", crr, " ft"]
Print["Rudder tip chord: ", crt, " ft"]
```

Figure A.10: Mathematica Script for Control Surface Sizing based on values obtained in Roskam[13]

```
Aileron area: 0.172889 ft2
Aileron inner chord location: 0.1375 ft
Aileron outer chord location: 0.132917 ft
Aileron inner span location: 2.05 ft
Aileron outer span location: 3.075 ft
Elevator area: 0.3403 ft2
Elevator root chord: 0.1799 ft
Elevator tip chord: 0.16705 ft
Rudder area: 0.2475 ft2
Rudder root chord: 0.2908 ft
Rudder tip chord: 0.248392 ft
```

Figure A.11: Output for script in Figure A.10.

Appendix B

Final Configuration Analysis

B.1 Final Range

```
wA = 120; (* initial weight, lbs. *)
wfuel = 27;
betaclimb = 0.998;
LD = 12.2;
PreqCRUISE1 = (V * (1 / LD) * wA * 4.45) / 0.78; (* generator power requirement, W*)
Treq = wAinitial * 4.45 / LD; (* thrust required, N *)
mdot = 0.61 * PreqCRUISE1 / (3600 * 1000); (* mass flow rate of fuel, kg/s *)
TSFC = mdot / Treq; (* Thrust specific fuel consumption, SI units *)
NSolve[r == (1 / 9.8) (V / TSFC) (LD) Log[120 * betaclimb / (120 * betaclimb - 27)], r]
Print["Updated cruise characteristics"]
Print["Power requirement, generator: ", PreqCRUISE1 / 1000, " kW"]
Print["Range: ", (1.056 * 10^6) * m2mi, " mi"]
{{r → 1.05588×106}}
```

Updated cruise characteristics
Power requirement, generator: 3.9949 kW
Range: 656.168 mi

Figure B.1: Mathematica script for final range calculation.

Appendix C

GNC

C.1 VTOL Ascent

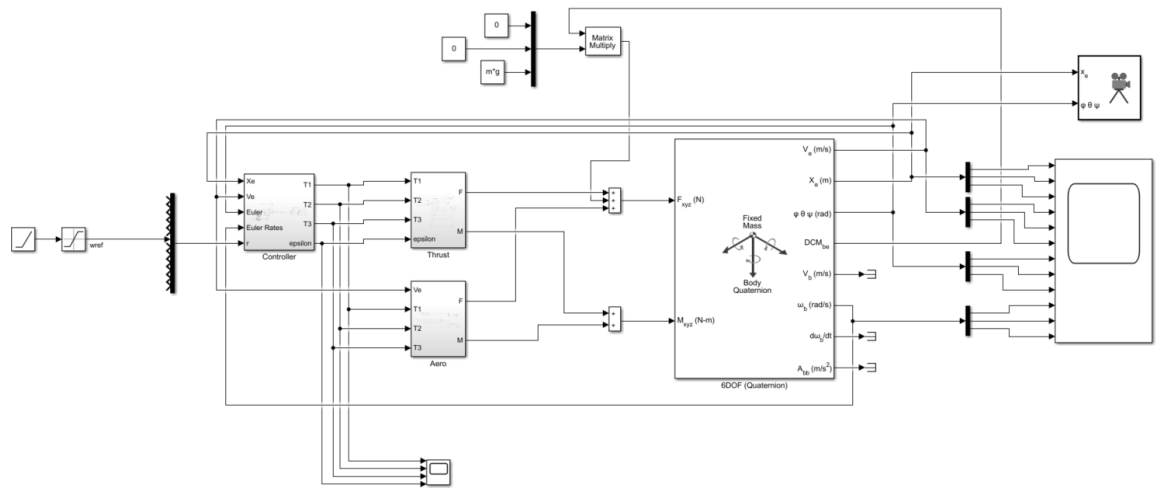


Figure C.1: Full Nonlinear Simulink Model.

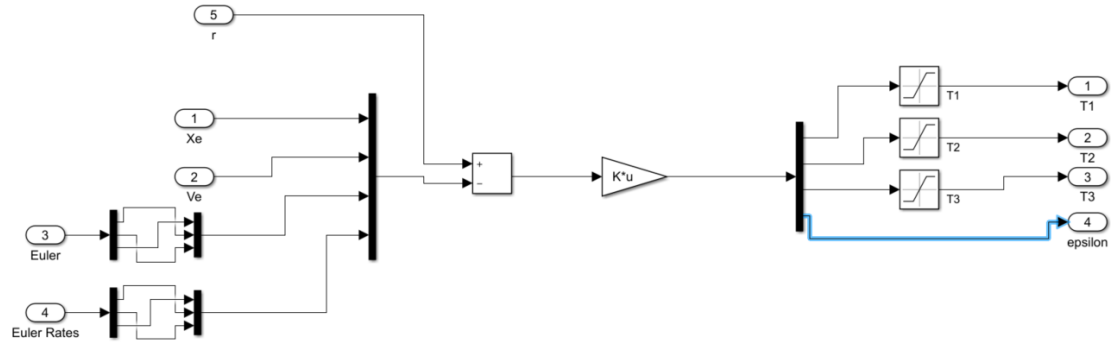


Figure C.2: Linear controller implemented in nonlinear Simulink model. Thrusts saturated at their maximum values.

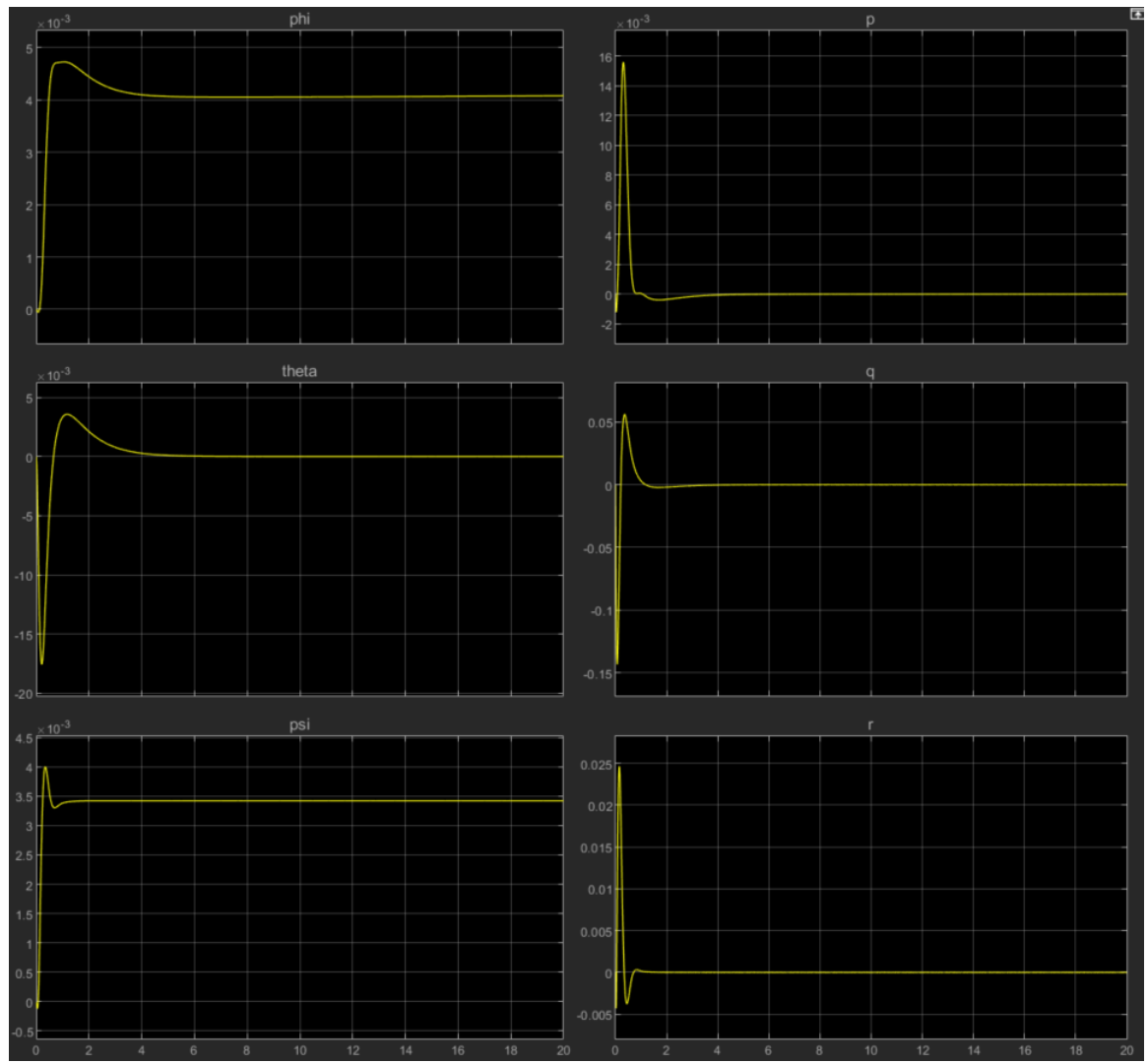


Figure C.3: Euler angle and body rate response to -0.5 ft/s ramp input.

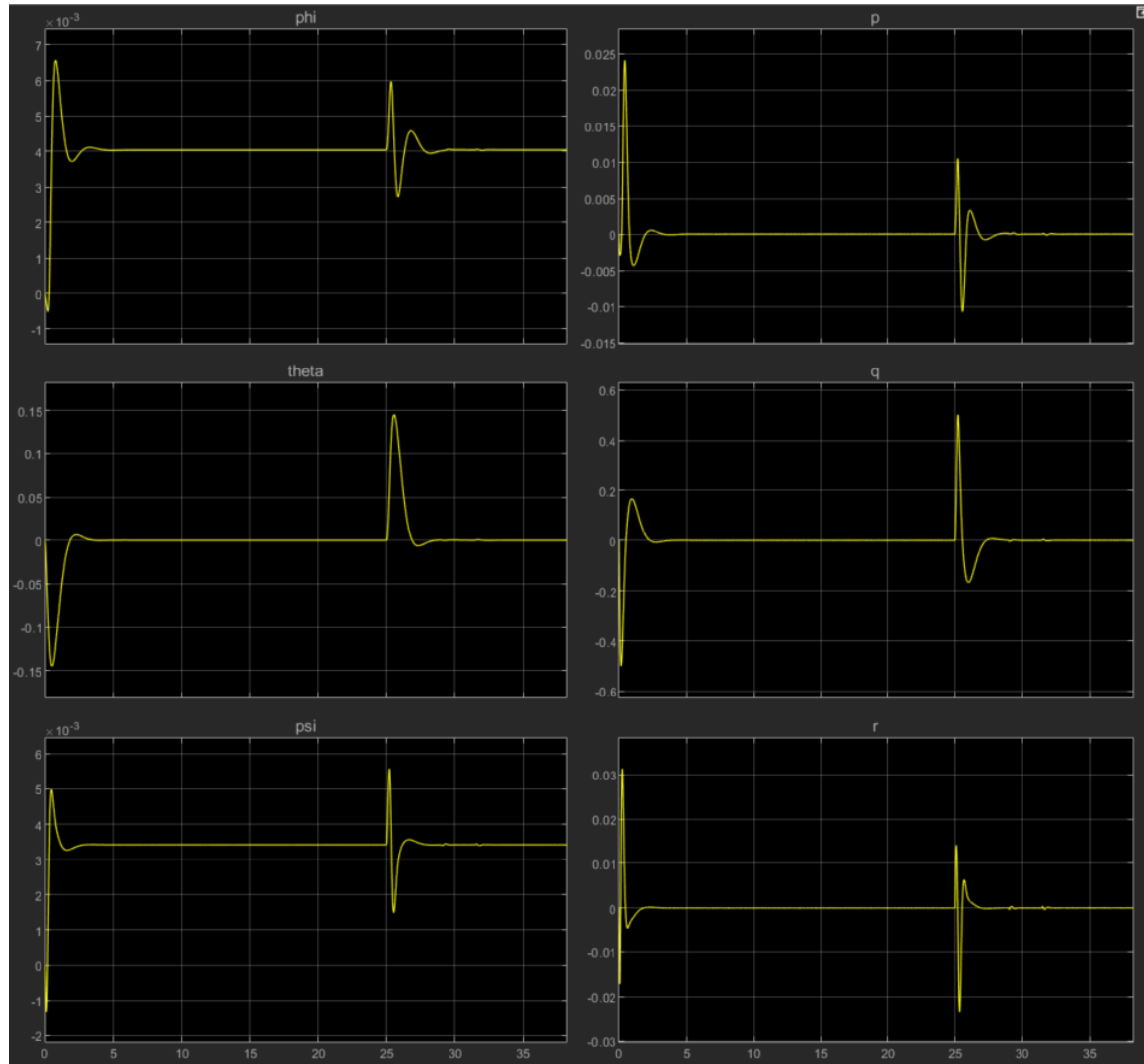


Figure C.4: Euler angle and body rate response to descent guidance.